École polytechnique de Louvain

Inertial enhancement in the Belgian High Voltage Grid with the Virtual Synchronous Generator

Authors : **Charles Dubuc**, **Clément Martin**
Supervisor : **Emmanuel De Jaeger**
Readers : **Bruno Dehez**, **Hervé Jeanmart**, **Claude Oestges**
Academic year 2019–2020
Master [120] in Electro-mechanical Engineering

Acknowledgements

We would like to take a moment to thank all the people that supported us through the writing of this thesis. Indeed, we are really grateful we could finish our thesis within the given time.

Foremost, we would like to express our deepest gratitude to Pr. Emmanuel De Jaeger for his continuous support, patience, enthusiasm and motivation. Without his guidance and sincere engagement, this thesis would not have been possible. Also, we would like to thank to him for his passion and pedagogy during the many courses he gave us during our master. He conveyed us his excitement for many energy topics and always was available to answer questions.

Then, we would like to thank Pr. Jeanmart, Pr. Oestges and Pr. Dehez for immediately agreeing to read our thesis and for taking the time to do so. Moreover, we are also grateful for the various classes these professors taught us with enthusiasm and passion.

Special thanks to Caroline Leroi for her availability during the past two years and for her direction in the several projects she supervised.

We would also like to acknowledge the assistance of Benoît Martin for his valuable advice and for the time he devoted to the careful proofreading of this work.

Finally, the completion of this dissertation would not have been possible without the support of our families. We are forever grateful to our parents for their love, care and sacrifices for educating us and giving us the opportunity to complete this degree. Also, many thanks to our brother and sisters for their support and attention. Last but not least, we would like to thank our grand-parents for their prayers and the interest they showed in our studies.

Abstract

The inertial response of rotating machines is an essential mechanical property of synchronous generators. It allows them to release kinetic energy from their shaft to help counteract the frequency deviation occurring during a power imbalance in the grid. The steady growth of renewable energy sources (RES) due to the current EU policies on energy transition reduces the grid inertia and jeopardizes the global grid stability.

To counteract this issue, the Virtual Inertia principle consists in emulating the inertial behaviour of synchronous generators thanks to the combination of inverters and energy sources such as RES. The goal of this thesis is to study the impact of the Virtual Inertia on the frequency stability of the Belgian High Voltage Grid.

The Virtual Inertia algorithm choice is made based on a litterature review. Then, the Virtual Synchronous Generator (VSG) algorithm, its simplifications and its implementation in SIMULINK are detailed. The second part of the modelling concerns the various power plants feeding the Belgian power network as well as the neighbouring countries and the downstream grid.

A parametric analysis of the simulation results is achieved to find the optimal VSG tuning parameters. Subsequently, a generator loss and a load increase of the same rated power are compared regarding their impact on frequency. Even if the load connection is more critical on the frequency behaviour, the VSG reduces in both cases the frequency deviation and the RoCoF in an efficient way to avoid frequency issues. Thereafter, the influence of RES penetration rate is investigated. As expected, increasing RES penetration rate reduces the grid inertia, leading to bigger frequency deviations and RoCoF. The VSG is efficient in reducing the RoCoF during an imbalance with the virtual inertia it provides.

Finally, the economical viability of VSG on the Belgian Grid is investigated. De-loading RES and energy storage with BESS are currently not profitable. However, the frequency regulation with the BESS can easily become profitable by introducing Inertia Tariffs to remunerate the VSG for its inertial support.

Keywords : Virtual Inertia, Virtual Synchronous Generator, RoCoF, Inertial Response, Primary Frequency Control, RES, Belgian High Voltage Grid

Contents

List of Figures

List of Tables

List of Abbreviations

ACE	Area of Control Error
BESS	Battery Energy Storage System
BHVG	Belgian High Voltage Grid
DFIG	Doubly Fed Induction Generator
DG	Dispersed Generation
EU	European Union
FSWT	Fixed Speed Wind Turbine
HVDC	High Voltage Direct Current
IEPE	Institute of Electrical Power Engineering
KHI	Kawasaki Heavy Industries
LCOS	Levelized Cost of Storage
MMC	Multi-level Modular Converter
MPP(T)	Maximum Power Point (Tracking)
NPV	Net Present Value
P&O	Perturbation and Observation
PI	Proportional Integral
PLL	Phase Locked Loop
PMSG	Permanent Magnet Synchronous Generator
PSF	Power Signal Feedback
PV	Photovoltaic
PWM	Pulse Width Modulation
RES	Renewable Energy Sources
RoCoF	Rate of Change of Frequency

SG / SM	Synchronous Machine/Generator
SOC	State of Charge
SPC	Synchronous Power Controllers
TSO	Transmission system operator
UFLS	Under Frequency Load Shedding
VISMA	VIrtual Synchronous MAchine
VSG	Virtual Synchronous Generator
VSWT	Variable Speed Wind Turbine
WSM	Wind Speed Measurement

Chapter 1

Introduction

1.1 RES and Dispersed Generation emergence on the grid

Since the early 2000s, Renewable Energy Sources (RES) have been booming and have become an increasingly important part of the electricity mix in many countries. This is also the case for Belgium, as shown in FIGURE 1.1, with a current electrical production from RES 8 times bigger than the one in 2005. This can be explained by many factors, such as the democratisation of renewable energy sources, the subsidies they receive, and the political directives that the EU has taken. Moreover, there is a net increase of the penetration rate of renewable energy sources in the electricity production from 2005 to 2019, from less than 5% in 2005 to more than 20% currently.

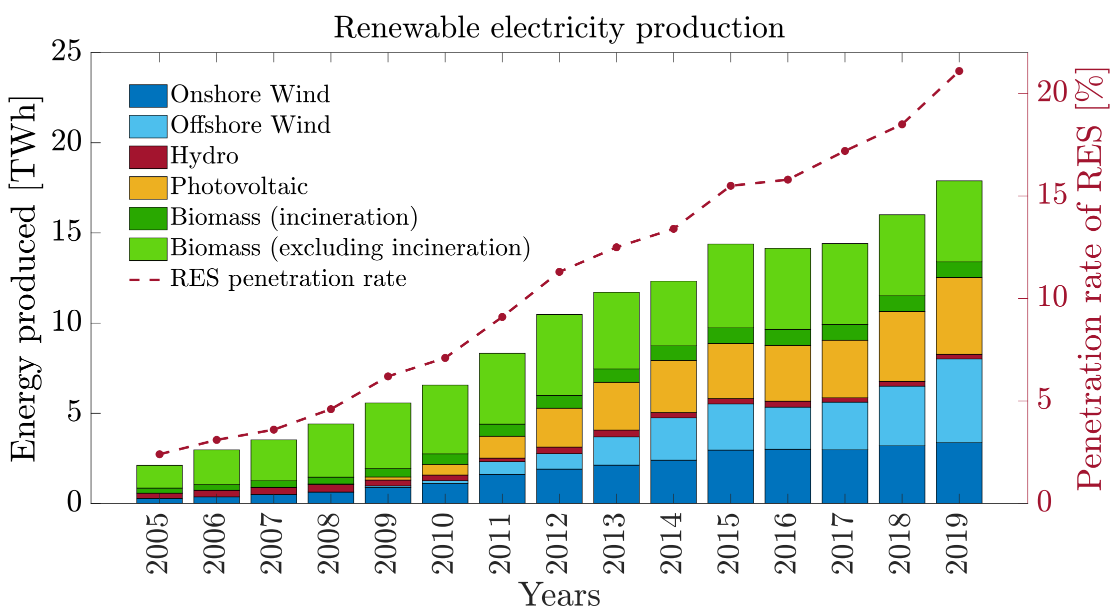

FIGURE 1.1: Renewable electricity production evolution and RES penetration rate evolution [1]

In 2007, in order to deal with the climate emergency, EU leaders put in place a climate package which became law in 2009. The package had three objectives for 2020:

- Reduce greenhouse gas emissions by 20% compared to 1990 levels.
- 20 % of EU energy production must come from RES.
- Increase energy efficiency by 20%.

This rapid development of RES has resulted in the transformation of an electrical network historically dominated by rotating machines into a network dominated by inverters [2], as illustrated in FIGURE 1.2. The grid topology is changing, giving way to more and more dispersed generation, i.e smaller size electrical generation connected to the low-voltage distribution grid [3]. Historically, electricity grids have been designed to transmit power generation from the high-voltage grid to the distribution grid on a unidirectional basis [3]. Increasingly, customers are becoming prosumers, i.e. consumers who also produce energy, e.g. via photovoltaics, wind power, and so on. This phenomenon leads to the growth of dispersed generation and thus to the transmission of electricity from downstream to upstream, which was not previously the case.

Furthermore, as the RES share in the energy mix increases, less energy is produced by rotating machines directly connected to the grid. These rotating machines are providing inertial support to the grid and this inertia helps to stabilise the frequency during a power imbalance. Therefore, the loss of inertia is harmful for the grid as frequency deviations will become more important. This paper will focus on increasing the inertia of the grid using RES in order to mitigate the frequency deviations.

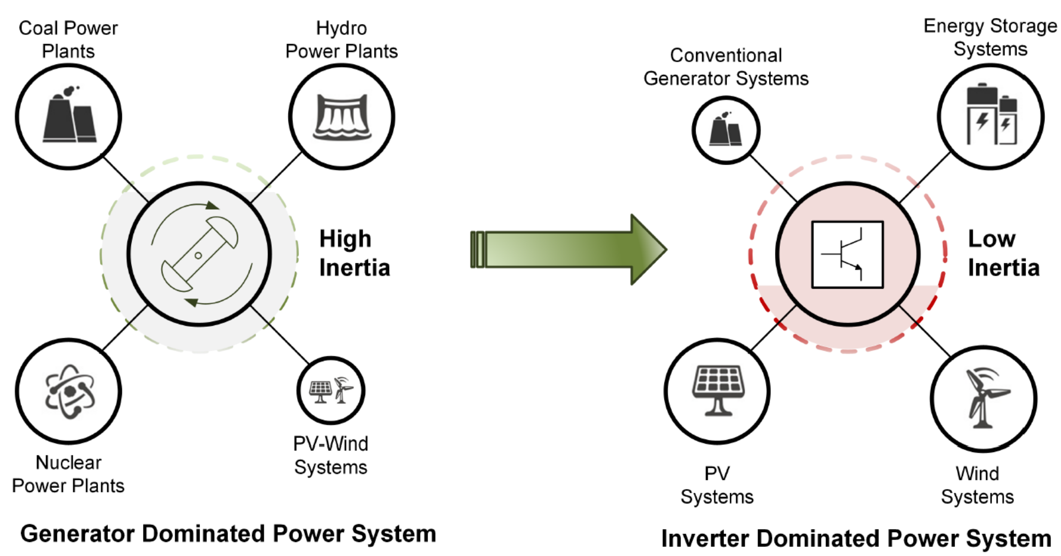

FIGURE 1.2: Modification of the network topology [2]

1.2 Inertia of rotating machines as a contributor to the frequency stability

In all power systems, active power production has to constantly match the demand. When there is an imbalance between the active power production and consumption, a frequency deviation appears and is partly compensated by kinetic energy from rotating machines connected to the grid.

A very important concept describing the behaviour of the rotating machines is illustrated by the swing equation in *Equation* 1.1 :

$$J\frac{d^2\theta_m}{dt^2} = T_m - T_e \tag{1.1}$$

Swing equation quantities		
J	[kg.m^2]	Moment of inertia of the rotor
θ_m	[rad]	Angular position of the rotor
T_m	[N.m]	Mechanical torque from prime mover
T_e	[N.m]	Electrical torque from machine

Since angular velocity of the rotor $\omega_m = \frac{d\theta_m}{dt}$ and $P = \omega T$, it becomes :

$$J\omega_m\frac{d\omega_m}{dt} = P_m - P_e \tag{1.2}$$

Introducing the inertia constant of the machine H, being the ratio between kinetic energy of the generator at synchronous speed and the rated power of the machine :

$$H = \frac{J\omega_s^2/2}{S_{nom}} \tag{1.3}$$

The swing equation can be rewritten as :

$$\frac{d\omega_m}{dt} = \frac{\omega_s^2}{2HS_{nom}\omega_m}(P_m - P_e) \tag{1.4}$$

The more kinetic energy available from the machines (or equivalently, the greater the inertia constant H), the smaller the rate of change of frequency (RoCoF) and thus the smaller the frequency deviation. Indeed, synchronous generators will give an electrical response proportional to their nominal power, to provide a fraction of the power loss. It is supplied by a mechanical source, which is here the stored rotational kinetic energy of generator shafts [4]. As energy is taken from the shaft of the synchronous machine, it is injected in the grid and counteracts the power imbalance in the grid. As a result, the grid frequency deviation is slowed down during the first moments of the power imbalance [4].

This initial support of the frequency by synchronous machines is called the **inertial response** of the machines. This physical phenomenon is crucial for the grid frequency stability. However, RES are connected to the grid through power electronics and has thus do not have rotating masses directly coupled to the grid [5]. In the way these converters are currently controlled, no inertia can be extracted from this type of generation. The increase of RES penetration rate in the power system results in a lower proportion of electrical rotating machines, and thus in a lower global inertia of the system. The swing equation does not only describe the behaviour of a machine, but can be generalized to a multi-machine system. If the system is considered as a global synchronous machine, the decrease of grid inertia can be interpreted as the decrease of this equivalent synchronous generator inertia. This makes the grid more and more sensitive to sudden and unforeseen power imbalances.

1.3 RoCoF as a stability indicator

As previously mentioned, the **R**ate **of** **C**hange **of** **F**requency (i.e the time-variation of grid frequency) is one of the most impacted quantities by the overall decrease of grid inertia. This quantity is important as it is used in the control of protection systems. Here are two common uses of RoCoF protection relays :

- **Loss of mains / Islanding protection** : it detects the loss of connection of the upstream grid to the distribution grid [6]. If the connection is lost, the grid becomes islanded and some of the benefits of the main grid connection disappear, such as the reliability of the voltage and frequency control usually provided by transmission grid [7].
- **Under/over frequency detection** : this allows disconnection of the generators when the frequency reaches values outside the acceptable range for normal operation, allowing them to avoid costly damages resulting from abnormal operation.

As a consequence, a power system with low inertia results in poorer security of supply, even in the Belgian case, i.e an interconnected grid at the European scale [5]. Indeed, lower inertia causes higher RoCoF, and thus unnecessary tripping of RoCoF relays can occur and cause cascading effects [2]. Here are some frequency issues to deal with :

Cascaded outages : The three steps of a cascaded outage are represented in FIGURE 1.3 : first a disruption, then the flow redistribution and finally a complete blackout [8]. A disturbance constrains a redistribution of the flow between the remaining lines, creating an overload on them. This overload of the lines may in turn disconnect them if the problem is not mitigated quickly, leading to a domino effect that results in a widespread blackout of the grid. A practical example of this domino effect is the disconnection of rotating machines, that were participating in the reduction the frequency drop, and their loss results here in an even more severe drop in frequency.

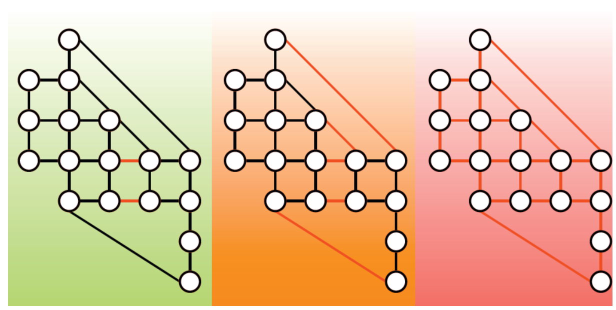

FIGURE 1.3: Cascaded outages representation [8]

Under Frequency Load Shedding (UFLS) : in order to mitigate the imbalance between production and consumption, a solution is to disconnect a certain quantity of loads until the frequency has returned to its nominal value [9]. According to Sibelga [10], this solution is to be used as a last resort. Indeed, other solutions exist to cope with imbalance [10] : increase or decrease the electricity production consequently, pay industrial customers to adapt their consumption or import from neighbouring countries.

1.4 Reminder on primary, secondary and tertiary control

Inertial response previously mentioned happens in the first seconds (typically less than 10 seconds) just after the active power imbalance, and helps to counteract frequency deviation until primary control takes over.

After this natural behaviour of the system, three control loops operate at different time scales [2], as depicted in FIGURE 1.4 :

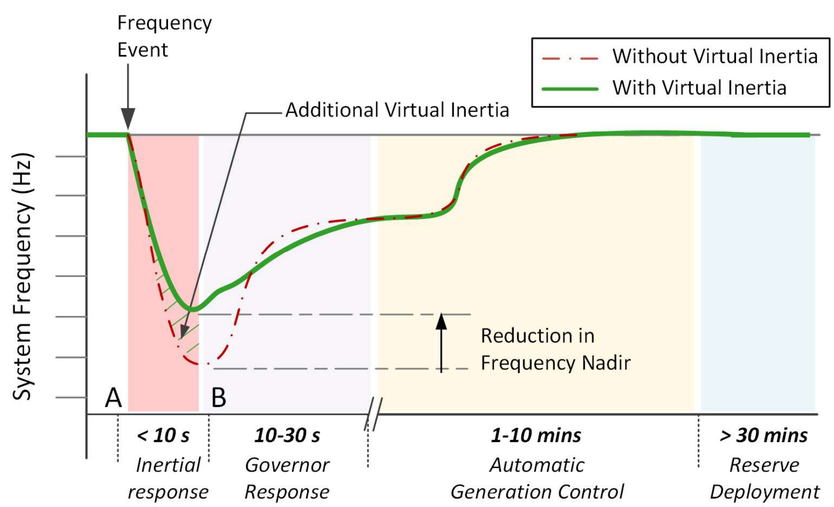

FIGURE 1.4: Different stages of frequency control on a power system [2]

- **Primary control (or Governor Response)**

  Primary control takes place in the first seconds after the inertial response, usually between 10 and 30 seconds. By adjusting the power injected by the machines through a coefficient proportional to the frequency deviation called the droop, the governor response allows to reduce the frequency deviation and establishes a new equilibrium before the action of secondary control. It is important to note that there is a static error for the new frequency equilibrium because the droop control is done by a proportional controller. Therefore, the new equilibrium after the primary control will be set at a different value than 50 Hertz. Droop control does not affect the initial RoCoF but changes the frequency nadir (i.e the minimum frequency point [2]) and the final frequency deviation.

- **Secondary Control (or Automatic Generation Control)**

  Then, within the next 1 to 10 minutes, the secondary control restores the grid frequency back to its nominal value of 50 Hertz by asking to contributing producers to adapt their electrical production. This is done thanks to a PI controller which cancels the power and frequency static error. More details will be given in SECTION 1.6.

- **Tertiary control (or Reserve Deployment)**

  At last, after 30 minutes and once the frequency is back to its nominal value, the tertiary control restores the secondary reserve for future disturbances. The tertiary control is done by changing the operating points of the generation units, disconnection of storage units and load control.

1.5 Virtual inertia concept to enhance grid frequency stability

The previous sections have discussed the net increase of RES in the electricity grid and the major consequence it has on the decrease of grid inertia and thus on the poorer grid inertial response. The goal of Virtual Inertia in this thesis is to reduce the RoCoF in the first instants after a power imbalance by injecting power quickly and properly. This would allow to lower the risks of unnecessarily activation of the protection systems, which can greatly affect the stability of the power network and sometimes lead to blackouts.

The concept of virtual inertia and more precisely virtual synchronous machine first appeared in 2007 with Beck and Hesse [11]. Virtual inertia allows energy sources that can not normally provide inertia to the grid to emulate the behaviour of a synchronous machine. This is done by connecting the DC side of this type of generation to the grid through inverters controlled to inject power in response to a frequency disturbance. This Virtual Inertia response must take place within the 10 first seconds after an imbalance to contribute to the inertial response. There are many control algorithms that will be presented later, but a simple overview of this concept is shown in FIGURE 1.5. Virtual Inertia emulation makes it possible to compensate for the loss of network inertia due to the increase in the penetration rate of renewables by interfacing them adequately. Thus, RES can help solving the problem they initiated. This virtual inertia would allow to reduce the RoCoF, frequency nadir and the final frequency deviation, avoiding then several issues specified in SECTION 1.3.

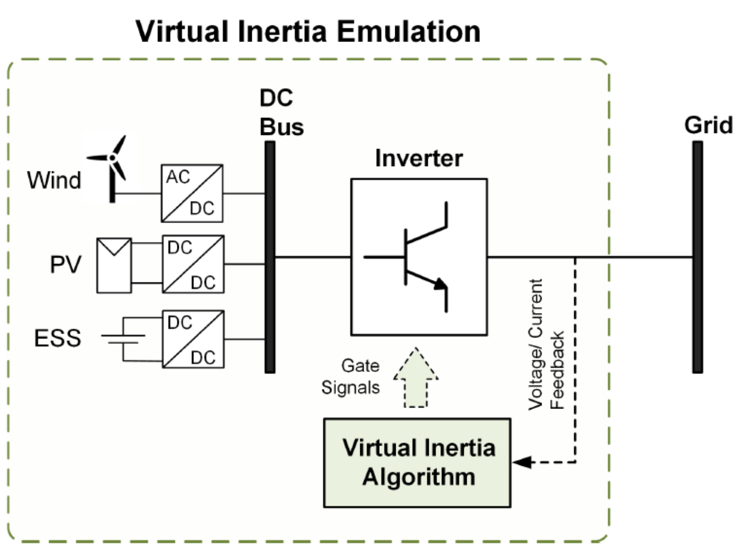

FIGURE 1.5: Concept of Virtual Inertia [2]

Basically, as seen in FIGURE 1.5, Virtual Inertia is made of three components [2]:

1. An energy source
2. Power electronics converters
3. Control algorithm

Energy Source The different energy sources that will be discussed in this thesis are renewable energy sources, specifically photovoltaic panels and wind turbines. Currently, these RES are operating at Maximum Power Point (MPP) such that no additional power can be used to provide virtual inertia. Several alternatives exist in order to be able to provide inertia : either by adding an Energy Storage System (ESS), or by operating under the MPP, to be able to inject more power during an imbalance event. The latter is called "de-loaded" operation. These topics will be more detailed in SECTION 6.1.1.

All these energy sources must fullfill two important criteria [2] :

- As said previously, their virtual inertia action must take place within the first seconds after a power imbalance in order to influence significantly the inertial response of the system.
- They must operate autonomously.

In FIGURE 1.5, RES are represented here in a simplified way, by a DC bus representing the DC-side of a PV panel AC-DC converter, or the DC-side of a Wind Turbine back-to-back converter or simply an energy storage system.

Power electronics converters: the details of power electronics converters will not be addressed in this thesis. Indeed, the goal of the thesis is to analyze the grid behaviour at a national scale and thus the in-depth functioning of power converters is not relevant in this context.

Algorithm controls: the different existing control algorithms will be detailed in CHAPTER 2.

1.6 Primary and secondary control global mechanisms

In order to understand what lies behind the several controls taking place in the frequency regulation, this section will explain the main equations helping to understand the primary and secondary control. Moreover, this theory will be helpful in order to cross-check simulation results with the theoretical expectations. All the equations detailed for primary and second control are coming from [13].

1.6.1 Primary Control

Droop control

As said previously, the droop control allows the machines to adjust their power proportionally to a frequency deviation through *the droop coefficient S*, in a linear way such that :

$$P_m = P_m^0 - \frac{P_N}{S}\frac{f - f_0}{f_0} \tag{1.5}$$

For a multi-machines system, it becomes :

$$P_m = \sum_{i=1}^{N} P_{mi}^0 - \frac{f - f_0}{f_0}\sum_{i=1}^{N}\frac{P_{Ni}}{S_i} \tag{1.6}$$

In this section, P_c will refer to power consumption of the grid, including system losses. P_m refers to power produced by machines.

Load variation

Let us consider a variation of loads in the grid, with loads that have a frequency dependency to be more general. This frequency dependency is represented by coefficient K_{pf} in *Equation* 1.7 :

$$P_c = P_c\left(1 + K_{pf}(f - f_0)\right) \tag{1.7}$$

The change of load power consumption can be expressed as : $P_c^0 \longrightarrow P_0^c + \Delta P_c^0$.
Taking into account the droop control of the machines and the frequency dependency of the loads, their power can be expressed as :

$$\begin{cases} P_m = P_m^0 - \dfrac{\Delta f}{f_0}\displaystyle\sum_{i=1}^{N}\frac{P_{Ni}}{S_i} \\ \\ P_c = P_c^0 + \Delta P_c^0 + P_c^0 K_{pf}\Delta f \end{cases} \tag{1.8}$$

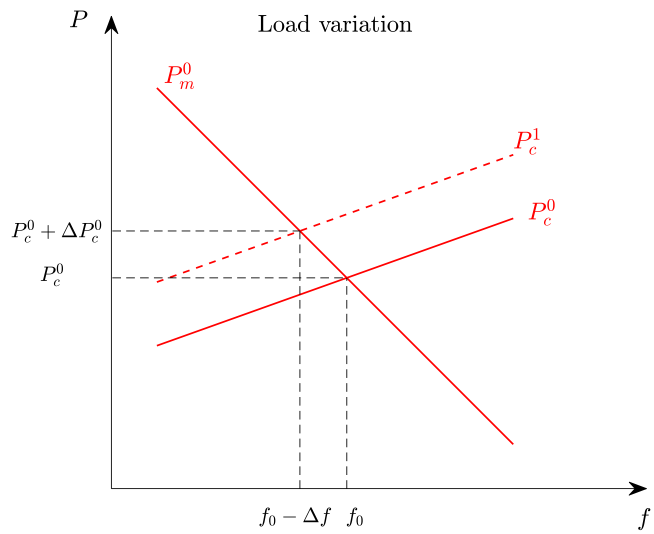

FIGURE 1.6: Droop response of a multi-machines system after a load variation [13]

As said previously, the primary control allows to reach a new steady-state equilibrium by controlling the injected power from the machines, to reach the power needed by the grid at different frequencies than the nominal one. The new equilibrium is at the intersection of the two straight lines :

$$P_c^0 + \Delta P_c^0 = P_m^0 + \Delta P_m^0 \tag{1.9}$$

Since at the initial equilibrium $P_m^0 = P_c^0$, *Equation* 1.9 reduces to:

$$\Delta P_m^0 = \Delta P_c^0 \tag{1.10}$$

By developing both side of the equation and rearranging terms, the frequency deviation between initial state and new equilibrium after primary control can be computed in *Equation* 1.11 :

$$-\frac{\Delta f}{f_0}\sum_{i=1}^{N}\frac{P_{Ni}}{S_i} = \Delta P_c^0 + P_c^0 D\Delta f = \Delta P_c^0 + P_m^0 D\Delta f \tag{1.11}$$

$$\boxed{\Delta f = \frac{-\Delta P_c^0}{P_m^0 K_{pf} + \dfrac{1}{f_0}\displaystyle\sum_{i=1}^{N}\frac{P_{Ni}}{S_i}}} \tag{1.12}$$

Loss of one generator

Let us now consider the loss a generator without any change in the load. However, they still have a frequency dependency. This change can be expressed as : $P_m^0 \longrightarrow P_m^0 - P_k$
Taking into account the droop control of the machines and the frequency dependency of the loads, their power can be expressed as :

$$\begin{cases} P_m = \sum_{i \neq k}^{N} P_{mi}^0 - \frac{\Delta f}{f_0} \sum_{i \neq k}^{N} \frac{P_{Ni}}{S_i} = P_m^0 - P_k - \frac{\Delta f}{f_0} \sum_{i \neq k}^{N} \frac{P_{Ni}}{S_i} \\ P_c = P_c^0 + P_c^0 K_{pf} \Delta f \end{cases} \tag{1.13}$$

Note that the sum includes all generators except generator k, since it is this machine that is lost.

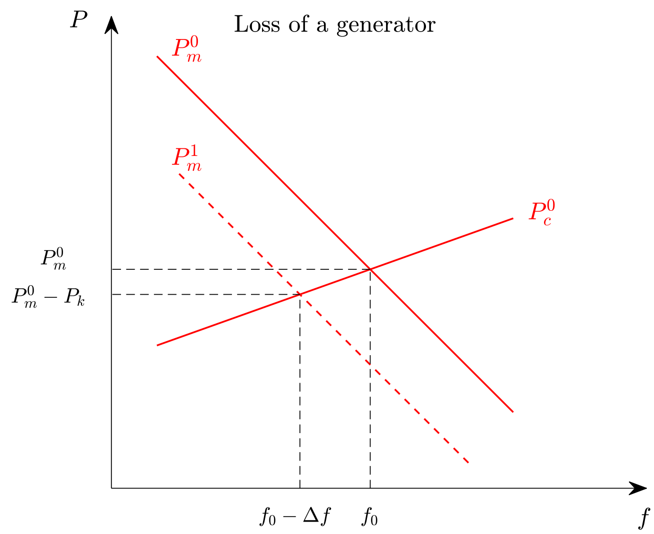

FIGURE 1.7: Droop response of a multi-machines system after a generator loss [13]

Again, thanks to primary control which adjusts injected power from machines, a new power-frequency equilibrium is reached at the intersection of production and consumption, at a new frequency $f = f_0 - \Delta f$:

$$P_m = P_c \tag{1.14}$$

Since at the initial equilibrium $P_m^0 = P_c^0$, *Equation* 1.14 reduces to:

$$-P_k - \frac{\Delta f}{f_0} \sum_{i \neq k}^{N} \frac{P_{Ni}}{S_i} = P_m^0 K_{pf} \Delta f \tag{1.15}$$

By developing both side of the equation and rearranging terms, the frequency deviation between initial state and new equilibrium after primary control can be computed in *Equation* 1.16 :

$$\boxed{\Delta f = \frac{-P_k}{P_m^0 K_{pf} + \frac{1}{f_0} \sum_{i \neq k}^{N} \frac{P_{Ni}}{S_i}}} \tag{1.16}$$

1.6.2 Secondary Control

Given that the secondary control will not appear neither in the modelling of the grid nor in simulations, this part will be less detailed. However, it is important to understand what takes place after the primary control to reach again the nominal frequency. For the following explanations, let us consider a simple two-area system with one interconnection between areas. The main metric to achieve the secondary control is the **A**rea **C**ontrol **E**rror. It can be expressed as [13] :

$$\begin{cases} \text{ACE}_1 = G_1 = P_{12} - P_{12}^0 + K_{s1}\left(f - f_n\right) = \Delta P_{12} + K_{s1}\Delta f \\ \\ \text{ACE}_2 = G_2 = P_{21} - P_{21}^0 + K_{s2}\left(f - f_n\right) = -\Delta P_{12} + K_{s2}\Delta f \end{cases} \tag{1.17}$$

Where :

- ΔP_{12} is the interconnection power variation
- K_{si} are parameters proportional to frequency deviation

The production setpoint of the generators contributing to secondary control are adapted via a PI control. The input is the ACE and the ouput is the production setpoint adjustment [13]:

$$\begin{cases} \Delta P_1^0 = \dfrac{1}{T_1}\displaystyle\int G_1 \text{dt} + \beta_1 G_1 \\ \\ \Delta P_2^0 = \dfrac{1}{T_2}\displaystyle\int G_2 \text{dt} + \beta_2 G_2 \end{cases} \tag{1.18}$$

Where :

- T_i is the time constant of the controller integral part
- β_i is the coefficient of the controller proportional part.
- G_i is the ACE in each area.

The distribution between contributing generators of each area is achieved by weighting the total production according usually to technical or economical criteria. [13].

$$\begin{cases} P_i^0 \longrightarrow P_i^0 - \rho_i \Delta P_1^0 \qquad \text{i} \in \text{area 1}, \quad \displaystyle\sum_{\text{i} \in \text{area 1}} \rho_i = 1 \\ \\ P_j^0 \longrightarrow P_j^0 - \rho_j \Delta P_2^0 \qquad \text{j} \in \text{area 2}, \quad \displaystyle\sum_{\text{j} \in \text{area 2}} \rho_j = 1 \end{cases} \tag{1.19}$$

If the PI controller performs its task properly, both ACE reach a zero value after a certain time (the integral part of the PI ensures a zero static error).

$$\left.\begin{cases} \text{ACE}_1 = 0 \longrightarrow \Delta P_{12} + K_{s1}\Delta f = 0 \\ \\ \text{ACE}_2 = 0 \longrightarrow -\Delta P_{12} + K_{s2}\Delta f = 0 \end{cases}\right\} \Longrightarrow \Delta f = 0 \text{ and } \Delta P_{12} = 0 \tag{1.20}$$

Broadly speaking, this is how secondary control is achieved in order to reach again the nominal frequency.

1.6.3 General overview

FIGURE 1.8 summarizes both primary and secondary control : when a sudden imbalance appears, the rotating machines adapt their power production to reduce the imbalance and to reach a better equilibrium than without primary control. Once this equilibrium has been reached, the secondary control takes over and sends through the PI control the new production setpoints to contributing generators in order to recover the nominal frequency.

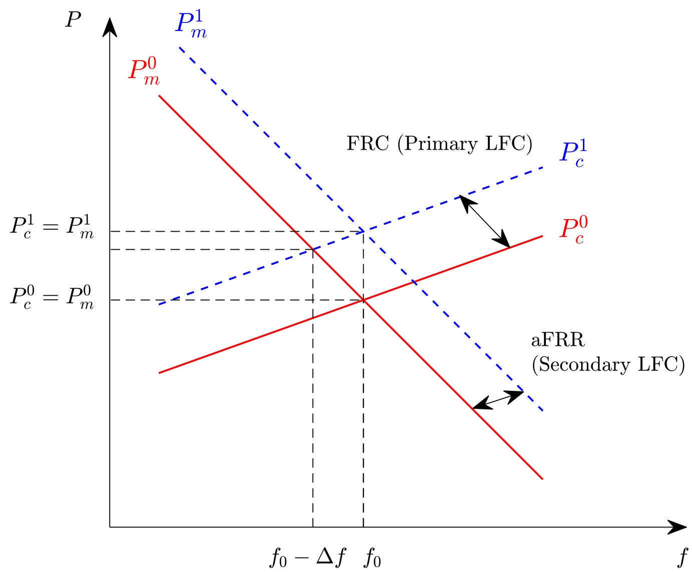

FIGURE 1.8: Primary and Secondary Control Overview [13]

1.7 Thesis outline

This thesis aims to study the benefits of the installation of virtual inertia devices to improve the Belgian High Voltage grid stability, from an inertial and primary control point of view. The goal is to analyse the contribution of virtual inertia in the current context of the rise of RES. More precisely, the objective is to quantify the RoCoF reduction provided by Virtual Inertia. To this end, the analysis will be divided in several parts.

The second chapter is devoted to a global overview of the state-of-the-art concerning the main virtual inertia control algorithms. This chapter will allow us to to choose among these control algorithms to model the virtual inertia system in our simulations.

The third chapter first justifies the algorithm choice for virtual inertia control before describing the different parts of the latter, as well as simplifications made with the aim of saving computational time.

Thereafter, the fourth chapter is dedicated to the modelling of the Belgian High Voltage Grid. It includes first the description of the several means of electricity production, such as Nuclear Power Plants, CCGT Power Plants, or Offshore Wind Farm. Then, this chapter addresses an overview of the power interconnections with neighbouring countries. A simplified model for the synchronous generators used for modelling the power plants will be explained, before detailing the simplified model of Offshore Wind Farm. Finally, the modelling of the power lines and the loads constituting the downstream distribution grid will be described.

Once the entire network and virtual inertia have been modeled, the fifth chapter will cover the results of the simulations achieved thanks to the *SimPowerSystems* library from SIMULINK. First, a parametric analysis of the VSG parameters identifies the influence of each parameter on the grid frequency behaviour and allows to choose the right parameters. Thereafter, several realistic scenarios are studied : the loss of a generator, a sudden load increase in the distribution grid and finally the grid behaviour with the increase of RES penetration rate degrading the frequency stability.

To conclude this thesis, an economical analysis of the virtual synchronous generator will be done. The storage costs of BESS and deloaded RES will be studied as well as the revenues from the ancillary services provided. These several technologies will be compared using different financial parameters as the net present value and the levelized cost of storage.

At last, some perspectives for further studies on the virtual synchronous generator will be proposed.

Chapter 2

Synthetic review of Virtual Inertia algorithms

In order to model the Virtual Inertia emulation with SIMULINK, it is important to study the main virtual inertia topologies before choosing the most convenient for the thesis simulations. Indeed, it is necessary to analyze the complexity of each algorithm as well as its advantages and disadvantages in order to be able to make a justified choice that meets the criteria of the thesis. These criteria are, among others, an implementation simple enough to limit the computational time, as well as parameters allowing a physical intuition when looking at their influence.

2.1 Global overview

The basic principle of virtual inertia is the same for all topologies. The difference between them lies in the complexity of each model of SG and how accurately the different models imitate the behaviour of the synchronous machine.

FIGURE 2.1 synthesizes the main topologies discussed in the literature.

There are four main topologies we will focus on, it is a non exhaustive but quite representative list. We will focus on one topology of each category :

- Synchronous generator model based : *Synchronverter*
- Swing equation based : *ISE Lab's topology*
- Frequency-power response based : *Virtual Synchronous Generator*
- Droop-based approach

The algorithm presented in this section only focus on the grid-side DC/AC converter control. This converter is connected to a DC bus which represents the energy source that provides the power used for Virtual Inertia emulation, as mentioned in SECTION 1.5.

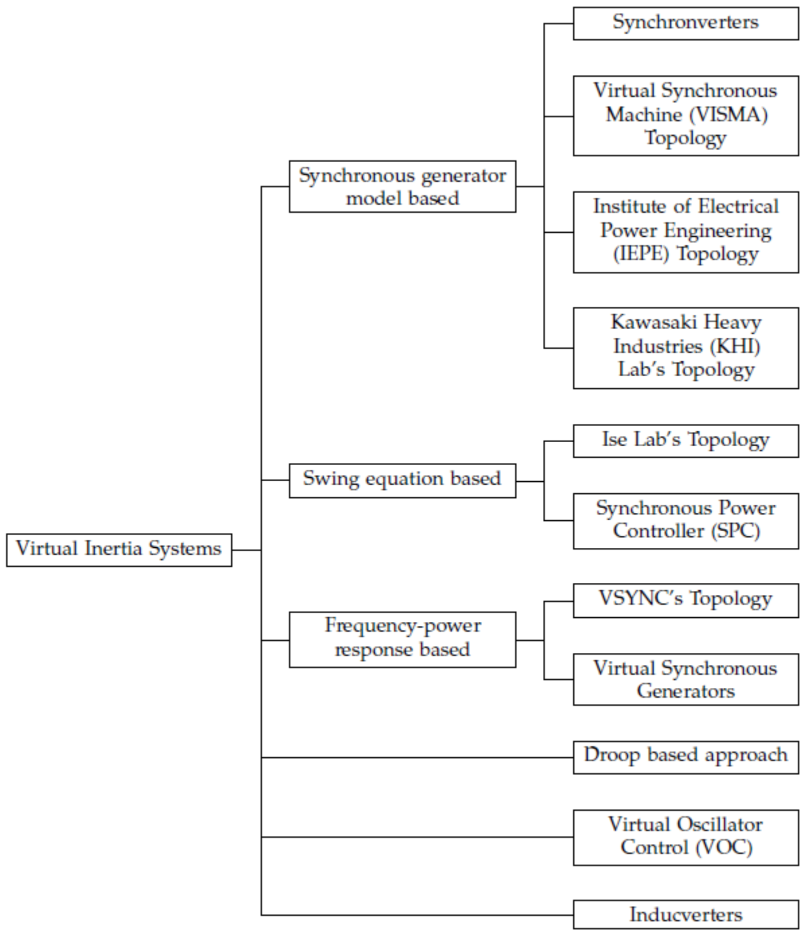

FIGURE 2.1: Classification of existing topologies for virtual inertia [2]

2.2 Synchronverters

2.2.1 Fundamentals and concepts

The principal concept behind this topology is to reproduce exactly the same frequency dynamics as a SG from the grid point-of-view, by applying the detailed equations of the SG.
Here is the set of equations used in the control of the synchronverters, in order to reproduce the dynamics of SG [2] :

$$T_e = M_f i_f < \mathbf{i}, \mathbf{sin}\theta > \tag{2.1}$$

$$e = \dot{\theta} M_f i_f \mathbf{sin}\theta \tag{2.2}$$

$$Q = -\dot{\theta} M_f i_f < \mathbf{i}, \mathbf{cos}\theta > \tag{2.3}$$

$$\ddot{\theta} = \frac{1}{J}(T_m - T_e - D_p \dot{\theta}) \tag{2.4}$$

Where T_e is the electromagnetic torque of the synchronverter, M_f is the mutual inductance between the field and stator windings, i_f is the field excitation current and θ is the angle between the rotor axis and one of the phases of the stator windings. e is the no load voltage, and finally Q is the generated reactive power [2].

$$\mathbf{i} = \begin{bmatrix} i_a \\ i_b \\ i_c \end{bmatrix} ; \quad \widetilde{\mathbf{sin}}\theta = \begin{bmatrix} \sin\theta \\ \sin\left(\theta - \frac{2\pi}{3}\right) \\ \sin\left(\theta - \frac{4\pi}{3}\right) \end{bmatrix} ; \quad \widetilde{\mathbf{cos}}\theta = \begin{bmatrix} \cos\theta \\ \cos\left(\theta - \frac{2\pi}{3}\right) \\ \cos\left(\theta - \frac{4\pi}{3}\right) \end{bmatrix} \tag{2.5}$$

More developments are available in [14].

2.2.2 Topology

In order to perform the control of the synchronverter, the discretized *Equations* 2.1, 2.3 and 2.5 are solved in order to generate e, T_e and Q. There are two control loops :

Frequency loop :

1. From active power reference P^*, T_m is computed thanks to the nominal frequency of the grid and is used (in combination with T_e) in order to compute virtual angular frequency ω.
2. This virtual angular frequency is then integrated to find the phase angle θ sent to the PWM block which generates, with e, the gating signals to control inverters.

D_p and J are respectively the damping factor and the moment of inertia of synchronverter. It is very important to choose wisely these parameters because they have a significant influence on the stability of the system [15].

Voltage loop : the error signal in this loop is the difference between reference reactive power, synchronverter reactive power computed with *Equation* 2.5 and a third signal which is the difference $v - v^*$ multiplied by a droop constant D_q. This error signal is passed through an integrator in order to compute $M_f i_f$ term in the equations set.

The output signals of the whole control block are e and θ, which are sent to the PWM block in order to generate gating signals which control the inverter. Here are the block diagrams of this topology in FIGURE 2.2 :

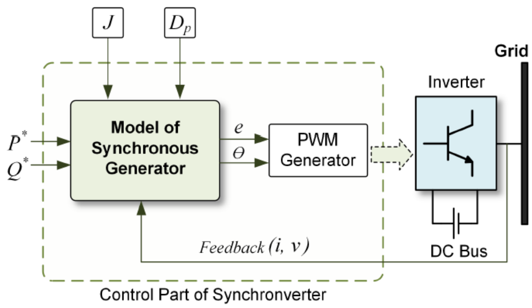

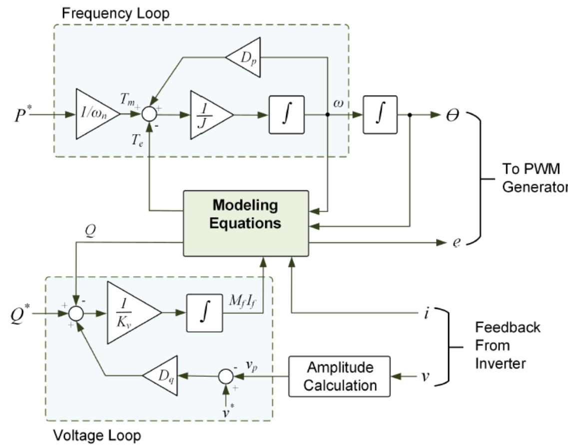

FIGURE 2.2: Left : global diagram. Right : Detailed block diagram of the system, with both voltage and frequency loop. [2]

2.2.3 Advantages and disadvantages

This topology presents several advantages [2]:

- The topology operates as a voltage source, so synchronverters can act as grid-forming units, often useful in micro-grids or DG not connected with the main grid. As a reminder, the role of grid forming units is to generate the voltage and frequency references for the whole microgrid by acting as an ideal voltage source. In this regard, they differ from the grid-feeding converters which only injects active power into the grid as an ideal current source, and from grid-supporting converters which can provide power, voltage and frequency regulation [16][17].
- The fact that RoCoF is not used in the control of the synchronverter is a good thing for the noise in the system, since derivatives tend to often introduce that kind of problem.
- From a grid operator point of view, the power system management does not change a lot since this topology tries to mimic as accurately as possible the exact behaviour of the SM, so the grid architecture does not need to be significantly adapted.

It also implies some disadvantages, that should not be neglected [2] :

- Complexity of differential equations can introduce numerical instabilities.
- Voltage-source architecture implies that there must be external protection systems in order to protect the system against large grid transients since this operation is not achieved with voltage-source architecture.
- PLL introduces risk of instabilities in weak grids [19], [20] (i.e grids where their Thevenin equivalent deviates from an ideal voltage source because they have a non-zero impedance which makes it more sensitive to variation of loads [18]. This non-zero grid impedance can generate coupling effects between the grid and the PLL, causing grid instabilities [21]). However, there are more developed models, such that self-synchronized synchronverters, which can cope with this kind of problem by avoiding the use of PLL [22] .

2.3 Swing equation based topology

In order to explain this topology, a model from ISE Lab is used.

2.3.1 Topology

This topology does not necessitate the full detailed set of equations of the SG, unlike synchroverters. Here, inertia is emulated thanks to a simpler equation, the swing equation, with an added term to model the effect of the damper windings :

$$P_{in} - P_{out} = J\omega_m \left(\frac{d\omega_m}{dt}\right) + D_p \Delta\omega \tag{2.6}$$

With P_{in} and P_{out} the input and output power of the inverter, ω_m the virtual angular frequency, and ω_g the grid angular frequency. The J and D_p parameters are respectively the moment of inertia and damping factor.

Control algorithm [2]

1. P_{out} is measured thanks to voltage and current measurement of the grid
2. ω_g is computed through a PLL
3. Input power P_{in} is computed thanks to a first order model of governor with gain K and time constant T_d, as described in FIGURE 2.3. This governor models the behaviour on how the system injects power in response to a frequency change.
4. By knowing P_{in}, P_{out}, J and D_p, the *Equation* 2.6 is solved at each discrete cycle in order to compute virtual angular frequency ω_m.
5. Virtual mechanical angle θ_m is found by integration, $\theta_m = \int_t \omega_m$
6. Voltage reference e is generated for example thanks to a $Q - v$ droop-control combined with a PI. [23]

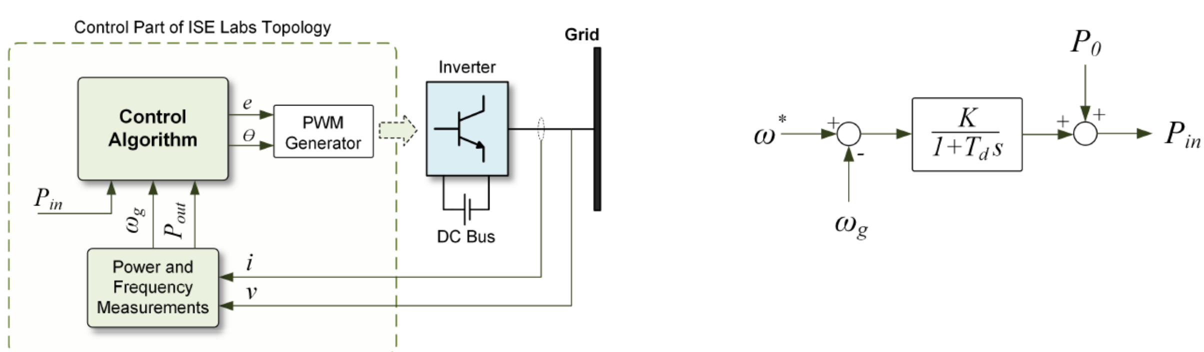

FIGURE 2.3: Swing equation block diagram and governor model [2]

2.3.2 Advantages and disadvantages

Swing equation based topology has several advantages : [2]

- Not introducing RoCoF in the control algorithm avoids typical problems related to this one, i.e noise and difficulties for the control [2].
- This topology can be used as grid forming unit, since it is voltage-source converter (VSC).

It also implies some disadvantages, that should not be neglected :

- The choice of J and D_p is critical, and can cause numerical instabilities and oscillatory behaviour [24].
- Delay introduced in governor's model causes higher RoCoF and frequency deviation [2].

2.4 Virtual Synchronous Generator

2.4.1 Fundamentals and concepts

The idea of behind the VSG is to emulate the dynamic response of a real synchronous generator by using DG units combined with power electronics [25]. By introducing an energy storage and by properly controlling the active power flow through the inverter, it is possible to mimic the release of kinetic energy of the rotor of an synchronous generator and thus to create virtual inertia [26]. The goal is to achieve the same stability enhancements as with synchronous generators during frequency deviations [27].
The biggest advantage of the VSG compared to traditional droop controllers is that it provides dynamic frequency control on top of frequency regulation [2]. It can be seen as a current source which adjusts its output power in function of the frequency of the grid.
The output power of the VSG is expressed by *Equation* 2.7:

$$P_{VSG} = P_0 + K_D \Delta\omega + K_I \frac{d\Delta\omega}{dt} \tag{2.7}$$

Where P_0 represents the primary power through the inverter, $\Delta\omega$ represents the deviation in frequency from the nominal value and $\frac{d\Delta\omega}{dt}$ represents the rate of change of frequency. As for the coefficients, K_D is the damping constant and K_I is the inertia constant [27]. The inertia constant helps reducing the rate of change of frequency of the system during a disturbance and the damping constant helps returning the frequency to a new steady-state value after the disturbance.

2.4.2 Topology

The topology of the VSG is shown in FIGURE 2.4.

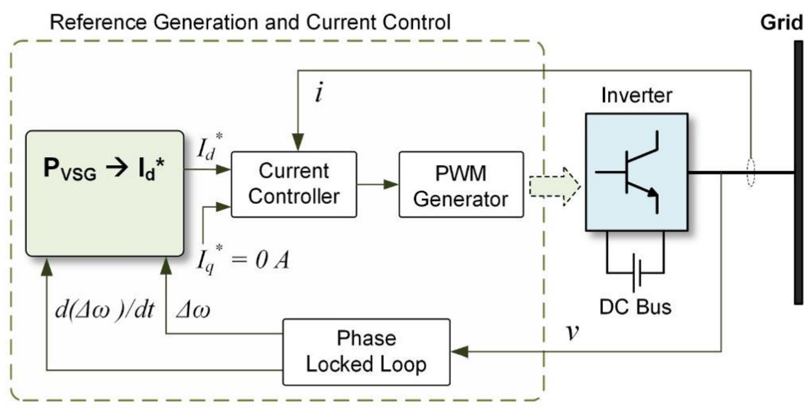

FIGURE 2.4: Topology of the Virtual Synchronous Generator [2]

First, a Phase-Locked Loop is used to determine the RoCoF and the frequency deviation of the grid.
Then, using *Equation* 2.7, the output power of the VSG is determined. This output power is commanded by a current controller and the choice was made to control it by using the d-q components of the current. Because we only have active power regulation ($I_q = 0$), the output of the VSG is controlled using *Equation* 2.8 [2].

$$I_d = \frac{2}{3}\frac{V_d P_{VSG} - V_q Q}{V_d^2 + V_q^2} \tag{2.8}$$

Finally, a gate signal is generated by the current controller for the inverter based on the grid current and the calculated current I_d. The inverter is thus a current-controlled voltage source [2].

2.4.3 Advantages and disadvantages

The VSG topology has several benefits [2]:

- Straightforward implementation : VSG has a similar physical behaviour to the real synchronous machine that makes it intuitively understandable.
- Inherent over-current protection : VSG use a current-source implementation for the inverter. Because the value of the current is controlled, the VSG topology ensures not having over-currents.

It also has several weaknesses [2]:

- Not suitable for islanded mode : in this mode, the virtual inertia unit has to act as a grid forming unit. As the VSG is current controlled, it can not act as grid forming because it can not provide a voltage reference for the grid.
- Instability due to PLL : PLL systems can provoke steady-state errors and instabilities, particularly in weak grids. Therefore, the PLL used in the VSG has to be robust and sophisticated for the topology to be successful.
- Sensitivity to noise : the VSG topology computes the RoCoF of the grid by derivation. This makes the VSG more sensitive to noise and can result into unstable activity.

2.5 Droop-based approach

The previous topologies explained in this review tried to mimic the behaviour of a real synchronous machine. The frequency droop-based approach is different and has been developed to operate autonomously in isolated micro grids [28]. Considering the impedance of the grid being dominated by inductance, the active power P is mainly dependent on the power angle [29].
The frequency droop control can be expressed as in *Equation* 2.9:

$$\omega_g = \omega^* - m_p(P_{out,LPF} - P_{in}) \tag{2.9}$$

By rearranging the terms, the power difference is expressed as :

$$P_{in} - P_{out} = \frac{1}{m_p}(\omega^* - \omega_g) + s\frac{T_f}{m_p}\omega^* \tag{2.10}$$

Where ω_g represents the local grid frequency, ω^* represents the reference frequency, P_{in} represents the reference active power, P_{out} is the active power measured at the output of the DG units and parameter m_p is the active power droop gain [2].

2.5.1 Topology

The frequency of the frequency-droop controller is shown in FIGURE 2.5.

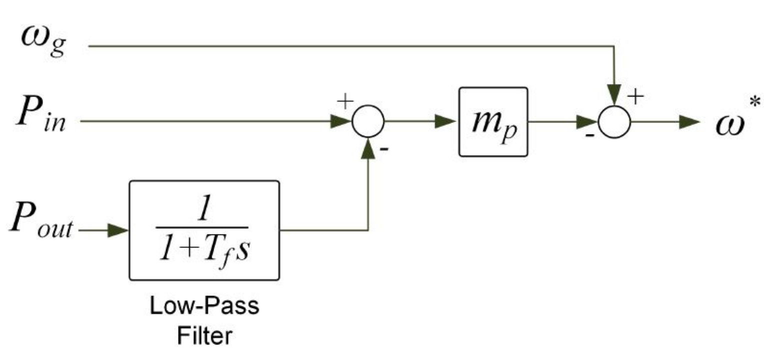

FIGURE 2.5: Topology of the droop-based controller [2]

As can be seen on the figure, a low-pass filter with time constant T_f is used for the output power measurement in order to filter the high-frequency noise of the power electronics [2]. Moreover, the time constant T_f of the first low pass filter on the output power measurement serves as an analogous function to simulate virtual inertia [30] [31], since it introduces the last term in *Equation* 2.10 which is proportional to the derivative of frequency. The delay introduced by the low pass filter is mathematically comparable to virtual inertia and the droop is comparable to damping [2].

2.5.2 Advantages and disadvantages

The droop-based topology has several advantages [32] [2]:

- Enhanced stability : by avoiding the use of a PLL we can avoid the instabilities typically introduced by this device.
- The concepts are equivalent to the droop of SG and thus intuitively understandable.

It also implies some disadvantages, that should not be neglected [2] :

- Slow transient response : the delay introduced by the low pass-filter results in a slow response.

2.6 Other Topologies

2.6.1 VISMA

The virtual synchronous machine, referred as VISMA, simulates the behaviour of a synchronous machine using inverter technology [33]. The VISMA can replicate the static and dynamics properties of a synchronous machine using a d-q frame implemented in the computer of a power inverter [2]. The VISMA computer transforms the measured instantaneous voltage of the grid into the instantaneous stator current of the virtual machine [33]. Then, the calculated stator current are injected by the inverter to the grid using a hysteresis current control. However, numerical instabilities can occur with the VISMA due to mathematical divergence using Euler's method in the computer algorithm [34].

2.6.2 IEPE's topology

The IEPE's topology is similar to the VISMA topology, except that it is operated as a voltage source [35]. Instead of using voltages as input and generating a current reference for the virtual synchronous machine, the IEPE's topology uses the current as input and generates a voltage reference [2]. Hence, it uses a PWM controller instead of a hysteresis controller. Moreover, in this topology, a low-pass filter is used for the measurement of the phase current. Then, because of the higher switching frequency of the PWM and the use of a low-pass filter in this technology, the voltages of the IEPE's topology have almost no harmonics [35]. Also, the IEPE's topology is able to build a three-phase voltage instantly after switching off from the grid and without needing hardware reconfiguration. Because of this features, the IEPE's topology is better suited for islanded operation.

2.6.3 SPC

The synchronous power converter has a similar structure for its general control algorithm as the Ise's lab topology but does not use a voltage controlled or current controlled converter as usual [2]. Moreover, the SPC is controlled by a cascade controller which is implemented with an inner current control loop and an outer voltage control loop [36]. This alternative control scheme enables a more robust performance against numerical instabilities, decreases sensitivity to the distortions from the electrical network and provides over-current protection [36].

2.7 Summary and comparative table

FIGURE 2.6 summarizes the pros and cons of each topology and will be used to make the choice of topology that will be implemented in this thesis.

Control Technique	Key Features	Weaknesses
Synchronous generator (SG) model based	• Accurate replication of SG dynamics • Frequency derivative not required • Phase locked loop (PLL) used only for synchronization	• Numerical instability concerns • Typically voltage-source implementation; no over-current protection
Swing equation based	• Simpler model compared to SG based model • Frequency derivative not required • PLL used only for synchronization	• Power and frequency oscillations • Typically voltage-source implementation; no over-current protection
Frequency-power response based	• Straightforward implementation • Typically current-source implementation; inherent over-current protection	• Instability due to PLL, particularly in weak grids • Frequency derivative required, system susceptible to noise
Droop-based approach	• Communication-less • Concepts similar to traditional droop control in SGs	• Slow transient response • Improper transient active power sharing

FIGURE 2.6: Comparative table between different topologies [2]

Chapter 3

Virtual Synchronous Generator

3.1 Choice motivation

We decided to implement the VSG topology because its advantages are relevant for the High Voltage Grid we are going to simulate. The similar inertial behaviour of the VSG topology to a real synchronous machine makes it intuitively understandable and facilitates the interpretation of each tuning parameter's impact. Also, the VSG provides an inherent over-current protection due to the current control of the inverter which other topologies like synchronverters, swing-based and droop-based do not provide.

Then, many of the downsides of the VSG have little influence when we only consider the high voltage grid. Indeed, the VSG is not suited for islanded mode but this is irrelevant for the high voltage grid analysis. Also, the instabilities introduced by the PLL are particularly important in weak grids and will thus have less impact in the strong high voltage grid we will analyze.

Moreover, the potential instabilities due to the PLL can be solved by using a robust and sophisticated PLL. Finally, the sensitivity to noise due to the derivative term of this topology will have little impact as we will see in the simulation results later on.

3.2 Theoretical approach

As seen previously, VSG is the combination of three elements : an energy storage, an inverter and a control mechanism. The VSG allows to make the energy storage act as a SG to the grid from the inertial and damping point of view [37]. The energy storage must be able to both inject and absorb power, so the SOC of the storage has to be at steady state at 50 $\%$ [37].
As seen in SECTION 2.4.1, the output power of the VSG is described by :

$$P_{VSG} = P_0 + K_I \frac{d\Delta\omega}{dt} + K_D \Delta\omega \tag{3.1}$$

P_0 is the steady state power of the inverter, the power exchanged when there is no frequency deviation.
The second term is proportional to the RoCoF. It is equivalent to a virtual mass since it emulates the inertial effect of synchronous machine. Since this term reacts to counteract the

RoCof, it allows to reduce it and thus to reduce the frequency deviation [37]. K_I is given by :

$$K_I = \frac{2HP_{VSG,N}}{\omega_0} \tag{3.2}$$

With H the inertia of the virtual generator, $P_{VSG,N}$ its nominal apparent power and ω_0 the nominal angular frequency of the grid.
Given that the steady-state RoCoF is zero, another term is needed in order to come back to an acceptable frequency. It is the goal of the third term in *Equation* 3.1, proportional to the deviation in frequency [37]. This term can be interpreted from two different point of views :

- Frequency regulation : it can be seen as the droop used in primary frequency regulation, which controls the mechanical torque in response to a change in frequency. It is a control feedback.

- Synchronous machine : K_D emulates the damper windings effect in an SG in order to suppress the oscillations of the electromagnetic torque when there is a frequency deviation. It is a natural behaviour of the machine.

Both representations produce the same effect but their interpretations are quite different. However, since the control of the VSG is only proportional, the new equilibrium will not be at nominal frequency. Indeed, with only a proportional controller, there is a static error. It is also the case with classical primary control, while secondary control will allow the system to come back to nominal frequency.
To summarize, K_I helps reducing the RoCoF which in turns reduces the frequency nadir during a power imbalance. Then, K_D reduces the frequency deviation of the new steady-state frequency after the power imbalance [37].
These two coefficients can be chosen such that maximum power is exchanged when both maximum frequency deviation and RoCoF occur [38]:

$$K_I = \frac{P_{VSG,N}}{\left(\dfrac{d\omega}{dt}\right)_{\text{max}}} \tag{3.3}$$

$$K_D = \frac{P_{VSG,N}}{(\Delta\omega)_{\text{max}}} \tag{3.4}$$

Notice that usually, a dead-zone is introduced to prevent from reacting to random noise due to measurement [39].
Another way to determine K_I is by imposing the desired time constant of the system τ_f [37]. Once K_D is computed we have:

$$\tau_f = \frac{K_I}{K_D} \tag{3.5}$$

Even though increasing K_I means adding a higher amount of inertia, there are some limits [37]:

- Increasing K_I results in a larger power overshoot during transients, so inverters have to cope with heavy overload.

- A high K_I can cause PLL instability

So there is a trade-off between these three aspects : virtual inertia, inverter overload and PLL stability [37].
Another way of determining K_I and K_D coefficients is to start from constitutive equations of frequency dynamics. Starting from the swing equation (with power in p.u):

$$\Delta\dot{\omega}_i = \frac{\omega_0^2}{2H_i\omega_i}\left(P_{mi} - P_{ei}\right) \tag{3.6}$$

The inertial part of injected power can be found by rearranging terms :

$$\Delta P(p.u) = \frac{2H_i\omega_i}{\omega_0^2}\Delta\dot{\omega}_i \quad \Leftrightarrow \quad K_I = \frac{2H_i\omega_i}{\omega_0^2}P_{VSG,N} \simeq \frac{2H_i}{\omega_0}P_{VSG,N}\left[\frac{MW\ s}{rad/s}\right] \tag{3.7}$$

With H_i the inertia emulated by the VSG.
The proportional part is found only by applying the definition of the droop D (p.u). Notice that we denote this by D instead of S to distinguish the droop of the VSG from the one of the SM governor. Knowing this, proportional part is :

$$\Delta P(p.u) = \frac{1}{D\omega_0}\Delta\omega \Leftrightarrow K_D = \frac{P_{VSG,N}}{D\omega_0}\left[\frac{MW}{rad/s}\right] \tag{3.8}$$

The total contribution of injected/absorbed power by VSG is expressed as :

$$\boxed{P_{VSG} = K_D\Delta\omega + K_I\frac{d\Delta\omega}{dt} = P_{VSG,N}\left(\frac{1}{D\omega_0}\Delta\omega + \frac{2H}{\omega_0}\frac{d\Delta\omega}{dt}\right)} \tag{3.9}$$

The advantage of this expression is to link coefficients to physical parameters (i.e inertia constant, droop of a machine), which is easier to interpret coefficients than with *Equations* 3.3 and 3.4.

Difference between conventional droop and VSG droop values

The droop approach for VSG and for primary control is the same since they achieve the same purpose. Given that the VSG does not inject any power at steady state in this analysis, the P-f characteristic is just shifted from $P_{m,0}^{set}$ to 0. If VSG injected power at steady-state (i.e if de-loaded PV or Wind Turbines are used), the characteristic would be around P_0. The shift of the characteristic is described in FIGURE 3.1 :

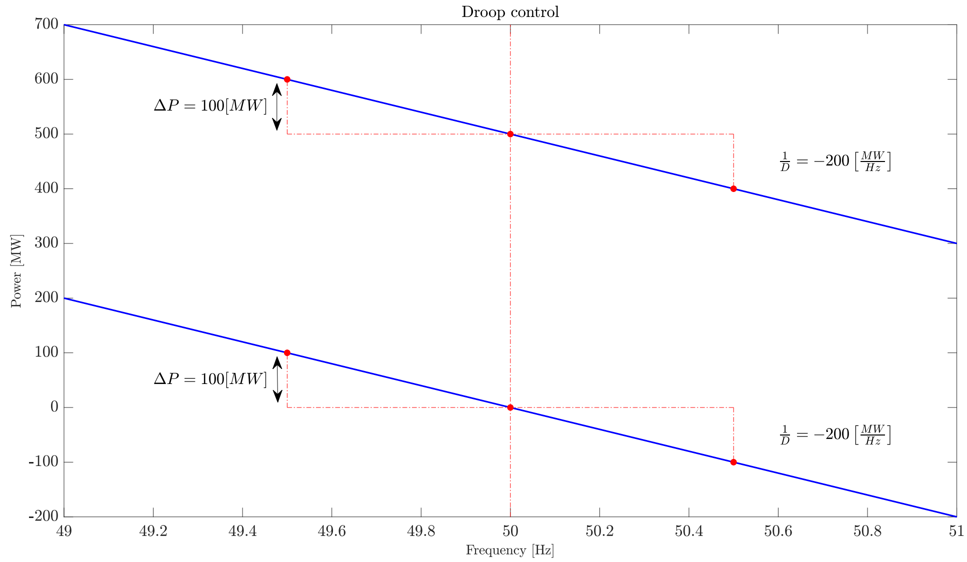

FIGURE 3.1: Droop control for both VSG and Synchronous Machine

As a reminder, the characteristic is given by :

$$P_m^{set,tot} = P_{m,0}^{set} + \Delta P_m^{set} = P_{m,0}^{set} - \frac{1}{S}\Delta f \tag{3.10}$$

For both cases, the SI droop (i.e the slope of the blue curve) remains the same, as shown in TABLE 3.1. In this example, for a frequency deviation $\Delta f = 0.5[Hz]$, power injected is $\Delta P = \pm 100[MW]$.

$$\boxed{S_{SI} = -\frac{f - f_0}{\Delta P_m^{set}} \quad \left[\frac{Hz}{MW}\right] \quad \Leftrightarrow \quad S(p.u) = -\frac{\frac{f - f_0}{f_0}}{\frac{\Delta P_m^{set}}{P_{m0}^{set}}} = S_{SI}\frac{P_{m0}^{set}}{f_0} \quad \left[\frac{p.u}{p.u}\right]} \tag{3.11}$$

The difference in droop value between the synchronous machines and the VSG may lie in the per uniting. Indeed, for primary control, P_{m0}^{set} is the steady-state power injected by the synchronous machines (here, 500 [MW]). However, for the VSG a consistent way to define P_{m0}^{set} is to define it as the maximum injected power (here 100 [MW]), since we assumed no steady-state injected power for VSG.

Droop comparison		
	Primary Control	**VSG**
P_{m0}^{set} [MW]	500	100
$S\,[Hz/MW]$	$\frac{1}{200}$	$\frac{1}{200}$
S (p.u)	5%	1%

TABLE 3.1: Difference in per unit values of droop

The result here is that for the same SI value, the SM per unit droop is 5 times bigger than the VSG per unit droop. The difference between these values may be even greater. This is why it is not surprising to have much smaller per unit droop values of the VSG than conventional ones in the next sections.

3.3 Control algorithm

This section describes the control algorithm of the VSG, as achieved in SIMULINK. A first VSG algorithm was presented in SECTION 2.4. The latter is slightly different from the SIMULINK implementation, due to some simplifications.

Indeed, the simulations were runned with the **phasor mode**. This implies that the electrical quantities (i.e voltage and currents) are expressed through phasors with magnitude and phase **at a fixed frequency**, here at 50 [Hz]. This makes electrical quantities independent from the grid frequency. The interest of this simulation mode is that by considering only phasor quantities, electrical equations initially described by differential equations through a state-space model are reduced to much simpler equations linking the several phasor quantities, i.e voltage and currents [40]. This greatly reduces the computational time and thus allows much faster simulations. However, it changes the way to compute the grid frequency.

Indeed, the PLL previously discussed in CHAPTER 2 used to track the grid frequency is not represented here. Since the electrical quantities are running at 50 [Hz], the only way to access to the frequency is through the synchronous speeds of the different synchronous generators. The frequency of the grid is thus computed as the sum of the synchronous speeds weighted by their respective nominal powers :

$$f_{grid} = \frac{1}{2\pi}\frac{\sum\limits_{i=1}^{N}\omega_i S_{Bi}}{\sum\limits_{i=1}^{N} S_{Bi}} \tag{3.12}$$

3.3.1 Global overview of the control algorithm

First, FIGURE 3.2 shows a simplified overview of the VSG control :

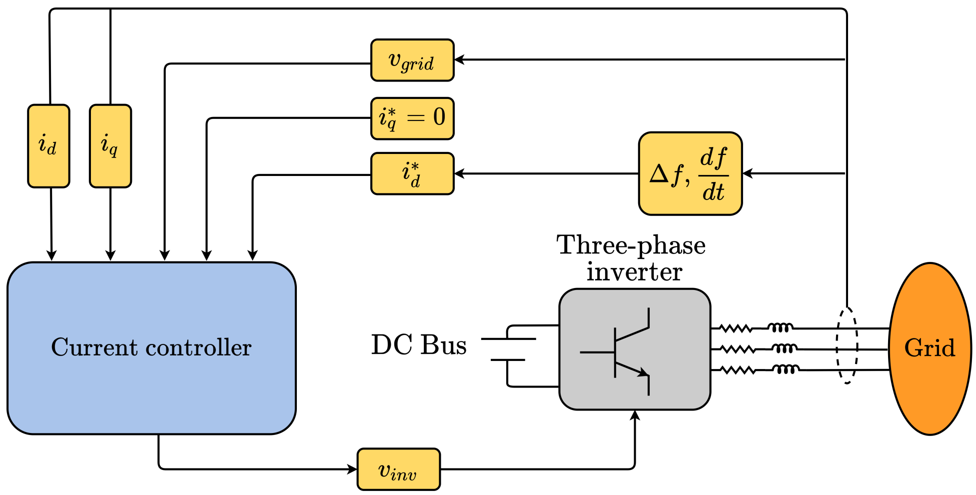

FIGURE 3.2: Global overview of control loop for VSG

The main principle of the VSG control is to adjust, through current control, the voltage of the converter-side w.r.t the grid-side voltage in order to inject in the grid the correct power imposed by the VSG.
The control can be described in a few steps (dq subscripts will be explained after the global overview). First, the current controller needs several inputs :

1. **Reference currents $\mathbf{i_d^*}$ and $\mathbf{i_q^*}$.** : through frequency measurement, P_{VSG} is computed according to *Equation* 3.9 and is translated in an i_d^* setpoint. Arbitrarily, i_q^* is set to 0.

2. **Grid voltages and currents:** from grid measurements, V & I are expressed in a dq frame to be used appropriately in the current controller.

The goal of the current controller is to provide as output the converter-side voltage. In a realistic algorithm, the current controller provides the output going into a PWM block which supplies the gating signals controlling the inverter. The PWM is not represented here and the considered simplification allows the current controller to generate directly the converter-side voltage without considering the complexity of power electronics. The following sections aim to study in more details each part of the Virtual Inertia control algorithm.

3.3.2 Grid voltage measurement

Before analyzing the operation of each block, it is important to specify that the voltage measurement is slightly modified in order to select only the voltage component we are interested in.

To this end, the positive sequence of the measured three-phase grid voltage is computed in order to suppress the non-symmetrical components of grid voltage. As a reminder, FIGURE 3.3 shows the decomposition of unbalanced voltage in its three components (French notation is used on the figure). In English, zero-positive-negative sequence (i.e 0-1-2 sequence) refers to d-i-o in French. It corresponds to "composantes directe, inverse et homopolaire" (subscript d has not to be confused with the d subscript used subsequently). This three components are computed thanks to Fortescue matrix :

$$\begin{pmatrix} v_0 \\ v_1 \\ v_2 \end{pmatrix} = \frac{1}{3} \begin{pmatrix} 1 & 1 & 1 \\ 1 & a & a^2 \\ 1 & a^2 & a \end{pmatrix} \begin{pmatrix} v_a \\ v_b \\ v_c \end{pmatrix} \tag{3.13}$$

$$v_1 = \frac{1}{3}\left(v_a + av_b + a^2 v_c\right) \qquad a = e^{j2\pi/3} \tag{3.14}$$

With $v_a,\ v_b,\ v_c$ are the phase-to-ground grid voltages. Even if our grid is supposed to be balanced from a voltage point-of view, extracting only the positive sequence allows to get rid of unwanted voltage components for the control.

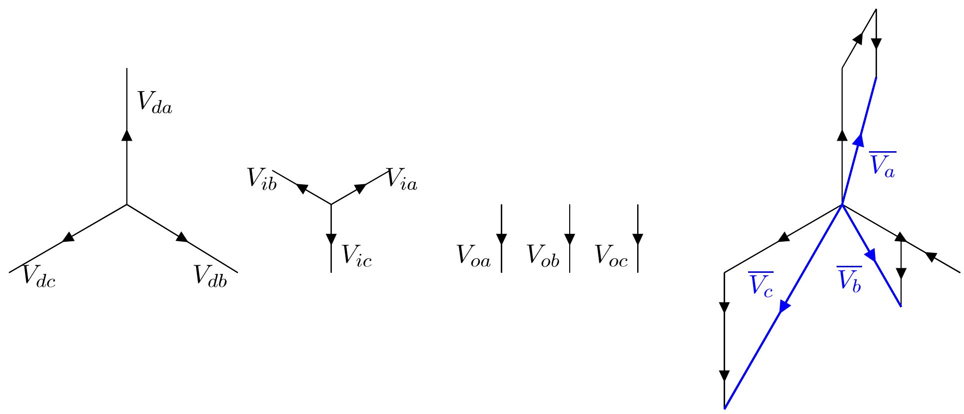

FIGURE 3.3: Decomposition of unbalanced voltage in its three components (French notation d-i-o : directe, inverse, homopolaire) [41]

Once this preliminary step has been done, the different parts of the control can be analysed. FIGURE 3.4 gives a more detailed diagram of how the algorithm works.

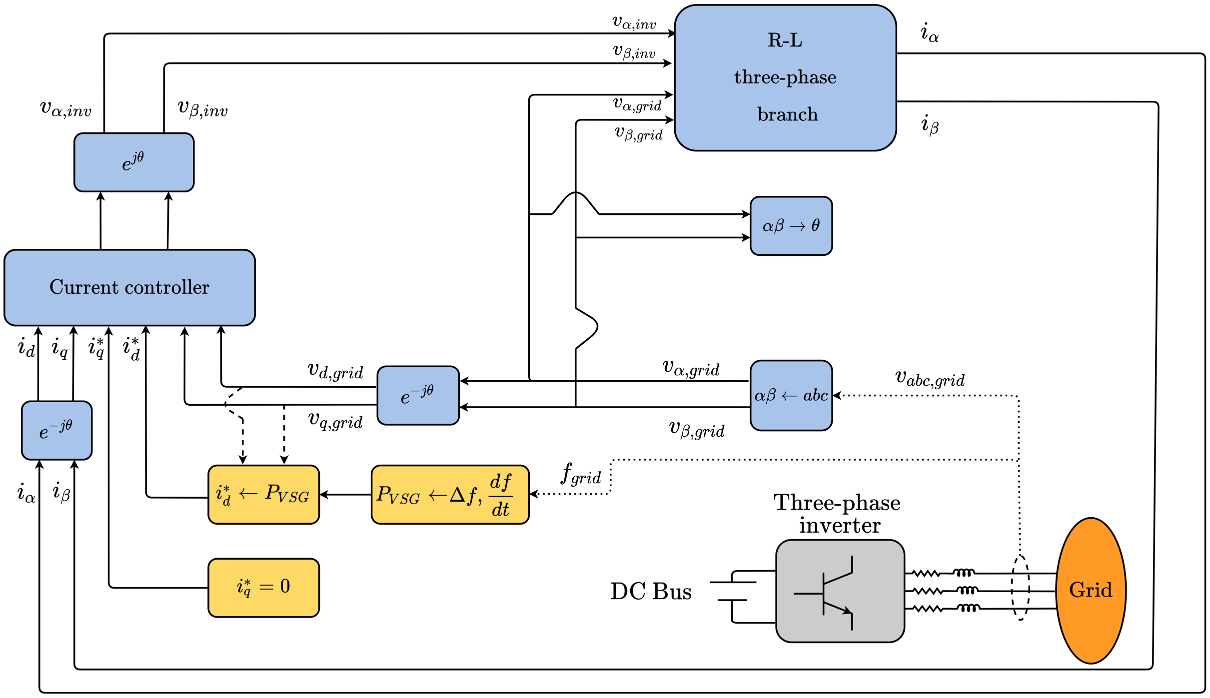

FIGURE 3.4: Detailed overview of control loop for VSG

3.3.3 Different coordinate systems

From the positive sequence component, Clarke's transform is applied in order to convert a three-phase system into a simpler two-phase system :

$$\begin{cases} v_\alpha = \mathbb{R}\{v_1\} \\ v_\beta = \mathbb{I}\{v_1\} \end{cases} \qquad \theta = \arctan\frac{v_\beta}{v_\alpha} \tag{3.15}$$

Then, in order to make d-axis aligned with the grid-side voltage, a d-q frame is used:

$$\begin{cases} v_d = v_\alpha e^{-j\theta} \\ v_q = v_\beta e^{-j\theta} \end{cases} \tag{3.16}$$

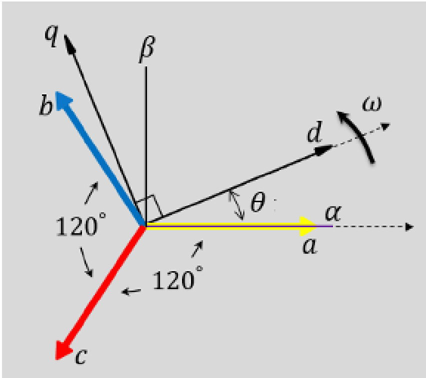

FIGURE 3.5: Representation of the different coordinate systems [42]

Electrical *abc* signals are here expressed in terms of phasors at 50 [Hz], while real ones can not be expressed as such since their frequency constantly changes.
Moving from a three-phase frame to a d-q frame is done by two different ways : for phasor mode, it is achieved with *Equations* 3.15 and 3.16. In reality, *abc* quantities are expressed in d-q frame with Park's transform :

$$\begin{bmatrix} x_d \\ x_q \\ x_o \end{bmatrix} = \sqrt{\frac{2}{3}} \begin{bmatrix} \cos(\theta) & \cos(\theta - \frac{2\pi}{3}) & \cos(\theta - \frac{4\pi}{3}) \\ -\sin(\theta) & -\sin(\theta - \frac{2\pi}{3}) & -\sin(\theta - \frac{4\pi}{3}) \\ \frac{1}{\sqrt{2}} & \frac{1}{\sqrt{2}} & \frac{1}{\sqrt{2}} \end{bmatrix} \begin{bmatrix} x_a \\ x_b \\ x_c \end{bmatrix} \tag{3.17}$$

These phasor and matrix representations of d-q frame are equivalent and represent the same reality, but are achieved by two different ways. It changes the way the algorithm is implemented.

3.3.4 Current controller

FIGURE 3.6 shows the connection between the inverter of the VSG and the grid, made of a LC filter.

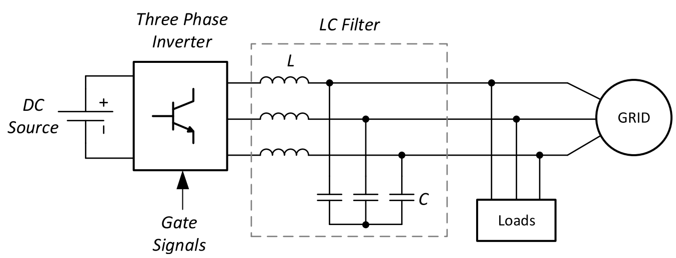

FIGURE 3.6: Schematic of grid connected inverter [43]

In order to be able to use linear control techniques, d-q frame is used to control the currents injected to the grid [39]. After converting the connection in this frame, circuits in FIGURE 3.7 can be used for the current control. Indeed, in this frame, AC quantities appears as DC quantities at steady-state [44].

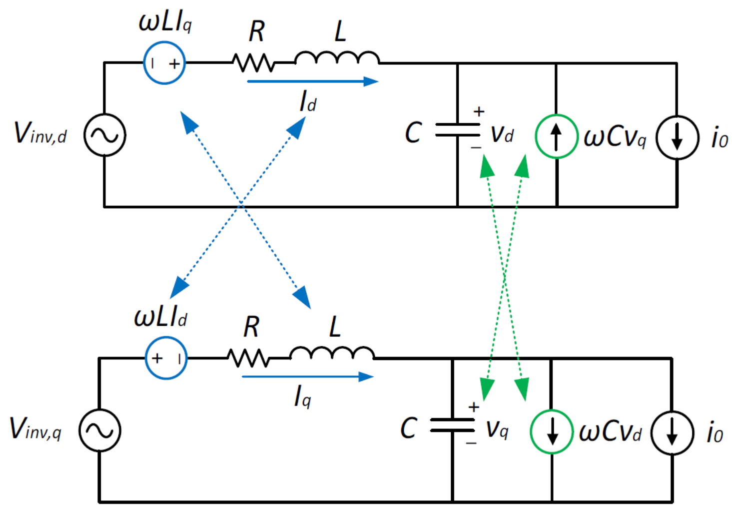

FIGURE 3.7: Park transform equivalent circuit of grid-connected inverter [43]

These equivalent circuits allow to compute reference currents i_d^* and i_q^* as follows [39]:

$$\begin{cases} i_d^* = \dfrac{2}{3}\left(\dfrac{v_d P_{VSG} - v_q Q_{VSG}}{v_d^2 + v_q^2}\right) \\ \\ i_q^* = \dfrac{2}{3}\left(\dfrac{v_d Q_{VSG} - v_q P_{VSG}}{v_d^2 + v_q^2}\right) \end{cases} \tag{3.18}$$

Where P_{VSG}, as discussed in SECTION 3.2, is given by :

$$P_{VSG} = K_D \Delta\omega + K_I \frac{d\Delta\omega}{dt} = P_{VSG,N}\left(\frac{1}{D\omega_0}\Delta\omega + \frac{2H}{\omega_0}\frac{d\Delta\omega}{dt}\right) \tag{3.19}$$

A saturation block has been put after the P_{VSG} setpoint to limit it to its nominal value. In this way, the current setpoint i_d^* is thus also limited. However, the equivalent circuits also allow to design the current controller represented in FIGURE 3.8:

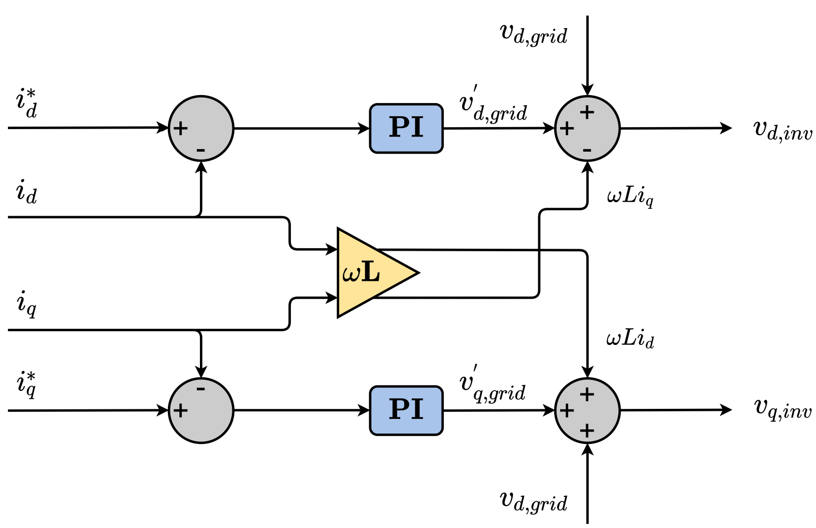

FIGURE 3.8: PI Controller

From this current controller, inverter d-q voltages are generated :

$$\begin{cases} v_{d,inv} = v_{d,grid} + v'_{d,grid} - \omega L i_q \\ v_{q,inv} = v_{q,grid} + v'_{q,grid} + \omega L i_d \end{cases} \tag{3.20}$$

3.3.5 Three-phase RL branch

In order to compute the injected/absorbed currents i_d and i_q from the VSG used in the current controller, here is the d-q axis model of a three-phase series R-L branch :

$$\begin{cases} v_{d,inv} - v_{d,grid} = Ri_d + L\dfrac{di_d}{dt} - \omega L i_q \\ v_{q,inv} - v_{q,grid} = Ri_q + L\dfrac{di_q}{dt} + \omega L i_d \end{cases} \tag{3.21}$$

By applying Laplace's transform and isolating i_d and i_q, it follows :

$$\begin{cases} i_d = \dfrac{\omega}{sL}\left(v_{d,inv} - v_{d,grid} - Ri_d - Li_q\right) \\ i_q = \dfrac{\omega}{sL}\left(v_{q,inv} - v_{q,grid} - Ri_q + Li_d\right) \end{cases} \tag{3.22}$$

3.3.6 Summary

In summary, by measuring grid-side voltages, the VSG algorithm generates via current control the inverter-side voltages in order to get the right injected/absorbed currents (and thus power) in the grid.

Chapter 4

Modelling of the grid

4.1 Belgium High Voltage Grid

As said in the introduction, the goal of this thesis is to observe the potential of virtual inertia on the Belgian High Voltage Grid. It is managed by the Belgian Transmission System Operator (TSO), Elia. Table 4.1 depicts the various voltage levels that exist on the Belgian grid : here, the grid modelling is limited to the extra-high voltage level, i.e 380 [kV]. In practice, Elia's grid ends at 30 [kV], where the distribution grid begins. However, the analysis is restricted to the 380 [kV] level.

Voltage levels on Belgian Grid	
Level	**Voltage [kV]**
Extra-High Voltage (EHV)	$U_n > 230$
High Voltage (HV)	$35 < U_n < 230$
Medium Voltage (MV)	$1 < U_n < 35$
Low Voltage (LV)	$U_n < 1$

Table 4.1: Description of existing voltage levels according to standard IEC 60038

This specific grid and neighbouring lines are highlighted in red in Figure 4.1. The only exception concerning the voltage level restriction is for the Offshore Wind connection : indeed, this one is connected to BHVG through a 220 [kV] line.

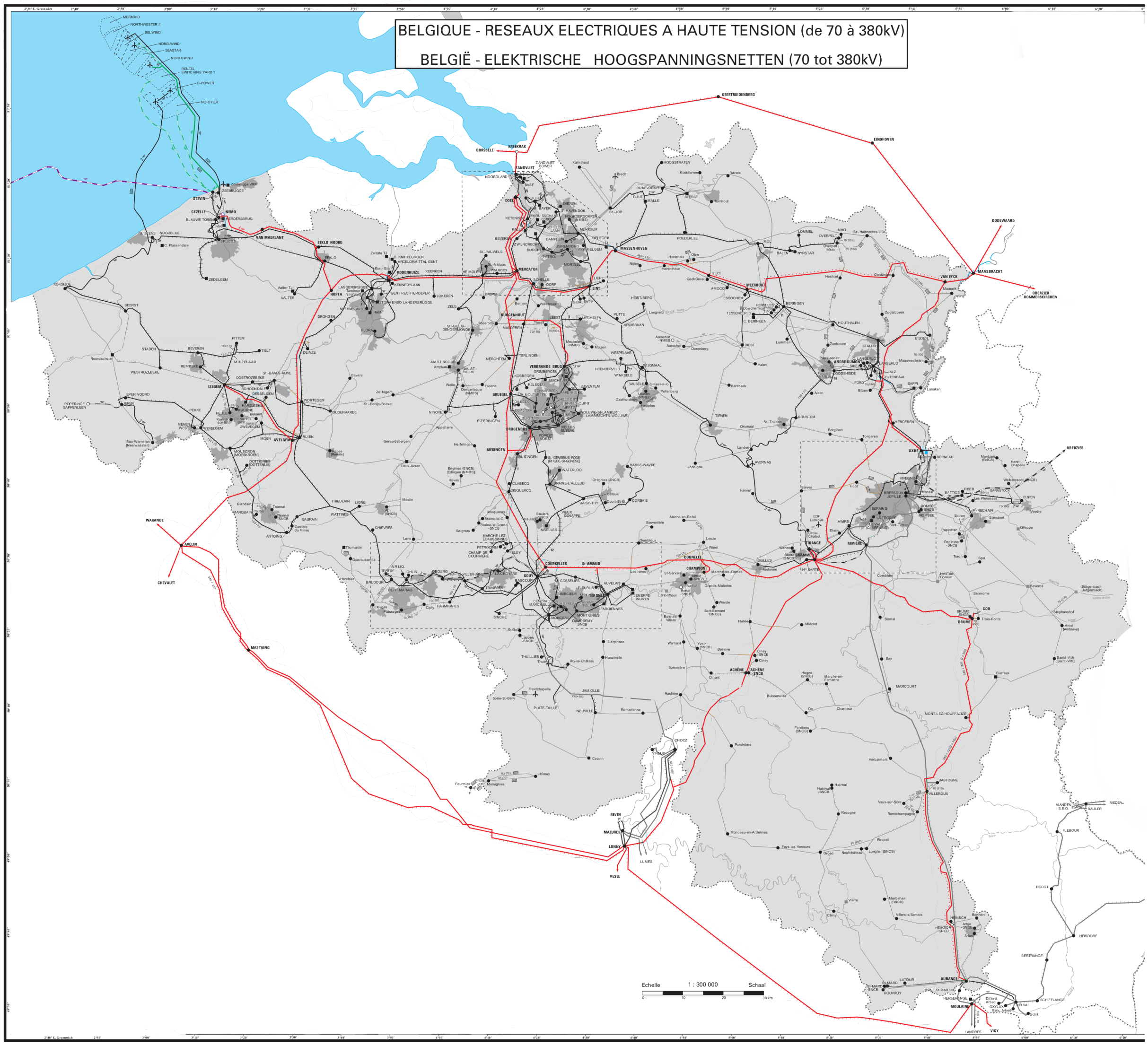

FIGURE 4.1: Map of Belgian High Voltage Grid [45]

Due to the voltage level restriction at 380 [kV], several simplifications have been made :

- Restriction in voltage buses : only buses at 380 [kV] have been represented. Downstream grid is simply represented by loads at several places. More details will be given in SECTION 4.4.
- Only the biggest electricity production sites with a nominal power over 350 [MW] have been taken into account.
- All synchronous generators are connected to BHVG through 150/380 [kV] transformers, except for the interconnection with the Netherlands and France, where the connection is made directly at 380 [kV], and for the Offshore Wind Farm which is connected through a 220/380 [kV] transformer.

Once these approximations are made, this results in a simplified network represented by the single-line diagram in FIGURE 4.2. This representation of the grid does not accurately describe the spatial arrangement of the different buses.

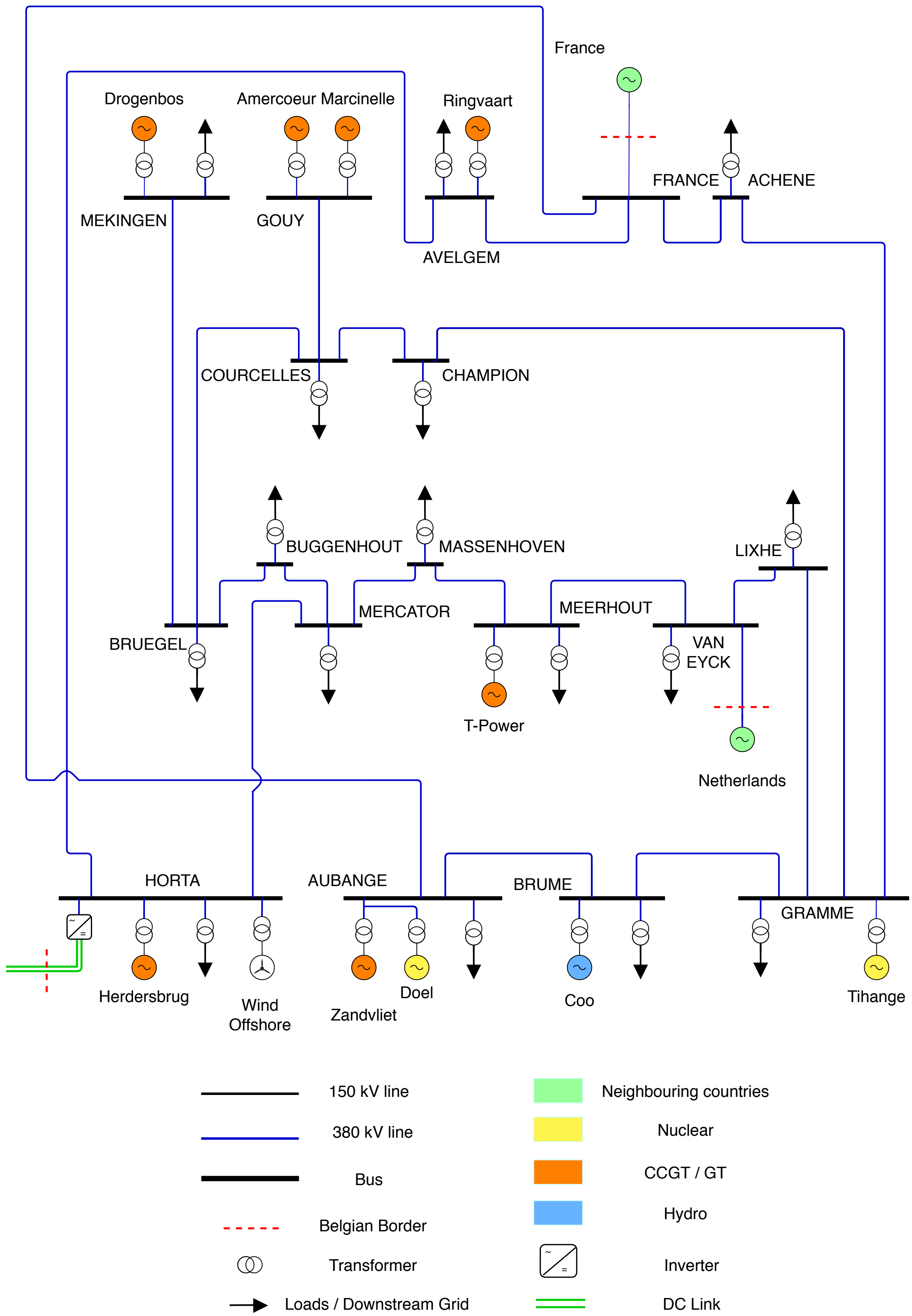

FIGURE 4.2: Single-line diagram of simplified BHV

4.2 Generation

4.2.1 Power generation in Belgium

This section details the modelling of the different production units connected to the high voltage grid. There are four main types of generation units connected to the High Voltage Grid in Belgium : nuclear and gas plants, wind farms and hydro-turbines. These power generation means have different control time constants and different inertia constants which leads to different dynamic behaviours.

The choice is made to only incorporate in the grid equivalent model the power plants with a nominal power of more than 350 [MW] . This choice is driven by the limited computational power available to run the simulations.

Generation units

TABLE 4.2 summarizes the Belgian power units incorporated in the equivalent model of the grid [46]. It can be seen that there are three main types of power plants: nuclear, gas and hydro-power. Additionally, offshore wind farms represent a significant amount of the Belgian electricity supply during times of powerful winds.

Production units in Belgium			
Location	**Type**	**Number of Power Units**	**Total Power [MW]**
Doel	Nuclear	4	2923
Tihange	Nuclear	4	3008
Marcinelle Energie	CCGT	1	413
Amercoeur 1	CCGT	1	451
Drogenbos	GT/ST	3	460
Herdersbrug	CCGT	1	465
T-Power Beringen	CCGT	1	422
Zandvliet	CCGT	1	387
Ringvaart	CCGT	1	385
COO	Hydro	2	1164
Offshore Wind	Wind	N/A	1798

TABLE 4.2: Production units in Belgium with over 350 [MW] of capacity [46]

Control and inertia time constants

As previously stated, the control and inertia time constants are different depending on the production type as summarized in TABLE 4.3.

Inertia and Control time constants		
Type	**Inertia constant H [s]**	**Control T_s [s]**
Wind	0	N/A
Nuclear	4	0.8
Gas	5.29	1
Coal	2.63	0.8
Hydro	2.4	1.5
Diesel	0.95	0.6
Biomass	1.92	N/A
Solar	0	N/A

TABLE 4.3: Inertia and control time constants for several production types [47][48]

The inertia constant is defined as the ratio between the kinetic energy of a synchronous machine rotor to the rating of the machine. We see that gas turbines provide proportionally the most inertia followed by nuclear, coal, hydro-power, biomass and diesel. Evidently, solar panels do not provide inertia since they do not have rotational masses and they are connected to the grid through a set of AC/DC converters. Their control is such that their power injection is independent from the grid frequency (MPPT). Permanent magnet wind turbines do not add inertia as they are connected through power converters to the grid. DFIG wind turbines stator is directly connected to the grid but the DFIG inertia is neglected as we consider they are controlled to have a constant power output.

Then, we see that wind, biomass and solar power plants have no droop control time constant because they do not participate in the droop control. This assumption is made as wind and solar units are controlled to operate at their Maximum Power Point (MPP) and thus can not engage in droop control. Biomass power plants are supposed to be smaller reactors where investing in a droop control algorithm is not justified from an economical standpoint. For the other types of generation, diesel has the fastest droop response followed by nuclear, coal and hydro-power.

Load flow

As a reminder, the load flow analyses the electrical power flows in a system where multiple loads and generators are interconnected. For the load flow computations, there are three operating modes possible of the synchronous machines: PV (constant active power and voltage), PQ (constant active and reactive power) and swing node (adapts its active and reactive power to balance the grid).

All synchronous machines in the system are designated as PV nodes except one which is the swing node. At the equilibrium, synchronous machines as PV nodes generate a constant power and have a constant bus voltage. On the other side, the synchronous machine at the swing node adapts its power production in order to balance the system. Because in real life priority will be given to the Belgian generation units, the choice was made to use one of the neighbouring countries as swing node to balance the Belgian generation and consumption.

More precisely, France is considered as swing node and thus the power flows through the interconnection of the Belgian grid with French grid will balance the system.

Nuclear

There are two nuclear power plants in Belgium : Doel and Tihange. These power plants have multiple reactors that have to be brought to one Thevenin equivalent model to reduce the computational power required to solve the system. The Thevenin equivalent model is constituted of one equivalent synchronous machine and one equivalent line to connect to the grid. The equivalent synchronous machine has a nominal power which is the sum of each reactor individual power. The inertia constant remains the same and the control time constant as well.
Then, the line equivalent impedance is found by calculating the value of the four lines in parallel. The impedance of the equivalent line is thus smaller than the value of each line.

Gas

The gas power plants have mainly only one reactor and thus one set of bus-bars. Therefore, the equivalent model for the gas power plants is simply a synchronous machine with the reactor nominal power in series with the line connecting the plant to the grid.

Hydro

All the hydro power capacity in Belgium is concentrated in the hydro station of Coo. This station has two reactors connected in parallel to the grid. The Thevenin equivalent of the two reactors is a synchronous machine with as nominal power the sum of the individual power of each reactor. Then, the line connecting the synchronous machine to the grid is obtained by taking the equivalent parallel impedance of the two individual lines.

Wind

Only the Offshore Wind Farms are represented in the grid equivalent model and they are all connected to BHVG through a single power line. There are 9 Belgian offshore platforms which are composed of Doubly-Fed Induction Generator (DFIG) and Permanent Magnet (PM) wind turbines [49], as summarized in FIGURE 4.3 and TABLE 4.4. Because we consider small time steps for the stability analysis, we assume that the wind speed does not vary on those small time intervals and thus that the mechanical power of the turbines is constant.

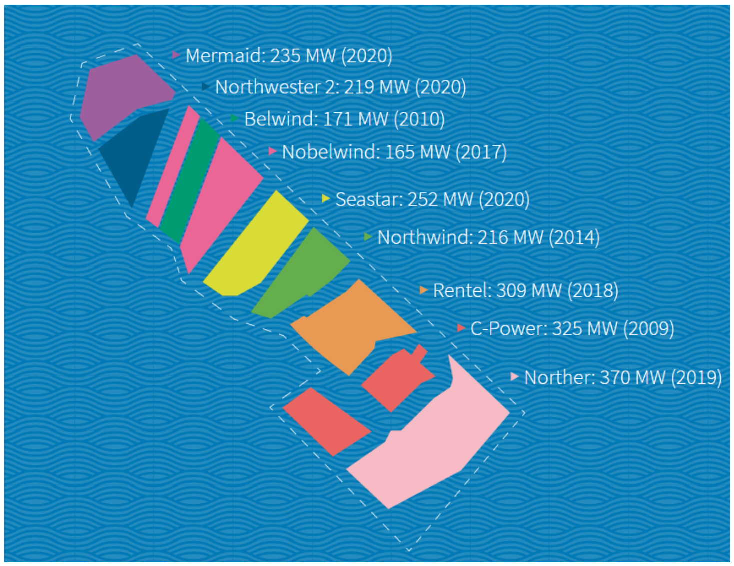

FIGURE 4.3: Map of Belgian offshore wind farm [49]

Belgian offshore wind farm				
Site	**Year**	**Nominal power [MW]**	**Type**	**Model**
C-Power	2009	325	DFIG	Senvion 5M-6M
Belwind	2010	171	DFIG	Vestas V90
Northwind	2014	216	DFIG	Vestas V112
Nobelwind	2017	165	DFIG	Vestas V112
Rentel	2018	309	PMSG	Siemens D7
Norther	2019	370	PMSG	Vestas V164
Northwester 2	2020	219	PMSG	Vestas V164

TABLE 4.4: Summary of the different production sites of Belgian Offshore Wind Farm [49]

First, let us consider the DFIG wind turbines. They generate an electrical power independent from the grid frequency because of the nature of their control system. Moreover, as the wind turbines are doubly-fed, the power converters are able to adapt the blades rotational speed to keep a constant power output even if the grid frequency changes. Therefore, as the mechanical power is considered constant and as the electrical generation is independent of the grid frequency, we can model the DFIG wind turbines as constant power generation units.

Then, the permanent magnet synchronous machines (PMSG) are also modelled as constant power injection units. PMSG are directly connected to the grid through power electronics and can therefore not take part take part in the grid inertia. As the mechanical power of the turbines is considered constant, they will produce a constant power output. More details are given in SECTION 4.2.5 concerning this hypothesis.

4.2.2 Neighbouring countries

The Belgian grid is directly connected to France with an interconnection capacity of 2000 [MW] and to the Netherlands with an interconnection capacity of 1200 [MW] [50]. The links with France are in the cities of Chooz, Mont St. Martin and Avalin. There are also two links with the Netherlands, in Kreekrak and Maasbracht.

France

The French grid is modelled as an equivalent synchronous machine with an appropriate inertia and an appropriate time constant. The inertia of the French grid is calculated with *Equation* 4.1

$$H_{tot} = \frac{\sum_{i=1}^{N} H_i S_{Bi}}{\sum_{i=1}^{N} S_{Bi}} \tag{4.1}$$

With :

- H_i the inertia constant of the individual machines
- S_{Bi} the nominal three-phase power of the individual machines
- H_{tot} the total inertia constant of the system

So the inertia constant of the equivalent synchronous machine that represents the French grid is the weighted average of the inertia constant of the different French generation units. The French electricity generation mix is summarized in TABLE 4.5.

French Electricity Mix and time constants				
Type	**Electricity Production [TWh]**	**Percentage %**	**H [s]**	**T_s [S]**
Nuclear	412.96	71.9	4	0.8
Wind	28.5	5.0	0	N/A
Coal	9.27	1.6	2.63	0.8
Gas	31.86	5.5	5.29	1
Hydro	70.14	12.2	2.4	1.5
Diesel	5.59	1.0	0.95	0.6
Solar	10.2	1.8	0	N/A
Biomass	5.88	1.0	1.92	N/A

TABLE 4.5: Summary of the electricity production mix in France in 2018 and of the time constants [51] [47]

As shown in TABLE 4.5, the electricity production in France is dominated by nuclear power and it has a significant amount of hydro-power as well. Using the data summarized in the table and *Equation* 4.1, we can calculate the total inertia constant of the French grid as follows :

$$H_{French} = \frac{\sum_{i=1}^{N} H_i E_i}{\sum_{i=1}^{N} E_i} = 3.53 \quad [s] \tag{4.2}$$

With:

- H_{French} : the total inertia constant of the french grid
- H_i : the inertia constant of each production type
- E_i : the electrical energy produced by each production type

Here, the weighted average for the inertia was done with electrical energy production instead of the three-phase nominal power. This choice is more logical as the generation units only contribute to the inertia when they are actively feeding electricity to the grid. This means that back-up units as diesel and gas power reactors may have a large capacity compared to their effective electricity production.

Therefore, using the electricity production of each unit instead of their three-phase nominal power gives a more accurate result as it takes into account the prioritisation of the different production types for the electricity production.

Then, the equivalent total time constant for the droop control is also calculated using a weighted average of the droop time constants of the several units participating in the droop control. *Equation* 4.3 gives the formula to calculate the total time constant.

$$T_{S,tot} = \frac{\sum_{i=1}^{N} T_{S,i} E_i}{\sum_{i=1}^{N} E_i} \tag{4.3}$$

With :

- $T_{S,total}$: the total time constant for the droop control of the system
- $T_{S,i}$: the droop control time constant of each production type
- E_i : the electrical energy produced by each production type

Using *Equation* 4.3 and the data provided in TABLE 4.5, we can calculate the french equivalent as follows:

$$T_{S,French} = \frac{\sum_{i=1}^{N} T_{S,i} E_i}{\sum_{i=1}^{N} E_i} = 0.832 \quad [s] \tag{4.4}$$

Finally, the three links between France and Belgium are modelled by three lines whose impedance are found in the Elia's database [46].

Netherlands

As the French grid, the Dutch grid was modelled as an equivalent synchronous machine with an appropriate inertia and an appropriate control time constant. The Dutch electricity generation mix is summarized in TABLE 4.6.

Dutch electricity mix and time constants				
Type	**Electricity Production [TWh]**	**Percentage %**	**H [s]**	**T_s [S]**
Nuclear	4	4.4	4	0.8
Wind	7	7.7	0	N/A
Coal	29	31.8	2.63	0.8
Gas	49	53.8	5.29	1
Hydro	0.1	0.11	2.4	1.5
Diesel	0	0	0.95	0.6
Solar	1.5	1.65	0	N/A
Bioenergies	0.5	0.55	1.92	N/A

TABLE 4.6: Summary of the electricity production mix in the Netherlands in 2015 and of the time constants [52] [47]

As shown in TABLE 4.6, the electricity in the Netherlands is primarily generated by coal and gas power plants. Nuclear and wind power make up most of the remaining 15% of electricity produced.

The total inertia constant of the equivalent synchronous machine that represents the Dutch is calculated using *Equation* 4.5 and the data in TABLE 4.6:

$$H_{Dutch} = \frac{\sum_{i=1}^{N} H_i E_i}{\sum_{i=1}^{N} E_i} = 3.87 \quad [s] \tag{4.5}$$

With:

- H_{Dutch} : the total inertia constant of the Dutch grid
- H_i : the inertia constant of each production type
- E_i : the electrical energy produced by each production type

Then, using *Equation* 4.3 and the data in TABLE 4.6, the total time constant for the droop control in the Netherlands is calculated as follows:

$$T_{S,Dutch} = \frac{\sum_{i=1}^{N} T_{S,i} E_i}{\sum_{i=1}^{N} E_i} = 0.829 \quad [s] \tag{4.6}$$

With :

- $T_{S,Dutch}$: the total time constant for the droop control of the Netherlands
- $T_{S,i}$: the droop control time constant of each production type
- E_i : the electrical energy produced by each production type

Finally, the links between the Netherlands and Belgium are modelled by two lines whose impedance is found in the Elia's database [46].

Summary We calculated that the inertia constant of the French and Dutch grid are respectively 3.53 and 3.87 seconds. The inertia constant of the dutch grid is higher as gas power plants produce more than half of the electricity in the Netherlands and gas turbines have the highest inertia constant. Then, the time constant for the droop control is approximately 0.83 seconds in both countries and thus they will have an equally fast droop response.

United Kingdom NemoLink is the interconnection with the United Kingdom and is quite different from those with Netherlands and France. Unlike the last two, where electricity is transmitted in AC, the DC link between Belgium and the United Kingdom is what is called a HVDC link, i.e **H**igh **V**oltage **D**irect **C**urrent. It is a sub-sea 140 km underground cable, able to transmit active power in both direction, from Herdersbrug in Belgium to Richborough in United Kingdom.

DC voltage is at 400 [kV] and the line capacity reaches 1000 [MW]. NemoLink is equipped with the recent **M**odular **M**ulti-level **C**onverter (MMC) technology of inverters. A simplified overview of the HVDC control is depicted in Figure 4.4 :

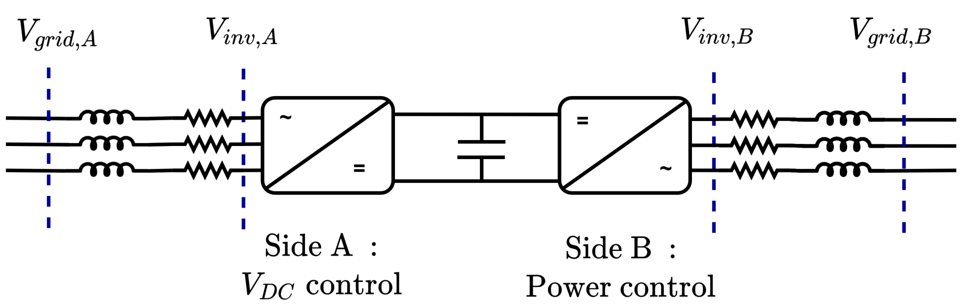

Figure 4.4: NemoLink simplified representation

The following reasoning remains valid if both sides are reversed. Each side of the link has a different function. One side is responsible for regulating the DC voltage of the HVDC link, arbitrarily the side A, and the other side, arbitrarily side B, is in charge of adjusting the power setpoint.

V_{DC} control : if the voltage on the capacitor between the converters is fluctuating, it means that the power is not well transmitted on the line. The role of the side A is to regulate the DC voltage through the i_d component of the current (i.e the one in phase with the grid voltage) in order to ensure the right power transmission.

P control: also through the control of i_d component of the current, the converter generates the power setpoint that the side B wants to receive or inject from/to NEMOLINK.

An advantage of this kind of converters is that the voltage control of the grid side is fully decoupled from the HVDC control. Indeed, as previously said, i_d component is used for V_{DC}/Power regulation, while the i_q component of the current regulates the voltage of the grid-side for A & B.

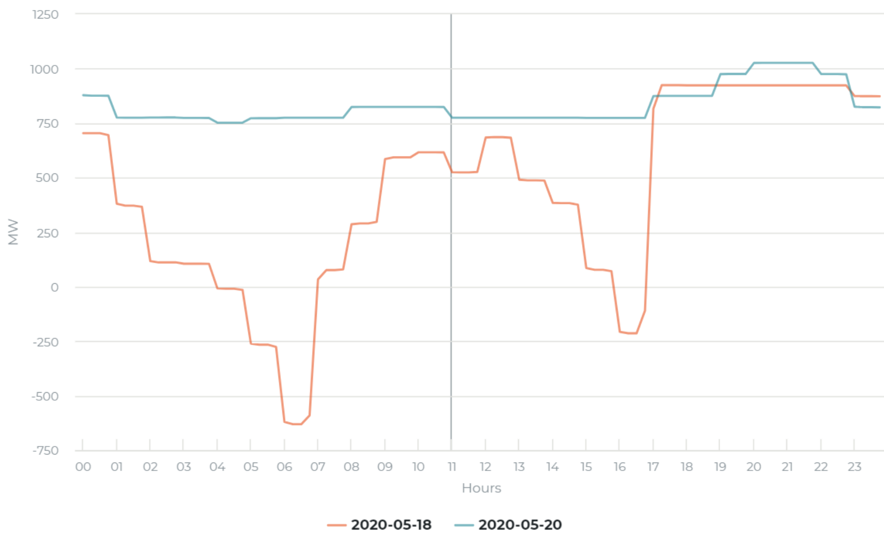

FIGURE 4.5: Power profile of NEMOLINK during two days of May 2020 [50]

The hourly power profile of NEMOLINK is shown in FIGURE 4.5. Two days are represented on the graph, one on each curve, to highlight the fact the profile is highly variable from day to day. Also, the power setpoint can only change every quarter of an hour. At the timescale of the inertial and droop effect that the thesis aims to analyze, NEMOLINK can be seen as a constant power injection. Moreover, in the way it is currently controlled, this HVDC can not provide any inertia to the grid. Therefore, the same model as the one used for Wind Farm will be used for NEMOLINK.

4.2.3 Synchronous Machine

Synchronous machines are used in the grid equivalent model to simulate various types of power generation. They also play an important role in the grid frequency stability as they provide inertia thanks to their rotating masses. The following paragraphs analyze the dynamics of the synchronous machine model that was used.

Simplified synchronous machine model

A simplified model of the synchronous machine is adopted in order to limit the computational time. Moreover, it is not necessary to have the whole detailed set of equation for the frequency analysis. This simplified model is provided by SIMULINK and is available on Simscape Library.

Equations Here are the main equations describing the model [53]. The electrical angular frequency deviation is computed as follows :

$$\Delta\omega(t) = \frac{1}{2H}\int_0^t (T_m - T_e) - K_d \Delta\omega(t) dt \tag{4.7}$$

Where H is the inertia constant of the synchronous generator, T_m and T_e the mechanical and electromagnetic torques, K_d the damping coefficient emulating simplified damper windings. The latter can be expressed as :

$$K_d = 4\xi\sqrt{\frac{\omega_s H P_{max}}{2}} \tag{4.8}$$

Where ω_s is the electrical angular frequency of the machine in $[rad/s]$. ξ is the damping ratio of the second-order transfer function modelling the variation of machine power angle δ resulting from a change of mechanical power P_m :

$$\frac{\delta}{P_m} = \frac{\omega_s/(2H)}{s^2 + 2\xi\omega_n s + \omega_n^2} \tag{4.9}$$

This approximated transfer function is valid when the machine is connected to an infinite grid (zero impedance). Since the modelled High Voltage Grid includes more than 10 generators, the grid Thevenin equivalent can be seen as infinite from a single generator point of view. Then, we can assume small power angles δ such that $\sin(\delta) \simeq \delta$.

Maximum power P_{max} found in *Equation* 4.8 can be found with the following equation, representing the *maximum power in pu transmitted through reactance X at terminal voltage V_t and internal voltage E* [53]

$$P_e = \frac{V_t E \sin(\delta)}{X} \tag{4.10}$$

Finally, when there is a change of mechanical power, load angle δ also varies, and undergoes a serie of oscillations before stabilizing to a new steady-state value. The frequency of these oscillations is given by :

$$f_n = \frac{1}{2\pi}\sqrt{\frac{\omega_s P_{max}}{2H}} \tag{4.11}$$

Electrical equations are also simplified : the electrical circuit is basically a voltage source in serie with a transient reactance and a resistance (in per unit, resistance and reactance are set by default at $R = 0.02$ and $X = 0.3$) . All the other elements (armature magnetizing inductances, field an damper windings) are neglected. The three voltage sources and R-L impedance branches are Y-connected.

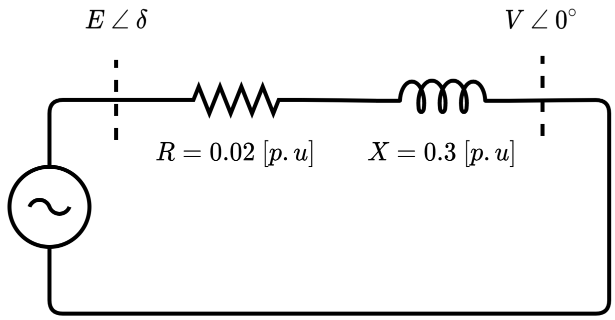

FIGURE 4.6: Simplified electrical circuit of synchronous machine

The damper windings effect, as previously said, is simplified by damping factor K_d. For this one, a choice has to be made as this coefficient has two effects :

- It damps the oscillations
- It reduces the frequency deviations during a power imbalance

FIGURE 4.7 helps to find an acceptable range for K_d values. This graph describes the dynamic behaviour of the grid frequency on a two-node systems, where a new load is successively connected in Area 1, then Area 2, and then successively disconnected. Both areas only have :

- A synchronous generator
- A simplified governor model as described in the next paragraph
- A 25 kV/ 230 kV transformer
- A load (only active power)

The power tie line between areas is modelled as a simple reactance. TABLE 4.7 summarizes the different quantities :

2-nodes system values					
	P_{nom} [MW]	$V_{nom,SM}$ [kV]	$V_{nom,loads}$ [kV]	P_{load} [MW]	ΔP_{load} [MW]
Area 1	300	25	230	100	50
Area 2	100	25	230	80	40

TABLE 4.7: Two-nodes system features

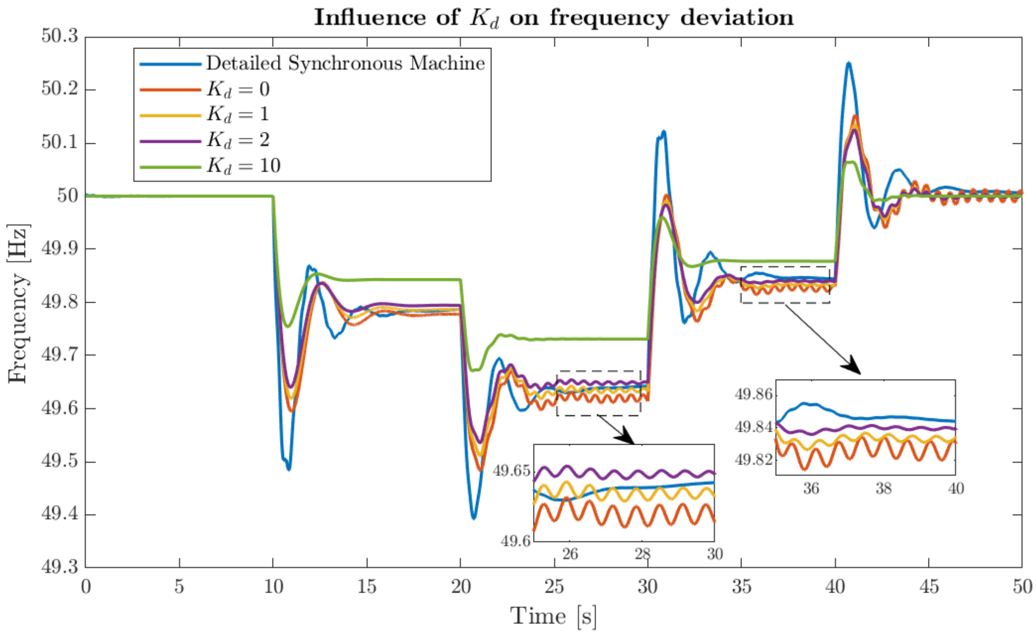

FIGURE 4.7: Comparison between detailed model of SM and simplified model with several K_d on the simplified two nodes network

Several observations can be made : first, for all K_d values, both frequency nadir and frequency overshoot are underestimated compared to the values of detailed SM, even when no damper windings are emulated (i.e $K_d = 0$). It has a consequence for the analysis of future results : the tolerances concerning acceptable frequency deviation must be tighter for our simulations than for real situation.
A compromise has to be made between two aspects : suppress the oscillations due to simplified transfer function $\dfrac{\delta(s)}{P_m(s)}$, and be as close as possible to the actual values of the frequency when a new equilibrium is established.
Both $K_d = 1$ and $K_d = 2$ are a good compromise between these two aspects. For $K_d = 10$, steady-state value is too far from detailed model of SM. $K_d = 0$ involves too big oscillations while $K_d = 1$ and $K_d = 2$ have a satisfying damping. Depending on the equilibrium, each of these two values has the closest steady-state values to detailed model. A compromise is to take a mean value, which means $K_d = 1.5$

Governor model

A droop control was added to the simplified model of the synchronous machine in order to bring back the frequency to an equilibrium state after a disturbance. This is a simplified implementation of primary frequency control, discussed in SECTION 1.6. The primary control generates the mechanical power input of the synchronous machine block as follows [65]:

- The total mechanical power setpoint of the synchronous machine, $P_m^{set,tot}$, is made of two parts : the reference mechanical power of the turbine $P_{m,0}^{set}$, and the mechanical power injected or absorbed when there is a frequency deviation, proportional to the droop S :

$$P_m^{set,tot} = P_{m,0}^{set} + \Delta P_m^{set} = P_{m,0}^{set} - \frac{1}{S}\Delta f \tag{4.12}$$

If we consider the linearization around an equilibrium value for the whole system (i.e $P_{m,0}^{set} \simeq \Delta P_{m,0}^{set}$), and based on FIGURE 4.8, real mechanical power input of SM is expressed as :

$$\Delta P_m(s) = \frac{G_t(s)}{G_t(s) + \frac{1}{K_t}s}\left[\Delta P_{m,0}^{set}(s) + \Delta P_m^{set}(s)\right] \tag{4.13}$$

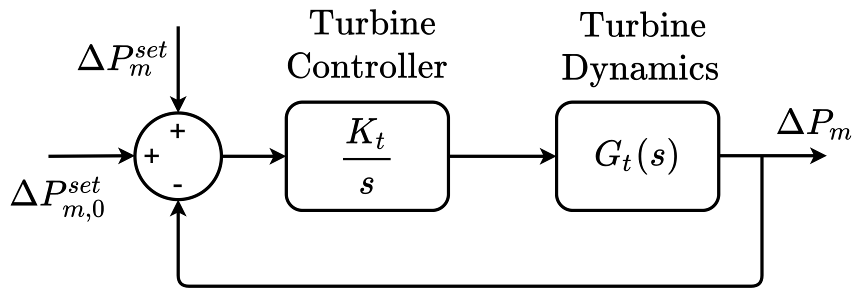

FIGURE 4.8: Dynamical behaviour of a turbine [65]

Neglecting turbine dynamics (i.e considering turbine response instantaneous : $G_t(s) \simeq 1$) and considering constant reference mechanical power ($\Delta P_{m,0}^{set} = 0$)

$$\frac{\Delta P_m(s)}{\Delta P_m^{set}(s)} = \frac{1}{1 + T_t s}, \qquad T_t = \frac{1}{K_t} \tag{4.14}$$

The transfer function between setpoint and real mechanical power input in *Equation* 4.14 is a first-order transfer function, describing a simple delay due to the turbine controller.

Adding the droop term in order to get the transfer function between the real mechanical power input and the frequency deviation, the complete simplified model of governor is obtained :

$$\frac{\Delta P_m(s)}{\Delta f} = \frac{-1/S}{1 + T_t s}, \tag{4.15}$$

4.2.4 Voltage regulation

In this thesis, the voltage is assumed no to have a significant impact on the grid frequency dynamics. Therefore, no voltage regulation systems nor SM exciter are considered in the BHVG modelling.

4.2.5 Wind Farm Model

As mentioned in Section 4.2.1, Offshore Belgian Wind Farm mainly consists in two types of turbines : **D**oubly **F**ed **I**nduction **G**enerator (**DFIG**) and **P**ermanent **M**agnet **S**ynchronous **G**enerator (**PMSG**). Both belong to the variable speed turbines family, which is opposed to fixed-speed turbines. Variable speed turbines offer several advantages [54]: better yield in energy, lower mechanical stress, noise reduction, lower output power variation and complete control of both active and reactive power. However, each variable-speed technology has its pros and cons ([55], [56], [57]), summarized in Table 4.8.

DFIG	
Pros	**Cons**
• Back-to-back converter sizing about 30% of DFIG rated power : smaller and cheaper • Speed range ± 30 %	• Gearbox needed • Slip rings needed • High initial and maintenance cost • Lower power factor at light loads • More sensititive to grid perturbations (stator directly connected to the grid)

PMSG	
Pros	**Cons**
• No need for excitation system and gearbox • Brushless (low maintenance) • Full-speed range • High power density and reliability	• Need of permanent magnets (high cost and possible demagnetization) • Full scale back-to-back converter • Multi-pole generator (big and heavy)

Table 4.8: Advantages and disadvantages of PMSG and DFIG wind turbines [55] [56], [57]

In order to spare computational time, a simplification of the wind farm has been made. In this process, the main question is whether wind turbines could provide inertia to the grid once connected to it. In other words, does a disturbance in the grid frequency affect the power injection of the wind turbines?

Part of the answer may lie in the wind turbine control topology, shown in Figure 4.9. On the right hand side, PMSGs are not directly connected to the grid. In between are an AC/DC converter followed by a DC/AC converter. This makes the PMSGs independent from the grid. No natural inertia can be extracted from this type of wind turbine. For the DFIGs, the situation is different, as they are partially connected to the grid through the stator. The rotor is connected to it via AC/DC and DC/AC converters. It is therefore legitimate to ask whether having the stator directly connected to the grid provides inertia.

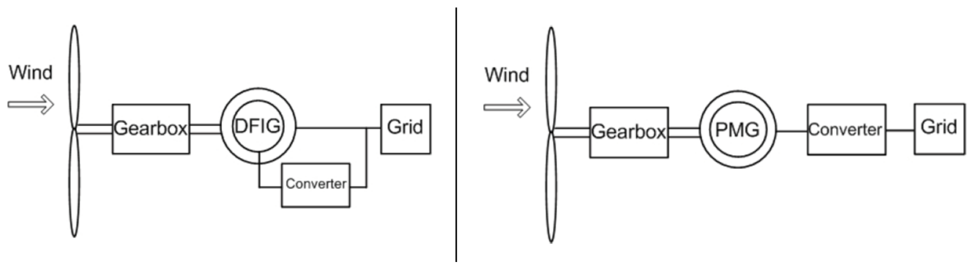

FIGURE 4.9: DFIG and PMSG simplified schemes [58]

Note : a gearbox is not necessarily present for PMSG. Indeed, due to its large number of pair of poles, its rotational speed can be sufficiently low to avoid a gearbox.

Maximum Power Point Tracking (MPPT) One of the main assumptions made for the Wind Farm model is that the wind turbines are operated via MPPT. As a reminder, FIGURE 4.10 shows power coefficient and power curves of wind turbines for several wind speeds. For both, the maximum point of the curve is different for each wind speed. Therefore the goal of the MPPT is track the optimal rotational speed ω_r of the rotor in order to maintain the maximum power output for all wind conditions, by adapting the rotational speed of the rotor [59].
The real power captured by a wind turbine can be expressed as [59] :

$$P = \frac{1}{2} C_p(\lambda, \beta) \rho A v_w^3 \tag{4.16}$$

With ρ the air density, A the area swept by the blades, v_w the wind speed and C_p the power coefficient of the turbine. This one is a non linear function of β, the pitch angle of the blades and $\lambda = \dfrac{\omega R}{v_w}$ the tip-speed ratio, which is the ratio between rotor linear speed and wind speed.

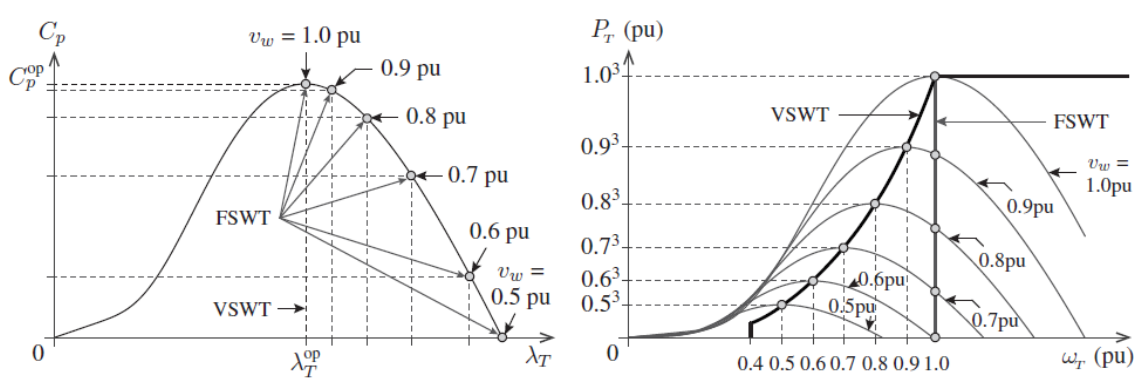

(a) C_p versus λ_T curve (b) P_T versus ω_T curve

FIGURE 4.10: Characteristic of power coefficient and output power for several wind speeds [60]

*Note : FSWT refers to **F**ixed **S**peed **W**ind **T**urbines and VSWT refers to **V**ariable **S**peed **W**ind **T**urbines.*

The three most common MPPT techniques are [59]:

- **P**erturbation & **O**bservation (P & O) : the rotor speed is slightly perturbed, and based on the output power observation, the next perturbation is adapted consequently.
- **W**ind **S**peed **Measurement** (WSM) : both wind speed and rotor speed are measured to find the optimum tip-speed ratio λ. In practice, wind speed is difficult to measure.
- **P**ower **S**ignal **F**eedback (PSF) : adapt the control algorithm to follow the maximum power curve by measuring the output power.

DFIG In order to determine if the DFIG can provide inertia to the grid, it seems important to look at its control algorithm. The latter is based on the electrical equations of the asynchronous machine, in the synchronous reference rotating dq frame [61] :

$$\begin{cases} v_{sd} = R_s i_{sd} + \dfrac{d\Phi_{sd}}{dt} - \omega_s \Phi_{sq} \\ \\ v_{sq} = R_s i_{sq} + \dfrac{d\Phi_{sq}}{dt} + \omega_s \Phi_{sd} \end{cases} \tag{4.17}$$

$$\begin{cases} \Phi_{sd} = L_s i_{sd} + M i_{rd} \\ \Phi_{sq} = L_s i_{sq} + M i_{rq} \end{cases} \tag{4.18}$$

$$\begin{cases} v_{rd} = R_r i_{rd} + \dfrac{d\Phi_{rd}}{dt} - \omega_r \Phi_{rq} \\ \\ v_{rq} = R_r i_{rq} + \dfrac{d\Phi_{rq}}{dt} + \omega_r \Phi_{rd} \end{cases} \tag{4.19}$$

$$\begin{cases} \Phi_{rd} = M i_{rd} + L_r i_{rd} \\ \Phi_{rq} = M i_{rq} + L_r i_{rq} \end{cases} \tag{4.20}$$

The vector control for DFIG is working in this synchronous reference frame such that [61]:

$$\boxed{\Phi_{sq} = \frac{d\Phi_{sq}}{dt} = 0} \tag{4.21}$$

$$\begin{cases} v_{sd} = R_s i_{sd} \\ v_{sq} = R_s i_{sq} + \omega_s \Phi_{sd} \end{cases} \tag{4.22}$$

$$\boxed{\Phi_{sd} = \Phi_s = \text{constant}} \tag{4.23}$$

$$\begin{cases} \Phi_{sd} = L_s i_{sd} + M i_{rd} \\ 0 \;\; = L_s i_{sq} + M i_{rq} \end{cases} \tag{4.24}$$

The torque of the turbine is controllable through rotor current i_{rq} [62]:

$$T_{em} = \Phi_{sd} i_{sq} - \Phi_{sq} i_{sd} = \Phi_{sd} i_{sq} = -\Phi_{sd} \frac{M}{L_s} i_{rq} \tag{4.25}$$

This part of the control lies in the left-hand side of FIGURE 4.11, in the rotor-side converter. The MPPT algorithm gives as output the optimal rotor rotational speed to extract the maximum power from the wind, and thus the resistive torque of the generator T_{em}.

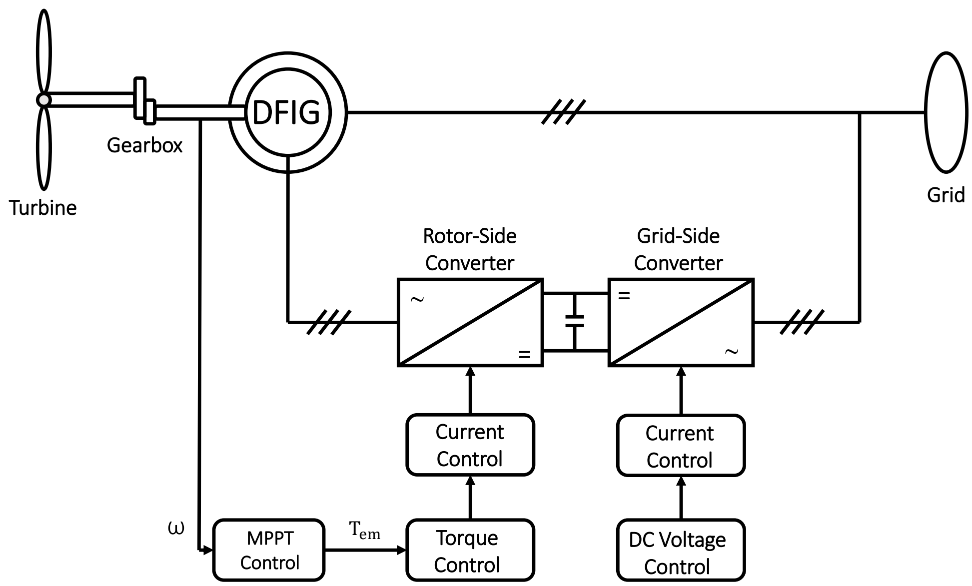

FIGURE 4.11: Simplified scheme of DFIG

If electrical losses and time rate of change of stored energy in inductances are neglected, power from rotor is proportional to the slip s and is given by [62]:

$$P_r = -P_s s = -P_s \left(1 - \frac{\omega_r}{\omega_{syn}}\right) \tag{4.26}$$

The total power from DFIG to the grid is the sum of the stator and rotor powers :

$$P_{tot} = P_s + P_r = P_s \frac{\omega_r}{\omega_{syn}} = (1 - s)P_s \tag{4.27}$$

P_{tot} can also be expressed as a function of electromecanical torque of the machine :

$$T_{em} = \frac{P_s}{\omega_{syn}} \Leftrightarrow P_t = T_{em}\omega_r \tag{4.28}$$

If we assume that the wind speed is constant and that the DFIG is regulated through T_{em}, what are the consequences of a change in the grid frequency?

1. The wind speed is constant : as seen previously, there is only one optimal rotor rotational speed w_r for a certain wind speed. The T_{em} setpoint associated to this $\omega_{r,opt}$ from MPPT remains then the same. Since $P_{tot} = T_{em}\omega_r$, total power of turbine remains constant.
2. A frequency deviation implies a change in ω_{syn}. Since T_{em} is constant, from *Equation* 4.28, a change in ω_{syn} results in a change of P_s, the stator electrical power.
3. Due to slip, and since $P_{tot} = P_s + P_r$, P_r also changes due to constant total power.

FIGURE 4.12 confirms what has just been explained. Indeed, an islanded electrical network with a 8 [MVA] Diesel Generator and a Wind Farm of 1.5 [GW] was modelled in [62]. The curves in FIGURE 4.12 show the behaviour of DFIG quantities when there is a load increase.

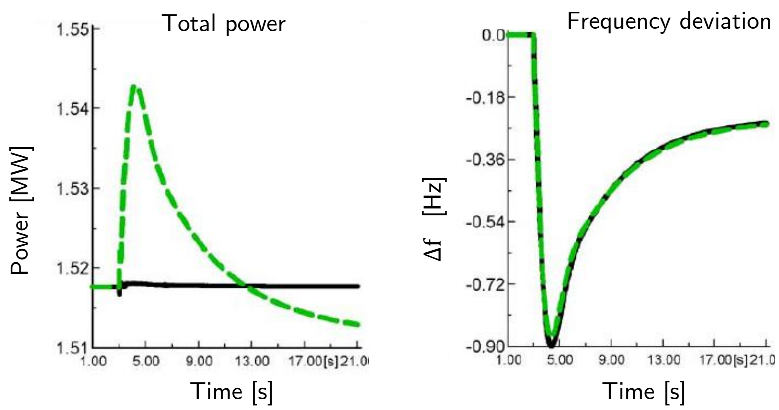

FIGURE 4.12: Simulation of DFIG behaviour for P_s control and for T_{em} control [62]

Two conclusions can be drawn from this figure :

- **Power injection point-of view** : with constant wind speed and MPPT through T_{em} control assumptions, the total power injected by DFIG to the grid remains constant when there is a deviation of grid frequency.
- **Influence of control on frequency behaviour** : regardless of the control mode (T_{em} or P_s), the frequency response of the grid remains the same.

From these first conclusions, we can assume that under constant speed assumption, DFIG wind turbines can be modelled as a constant power source.
Moreover, for the inertial aspect, an answer is also given in [62]. Indeed, if the number of connected DFIG increases while keeping the available inertia from the synchronous generator, the inertial response (thus the RoCoF) does not change. Other similar simulations have been carried out with the same result : DFIG are inertia-less, i.e do not contribute to the inertial response of the grid. They conclude by saying that due its back-to-back converter, rotor speed is decoupled from the grid speed, thanks to the very fast regulation (around 10 [ms]) of the electrical torque T_{em} [62].

In order to model wind turbines as constant power injection, the same algorithm is used than the one for VSG described in SECTION 3.3, with a constant power setpoint.

4.3 Overhead power lines

In order to model the overhead lines of the 380 [kV] Belgian grid, several assumptions are made :

Neglected line resistance : this simplification implies that resistive losses are neglected in the total power balance of the grid. Moreover, voltage drops across resistive elements are also neglected. Besides this, the total electrical losses in Elia grid (including 380/220/150 [kV] voltage levels) only represent around 1.5 % of the total power flowing in the whole Elia Grid [63]. Finally, resistances on High Voltage Grid have much smaller values than the reactances, as shown in the right-hand side of FIGURE 4.13 : on average, resistance value is ten times smaller than the reactance.

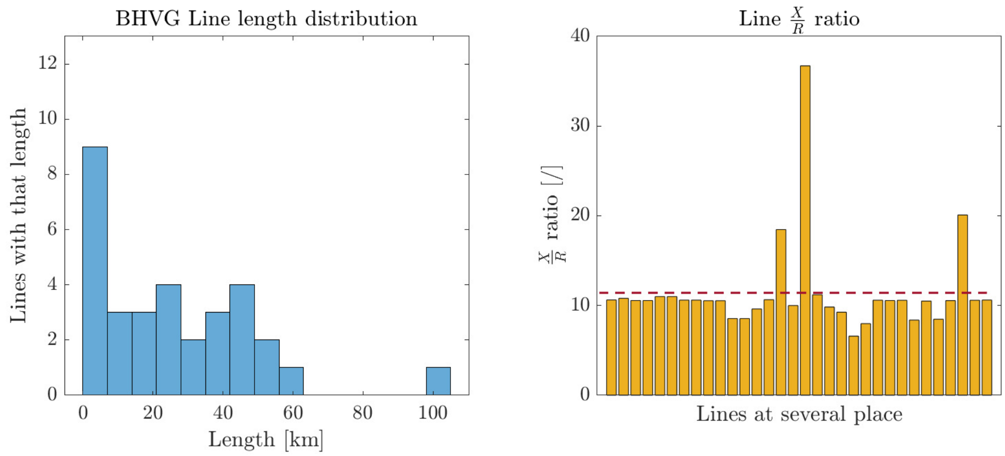

FIGURE 4.13: Line features [46]

Neglected capacitive effects : one of the main capacitive effect of the line is the Ferranti effect. It implies an overvoltage of the line if it is weakly loaded, or with no load at its end, which is not the case for our modeling of the grid. Furthermore, this effect happens for very long lines ($>$ 200 km), not present in BHVG. For overhead lines, capacitive effects are generally much lower than inductive effects. They become important when electricity is transmitted through underground cable [64], which is only the case for the connection with the offshore platform.

Very-short length lines : according to [64], for overhead lines whose length is smaller than 100 [km], the very-short length line approximation can be done : the line impedance can be modelled as only its series impedance (i.e inductance and resistance in series). By looking at the left-hand side of FIGURE 4.13, most of the lines are smaller than 60 [km], except for one line of 100 [km]. This approximation is thus consistent.

4.4 Loads and downstream grid

In order to model the downstream grid in a simplified way, we decided to represent it as loads connected at the BHVG different buses. In other words, distribution grid is seen here from the high voltage level as a load consuming a given amount of power.

However, the distribution grid contains different types of rotational loads and also has dispersed generation injecting power from downstream to upstream due to renewable energy sources. The result is that power consumption in the distribution grid is variable and frequency dependent. Therefore, the distribution grid cannot be modelled as a set of constant loads as it needs to adapt its consumption if the grid frequency changes.

The distribution grid is thus modelled as a set of static voltage and frequency dependent load.

This model is characterized by *Equation* 4.29 [65].

$$P_{load} = P_0 + \left(1 + K_{pf}\frac{f - f_0}{f_0}\right)\left(\frac{V}{V_0}\right)^{\alpha} \tag{4.29}$$

With :

- P_{load} : the effective consumption of the load
- P_0 : nominal power consumption of the load
- K_{pf}: load frequency dependency factor
- α : load voltage dependency factor
- f : the frequency of the grid
- f_0 : the nominal frequency of the grid (50Hz)
- V_0 : the nominal voltage of the grid

The value of α determines the type of load :

- $\alpha = 0$ represents a constant power load
- $\alpha = 1$ represents a constant current load
- $\alpha = 2$ represents a constant impedance load

The value of coefficient K_{pf} also depends on the type of load. According to [69], distribution grids have a K_{pf} that varies between 0 and 3. This results is also confirmed by Table 4.9 [65]. This table gives typical values of these parameters for several load categories :

Load coefficients			
Load category	cos(ϕ)	α	K_{pf}
Residential, summer	0.9	1.2	0.8
Residential, winter	0.99	1.5	1
Commercial, summer	0.85	1	1.2
Commercial, winter	0.9	1.3	1.5
Industrial	0.85	0.2	2.6
Power plant auxiliaries	0.8	0.1	2.9

Table 4.9: Load cos(ϕ) and α coefficient

From this table, some conclusions concerning modelling choices can be drawn :

- **Purely active power loads :** when looking at cos(ϕ), most of the values are close to 1. It means that the loads are way more active than reactive, i.e that they can be represented by a resistive load rather than a capacitive or inductive one. But the main argument that allows to model the load by a resistive load (i.e Q = 0) is that the frequency dynamics are influenced by the imbalance in **active** power (cfr the swing equation), thus reactive power has no influence on that issue.

- **Frequency dependent loads:** as seen in *Equation* 4.29, variable loads consume less power in under-frequency states in the grid and more power in over-frequency states. Therefore, variable loads are theoretically mitigating the frequency deviations in the grid as they counteract the power imbalance.

- α **values:** when looking at the α values, residential and commercial loads are closer to $\alpha = 1$ and thus can be modelled as constant current loads, while industrial loads are closer to $\alpha = 0$, i.e constant power loads. The reality should lie between these two load representations. Unfortunately, the default SIMULINK model for three-phase loads considers a constant impedance load, i.e $\alpha = 2$.

In the next chapter, SECTION 5.3 focuses on the type of load influence. Two types of loads will be considered : constant power loads with a frequency dependency (i.e $\alpha = 0$, $K_{pf} \neq 0$), and constant impedance load without frequency dependency (SIMULINK default model, $\alpha = 2$, $K_{pf} = 0$). The goal is to determine if the value of α and K_{pf} have a significant impact on frequency dynamics.

Chapter 5

Simulation results

In this section, the SIMULINK simulation results are analyzed in order to determine the impact of the VSG on the RoCoF reduction, the frequency nadir and the final frequency deviation after the primary control.

First, the different frequency response timescales are studied and the first differences between theoretical expectations and the simulation results are noticed.
In a second step, a parametric analysis is achieved to observe the impact of the two main parameters of the VSG (i.e droop coefficient D and inertia constant H) on the grid frequency dynamics. This first analysis allows to determine a convenient range of values for these parameters.

Thereafter, some realistic scenarios are studied. It covers :

- A sudden generator loss
- A sudden load increase
- A progressive increase of RES penetration rate in anticipation of the nuclear closure at the 2025 horizon.

For each scenario, the addition of the VSG is analyzed to observe its impact on the quantities previously mentioned.

An important remark concerning the following results is that the RoCoF measure is not standardized and its value depends strongly on how it is measured. As explained in the next section, a numerical instantaneous $\frac{df}{dt}$ is not necessarily relevant to quantify the RoCoF. In this thesis, the RoCoF has been measured on a larger time window of a few dozen milliseconds, based on a linear approximation, i.e $\frac{df}{dt} \simeq \frac{\Delta f}{\Delta t}$. However, the duration of the time window Δt influences strongly the RoCoF value (more than 50% difference between measurements) [66]. Still, the goal of this thesis is to analyze the tendencies rather than precise values. By keeping the same measurement method through the whole chapter, consistent comparisons can be made.

Finally, the three main metrics that are studied in this chapter are the RoCoF, the frequency nadir Δf_{nadir} and the final equilibrium frequency Δf_{eq}. As a reminder, f_{nadir} is the minimum frequency point during an imbalance, while f_{eq} is the final frequency value reached after the primary control action. The Δ symbol refers to their deviation from the nominal frequency, i.e 50 [Hz].

5.1 Primary control and time scales

This sections aims to show the impact of primary control on grid frequency dynamics. As a reminder, the droop control changes the machines setpoint when there is a frequency deviation such that :

$$P_m^{set,tot} = P_{m,0}^{set} + \Delta P_m^{set} = P_{m,0}^{set} - \frac{1}{S}\Delta f \tag{5.1}$$

Therefore, the lower the droop *S*, the greater the injected power from the machines when there is an imbalance, and thus the lower the frequency deviation. This first result is seen in Figure 5.1. Concerning the initial RoCoF, the droop of the machines does not influence it. It is the same for all situations, i.e for several droops and without droop control. This seems logical since the droop control timescale is much different from the inertial response timescale : a few milliseconds vs. several seconds. Droop control has not yet taken part in the frequency regulation in the first instants after the disturbance. The droop value have been chosen in the range $[2\% \ - \ 12\%]$ imposed by European Union law [67].

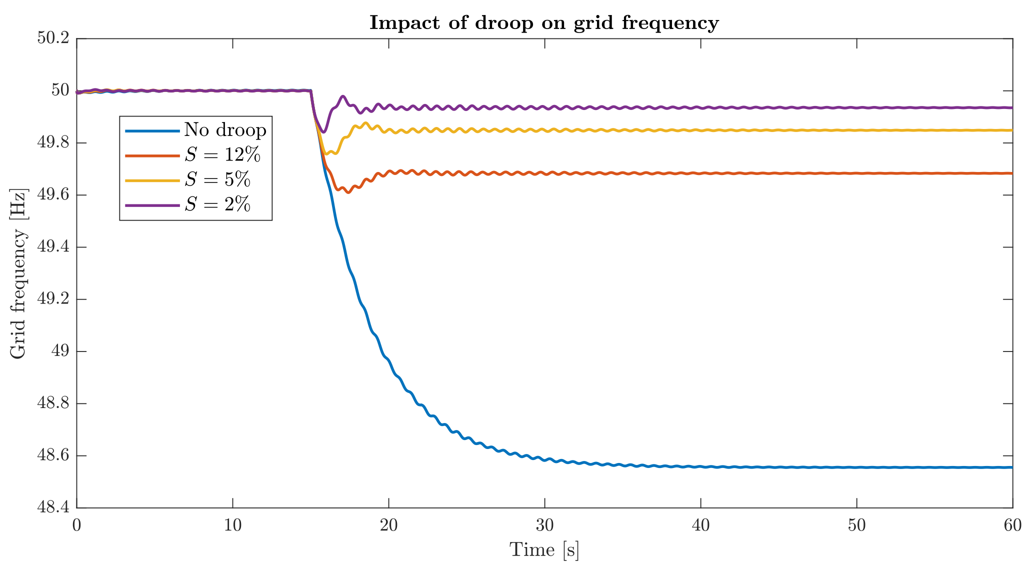

Figure 5.1: Grid frequency dynamics of BHVG with various droops

Another observation that can be made is that the time to reach the frequency nadir is different depending on the droop value. This seems normal because for the same initial RoCoF, if the final deviation is lower, the time to reach it is also lower.

The difference in timescales discussed before is clearly observable in Figure 5.2. This graph was obtained in a one-node system (i.e one generator and one load) in order to easily observe the dynamics. The graph depicts the electrical power behaviour of a synchronous machine during the connection of a new load in the system.

- The red curve is the natural/inertial response of the SM, without any droop control.
- The yellow curve is the mechanical power setpoint of the machine P_m generated by droop control.
- The blue curve is the droop response of the SM.

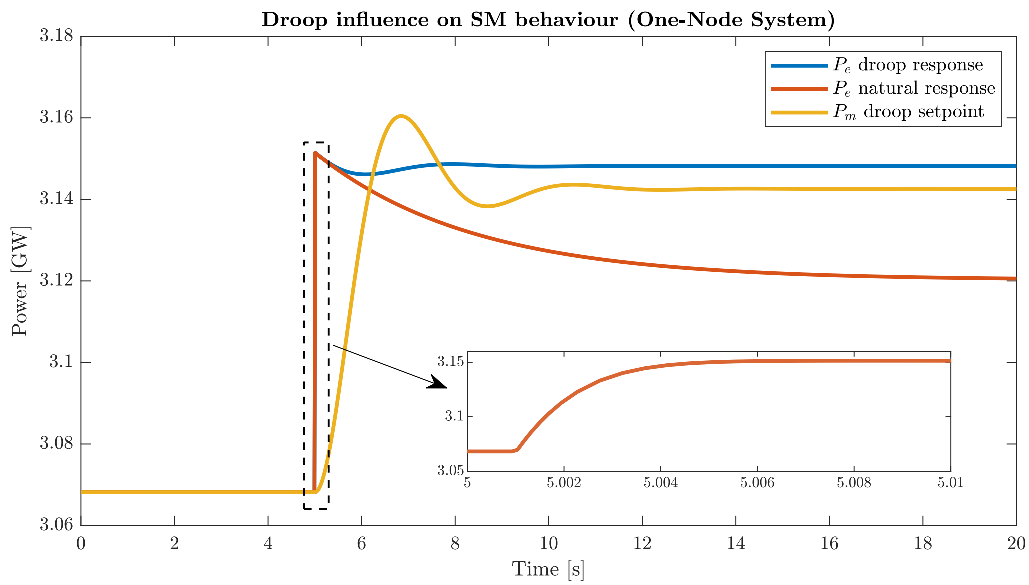

FIGURE 5.2: Power injected by a synchronous generator after an imbalance in t = 5 [s]

As said before, FIGURE 5.2 allows to observe accurately the various timescales. First, the inertial response of the machine reaches its peak value in nearly 6 [ms]. If there is no primary control, the electrical power will then decrease to a steady-state value, corresponding to the new frequency equilibrium.

The droop control allows the SM to maintain its power at a certain value, instead of letting it decay as in the natural response. The timescale for droop control is in seconds : it takes 1.85 [s] to reach the peak value, and more than 7 [s] to reach the steady-state value. There is an order of magnitude of 1000 between the inertial and the droop response timescales of the machine. This confirms what was said before : droop-control has no influence on the behaviour of SM during the first milliseconds after a perturbation, and thus does not influence the initial RoCoF.

This results is confirmed when looking at the power behaviour of Tihange power plant on the SIMULINK BHVG grid in FIGURE 5.3. The tendencies remain the same, with much more oscillations. This is the result of interactions between machines, since the BHVG is a multi-machine system. Indeed, when there is an imbalance, the power angle of each machine changes and oscillates before reaching a new state value. The relative variation of power angles between all the machines results in larger oscillations than in a one-node system. It is also useful to keep in mind that the dynamic behaviour of SM is simplified by a 2^{nd} order transfer function.

TABLE 5.1 summarizes the two scenarios studied for FIGURES 5.2 and 5.3.

Systems topologies					
	$\mathbf{P_{n,gen}}$[MW]	$\mathbf{P_{load}}$[MW]	$\mathbf{\Delta P_{load}}$[MW]	$\mathbf{S_{th}}$[%]	$\mathbf{S_{eff}}$[%]
One-node system	3008	3008	100	5	4.745
Belgian HV Grid	3008	12 000	1000	5	4.738

TABLE 5.1: System topologies for both scenarios

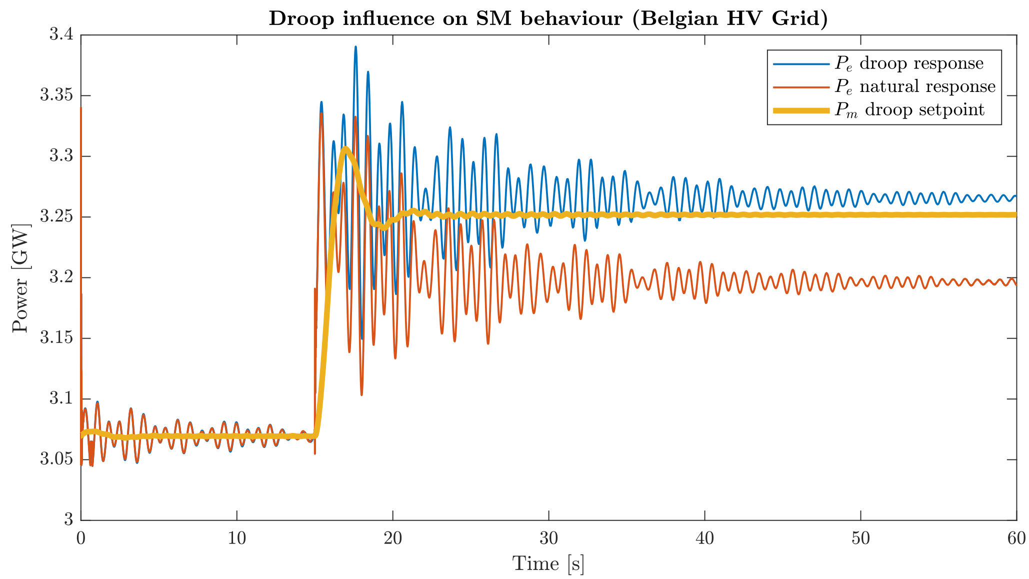

FIGURE 5.3: Power injected by Tihange equivalent SM on BHVG

Moreover, an observation can be made for both systems. Indeed, there is a static error between droop setpoint P_m and the power injected by SM P_e. The power injected by the SM is greater than the setpoint, which means that the effective droop is lower than the mechanical one. We understand that this result is physically not correct but no explanation has been found yet for this error. However, this static error will not influence the trends of the frequency response studied in this chapter.

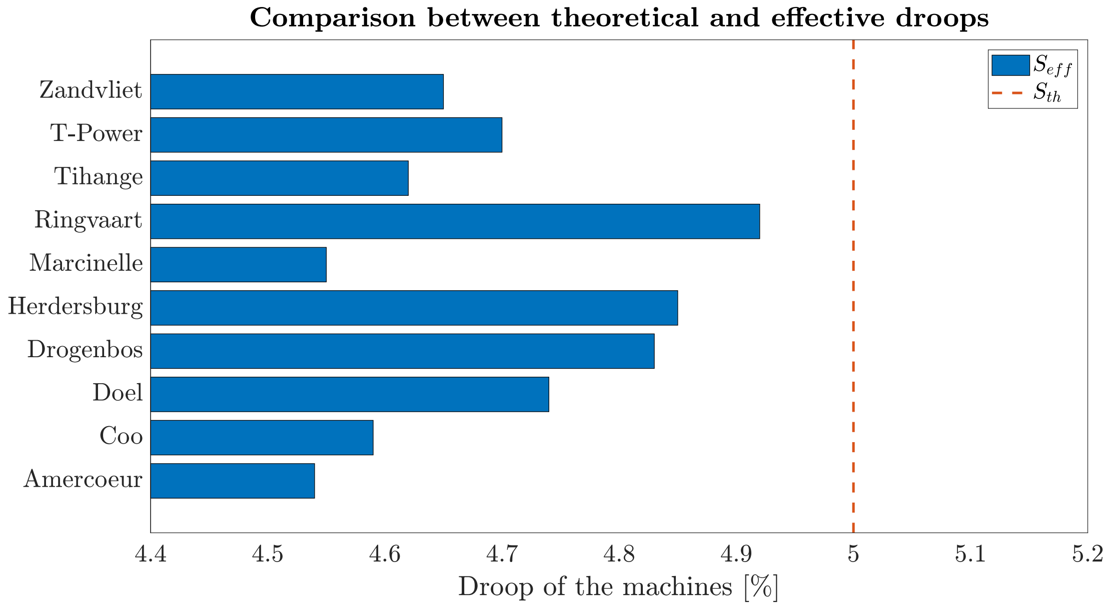

FIGURE 5.4: Comparison between theoretical (S_{th}) and effective (S_{eff}) droops

FIGURE 5.4 shows the difference between the theoretical droop and the effective droops for each generator. The effective droops are all under the theoretical value, which means that the generators inject slightly more power than in theory. This difference has to be taken into account in the calculations in the next sections as it can have an impact on the $\mathbf{\Delta f_{eq}}$ value. In order to take this into account, an effective droop of the machines can be computed as the weighted average of the individual droop constants of the SM, divided by their nominal power :

$$S_{g,eff} = P_{Ntot} \sum_{i=1}^{N} \frac{S_i}{P_{Ni}} = 4.64 \ [\%] \tag{5.2}$$

Theoretically, all the others parameters kept constant, a difference of $0.05 - 0.0464 = 0.0036[p.u]$ in the droop value can result in an error of 7.7 [%] in $\mathbf{\Delta f_{eq}}$ estimation, based on *Equation* 5.8 .

5.2 Parametric analysis

This section will focus on the impact of the two main coefficients of VSG, D and H, on grid frequency. As a reminder, the power injected in the grid is given by :

$$P_{VSG} = K_D \Delta\omega + K_I \frac{d\Delta\omega}{dt} = P_{VSG,N}\left(\frac{1}{D}\frac{\Delta\omega}{\omega_0} + \frac{2H}{\omega_0}\frac{d\Delta\omega}{dt}\right)$$

Where D is the droop coefficient of the VSG, and H its inertia constant. The first one multiplies the grid frequency deviation while the second multiplies its derivative (RoCoF).

In this section, all simulations are based on the same disturbance : at t = 25 [s], a new load of 2 [GW] is connected to the low voltage grid, at 150 [kV]. Please note that the orders of magnitude for load perturbation and P_{VSG} ([GW] order of magnitude) are much bigger than realistic values. This is done for purely academic purpose in order to clearly observe the influence of the parameters of the VSG. The next sections will deal with much more realistic quantities to analyze scenarios close to reality.

5.2.1 Influence of droop coefficient D

In order to study the impact of D on the system behaviour, 4 values are investigated : $D = 5\%$, $D = 1\%$, $D = 0.5\%$, and $D = 0.1\%$. For clarity, $D = 5\%$ is not shown in FIGURE 5.5 but is included in TABLE 5.2. This set of values is chosen since for classical governors, a droop of 5 % is a typical value. For the VSG application, this value is too high to have a significant effect. Therefore, smaller values have been investigated.

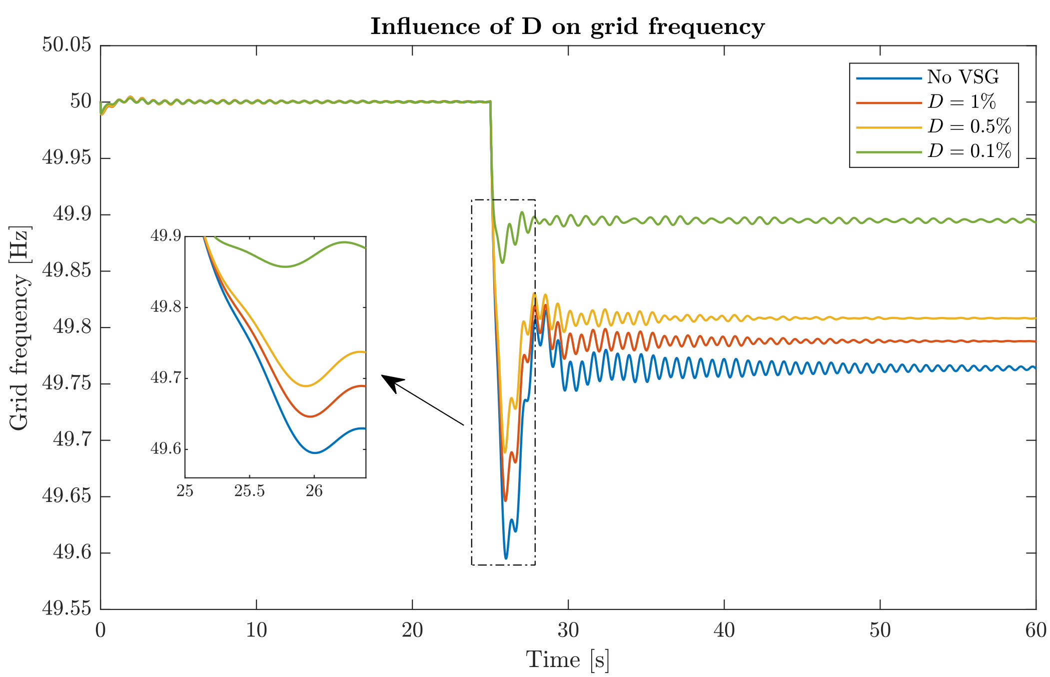

FIGURE 5.5: Grid frequency for several droop values

First of all, the main effect observable in FIGURE 5.5 is that as for classical frequency control, the droop of the VSG helps to reduce the frequency deviation at a new equilibrium, awaiting the action of secondary control. The smaller the droop, the greater the power injected and thus the smaller the final frequency deviation and frequency nadir.

Droop Analysis					
D [%]	$\mathbf{\Delta f_{nadir}}$ [mHz]	**Reduction** [%]	**RoCoF** [mHz/s]	**Reduction** [%]	$\mathbf{P_{max}}$ [MW]
/	405	/	- 695	/	/
5	394	2.6	- 693	0.1	78
1	354	12.6	- 681	2.1	350
0.5	311	23.3	- 664	4.5	614
0.1	143	64.8	- 621	10.7	1 387

TABLE 5.2: Evolution of frequency and other parameters when varying the droop coefficient

TABLE 5.2 shows the impact on frequency deviation reduction. With a typical droop value of 5%, the impact is negligible : the frequency nadir is decreased by only 2%. With $D = 1\%$, a positive effect is observable since the nadir is decreased by more than 12%. An extreme value of $D = 0.1\%$ shows very good results, with a frequency nadir reduction greater than 64%.

But FIGURE 5.6 shows that the peak of injected power is about 1.4 [GW], which represents 11% of the total electrical power produced on the Belgian grid. This value is clearly not realistic, but the order of magnitude of power values is studied in the next sections.

Another issue that is discussed further is the energy injected during an imbalance. Indeed, this must not be neglected during the sizing of the system if the converter-side of VSG is connected to BESS and RES, as seen on right-hand side of FIGURE 5.6.

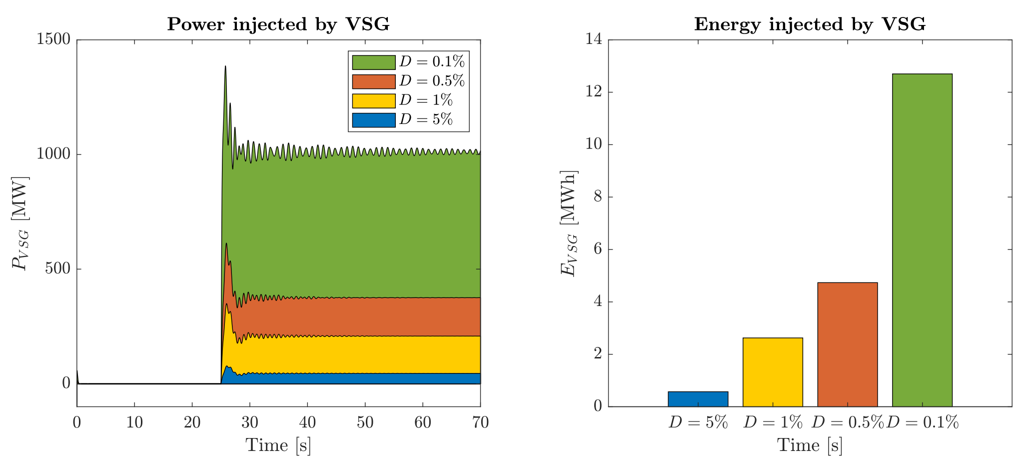

FIGURE 5.6: Power and energy injection for several droop values

The overshoot of power in FIGURE 5.6 in the first seconds after the disturbance is explained by grid frequency dynamics. Indeed, the frequency nadir is reached in a few seconds before stabilizing to a higher frequency value at the new steady-state. The power injected follows the same evolution since it is proportional to frequency : the power overshoot corresponds to the frequency nadir before reaching a steady-state power corresponding to the frequency equilibrium reached.

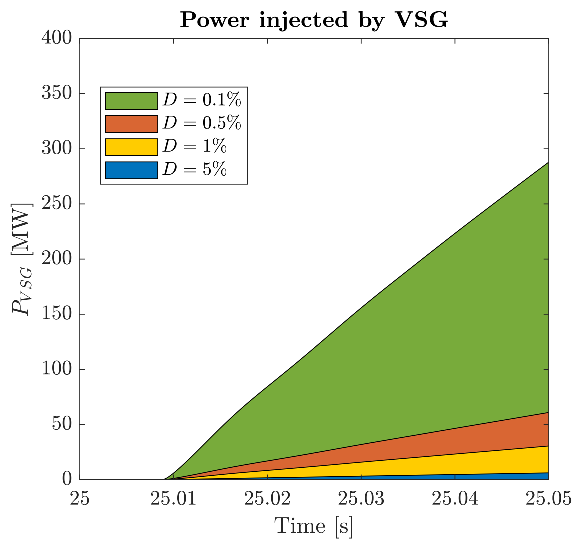

FIGURE 5.7: Droop influence on the inertial response

A last thing to notice is the RoCoF reduction with only the droop part of P_{VSG}. For regular rotating machines, the droop effect has no influence on the initial RoCoF since it takes a few seconds for primary control to take part in frequency regulation, while the inertial response lies in the milliseconds time-scale. However, since for the VSG the control is done by power electronics, the droop has an immediate effect on the power injection, and thus influences the initial RoCoF in the first milliseconds after the imbalance, as seen in FIGURE 5.7.

5.2.2 Influence of inertial coefficient H

As introduced previously, the goal of the inertial coefficient K_I is to reduce the RoCoF in the very first instants after an imbalance. Decreasing the slope of the frequency evolution after the disturbance theoretically allows to also reduce the frequency nadir.

Some observations can be made on the basis of FIGURE 5.8.

- First, the steady-state frequency after disturbance does not vary a lot with H. It is normal, since by definition at steady state the derivative is close to 0, so the derivative term of P_{VSG} has no longer an impact. The inertial term is thus not useful to reduce the final frequency deviation.
- The right-hand side of FIGURE 5.8 shows the behaviour of frequency in the first 150 [ms] after the imbalance. The RoCoF can be approximated as linear on this time interval. It is useful in order to compute the RoCoF in a more physical way than looking at numerical values of a derivative block in SIMULINK. It becomes $\dfrac{df}{dt} \simeq \dfrac{\Delta f}{\Delta t}$.

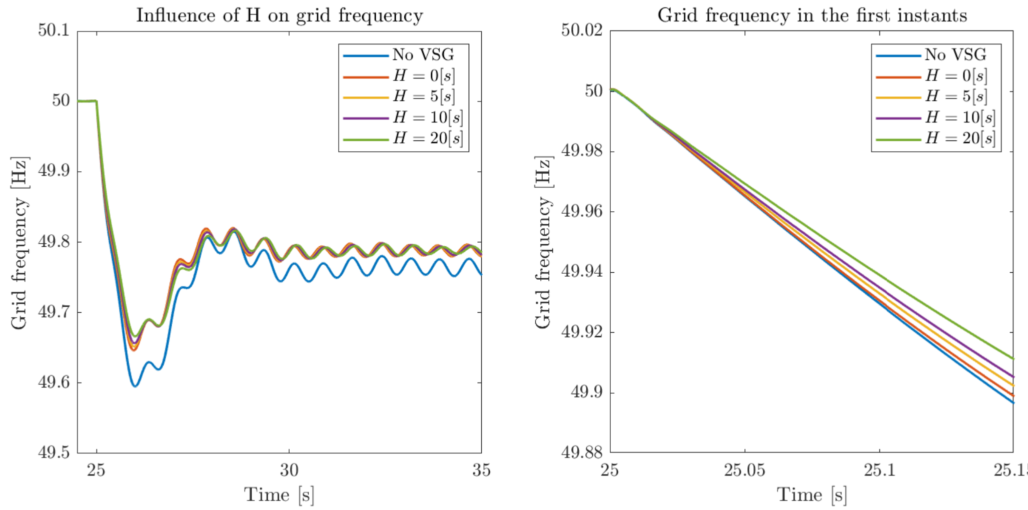

FIGURE 5.8: Frequency and RoCoF behaviour after an imbalance of 2 [GW]

Inertial Analysis					
H [s]	Δf_{nadir} [mHz]	Reduction [%]	RoCoF [mHz/s]	Reduction [%]	P_{max} [MW]
No VSG	405	/	- 695	/	/
0	354	12.6	- 682	2	348
5	349	14.0	- 660	5.2	353
10	344	15.1	- 640	8	368
20	338	16.5	- 600	13.8	409

TABLE 5.3: Evolution of frequency and other parameters when varying the inertial coefficient

TABLE 5.3 describes the impact of inertia constant H of VSG. The reduction of Δf_{nadir} with H is lower than with the droop. The real advantage of adding an inertial term is the enhanced RoCoF reduction. As shown in TABLE 5.4, the RoCoF reduction with inertial support is nearly equal to the one with the droop control. However, when comparing the maximum power injected by both methods, it is clear that the inertial support achieves the same results but with less power injection.

Decreasing D		Increasing H	
RoCoF Reduction [%]	P_{max} [MW]	RoCoF Reduction [%]	P_{max} [MW]
2	350	2.1	348
5.2	614	4.5	353
13.8	1387	10.7	409

TABLE 5.4: Power injection comparison

For a low RoCoF reduction value ($\sim 2\%$), the maximum injected power is nearly the same with D and with H. But when the RoCoF diminution becomes much more significant (i.e 5 -

10 %), the P_{max} needed to achieve a certain RoCoF reduction is much lower with the inertial response. For the same order of magnitude of RoCoF reduction ($\sim$ 10-13 %), the peak power is reduced by a factor 3 with the inertial part. Here lies the greatest advantage of adding an inertial term to P_{VSG}.

Finally, the reason of the RoCoF reduction at lower P_{max} is shown in FIGURE 5.9. The blue curve is the behaviour of P_{VSG} when no inertial term is added. Thus, since Δf remains small in the first instants after the imbalance, , P_{VSG} is not significant enough to counteract the high RoCoF. Adding a term proportional to this one helps the VSG to inject power in the very first milliseconds. It allows to be much more reactive during the inertial behaviour of the grid frequency and to reduce the RoCoF in an efficient way. The influence of H is limited during this timescale, and vanishes after a few seconds as it can be seen on the lower right-hand side of FIGURE 5.9. The energy emitted by the VSG (i.e the area under the power curve) is not really influenced by H, its variation is lower than 1%.

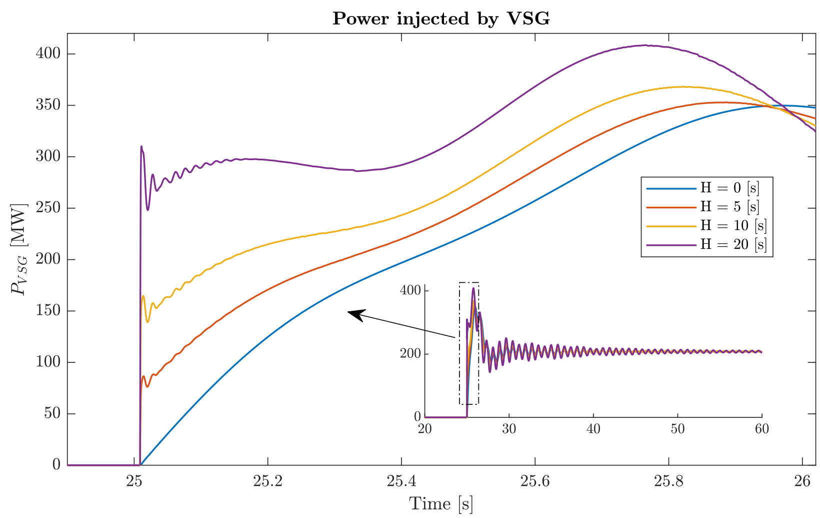

FIGURE 5.9: Influence of H on P_{VSG}

5.2.3 Influence of location of VSG

One of the modelling choices is to represent the VSG as a single VSG located at only one place. In practice, the power injected by the units it represents cannot be located at one place, and the equivalent VSG represents in fact multiple smaller power units located at various places in the grid. However, an equivalent VSG is modelled here, mainly to limit the computational time.

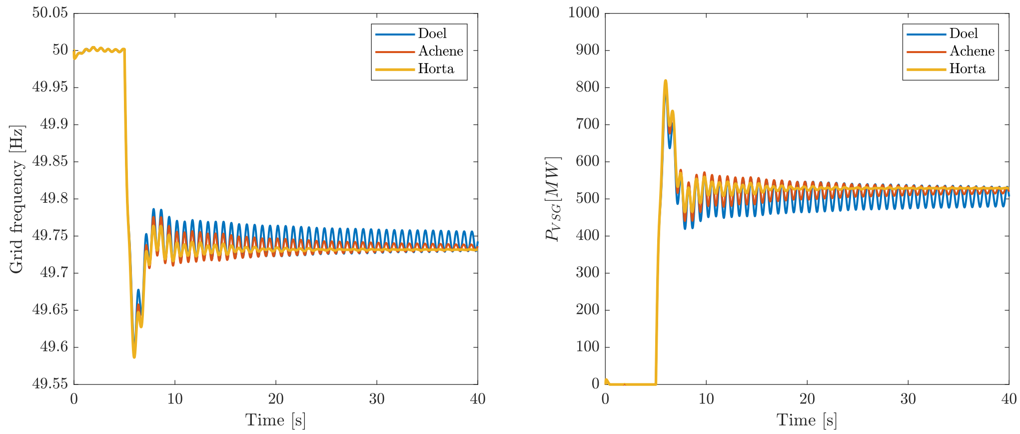

FIGURE 5.10: Influence of VSG location on frequency and power

Depending on where the power injection is achieved, the amplitude of resulting oscillations of frequency and thus P_{VSG} changes, as seen in FIGURE 5.10. Here, the load connection is near Horta. The closer the disturbance is to the power injection of the VSG, the smaller the oscillations will be. In order to make the graphs as readable as possible, most of the simulations are done with a VSG relatively close to the disturbance.

Some conclusions

- The most effective way to reduce Δf_{nadir} and Δf_{eq} is to play on the droop coefficient of P_{VSG}. The lower the droop, the lower the frequency deviation. Some limits must be defined to be able to inject such power values in a real implementation of VSG.

- The most effective way to reduce the RoCoF in the first instants after the imbalance is to play on inertial coefficient of P_{VSG}. If the droop part of VSG is self-sufficient to enhance frequency dynamics, this is not the case for the inertial part. Indeed, the inertial action of the VSG is limited in a smaller timescale and it will not allow to reduce the final frequency deviation.
  What is interesting is the complementarity of the inertial part with the droop part : first, the inertial part can reduce Δf_{nadir} by a few percent more than the droop without significantly increasing the injected power. Then, the inertial part reduces the initial RoCoF for a much lower P_{max} than what would be required if it were to be done by the droop control.

- A more concrete impact on the grid behaviour is that reducing the RoCoF can prevent the RoCoF relays from unnecessary tripping. This kind of event are unwanted, as explained in SECTION 1.3

5.3 Distribution grid : influence of variable loads

5.3.1 Theory

As explained in SECTION 4.4, the presence of dispersed generation and rotating loads in the downstream grids make the load respectively time-varying and frequency dependent. Therefore, the distribution grid is modelled as a set of static frequency-dependent loads. As a reminder, this model is described by *Equation* 5.3 [68], with α set to 0 here :

$$P_{load} = P_0(1 + K_{pf}\frac{(f - f_0)}{f_0})\left(\frac{V}{V_0}\right)^{\alpha} \tag{5.3}$$

With

- P_{load} : the effective consumption of the load
- P_0 : the nominal consumption of the load
- f : the frequency of the grid
- f_0 : the nominal frequency of the grid (50Hz)
- K_{pf} : the load frequency dependency factor

The value of K_{pf} varies depending on the type of load. According to [69], distribution grids have a K_{pf} that lies between 0 and 3 [69]. As we see from *Equation* 5.3, variable loads consume less power in states of under-frequency in the grid and more power in states of over-frequency. Therefore, variable loads are mitigating the frequency deviations in the grid as they counteract the power imbalance.

5.3.2 Simulations

FIGURE 5.11 shows the impact of the variable loads on the grid frequency during a disturbance. It was obtained by switching a load of 3000 [MW] on the grid after 10 seconds and shows the frequency response for several values of load frequency dependency factor. An important note is that the values of K_{pf} in this example are abnormally high compared to reality in order to better show its influence.

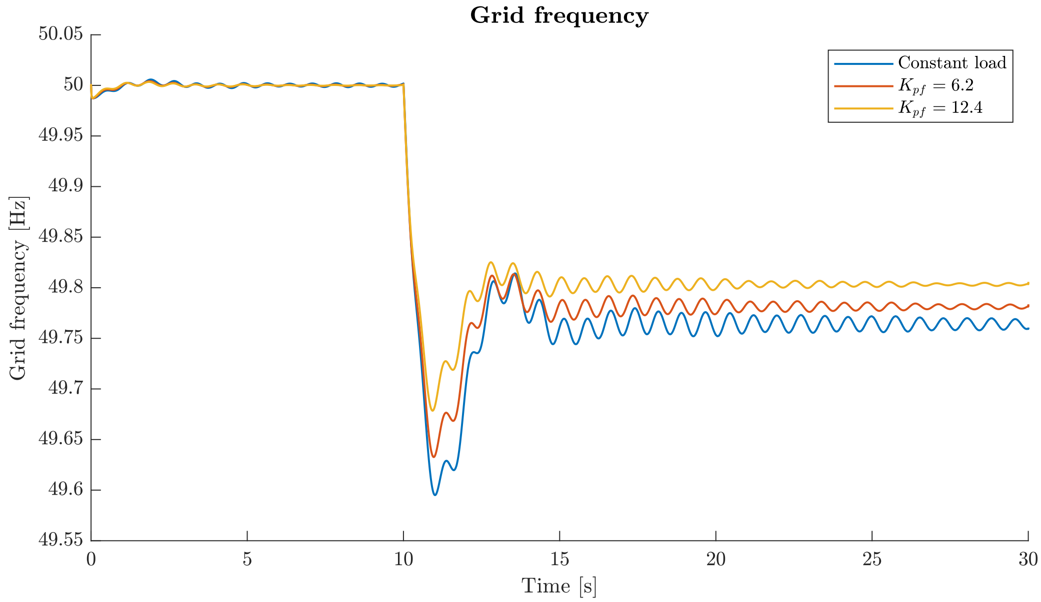

FIGURE 5.11: Influence of variable loads on the grid frequency with high K_{pf}

This confirms the positive influence of variable loads on the grid frequency. Not only do variable loads attenuate the frequency deviations but they also help to damp the oscillations. TABLE 5.5 summarizes the influence of variable loads on key parameters of the grid frequency.

Influence of variable loads on the grid frequency with high K_{pf}					
K_{pf} [pu]	Δf_{nadir} [Hz]	Reduction[%]	RoCoF [mHz/s]	Δf_{eq} [Hz]	Reduction[%]
/	0.405	/	- 731	0.241	/
6.2	0.367	9.4	- 736	0.219	9.1
12.4	0.321	20.7	- 733	0.197	18.3

TABLE 5.5: Influence of variable loads on critical parameters of the grid frequency with high K_{pf}

As seen in TABLE 5.5, variable loads reduce the frequency nadir and the frequency deviation at the equilibrium but they do not have an influence on the RoCoF. Higher frequency dependency factors lead to a greater mitigation of frequency nadirs and deviations at the equilibrium. However, in practice K_{pf} is between 0 and 3 [p.u] and the influence of variable loads is thus limited.

FIGURE 5.12 shows the influence of variables loads with a more realistic load dependency factor of 2.8 [p.u].

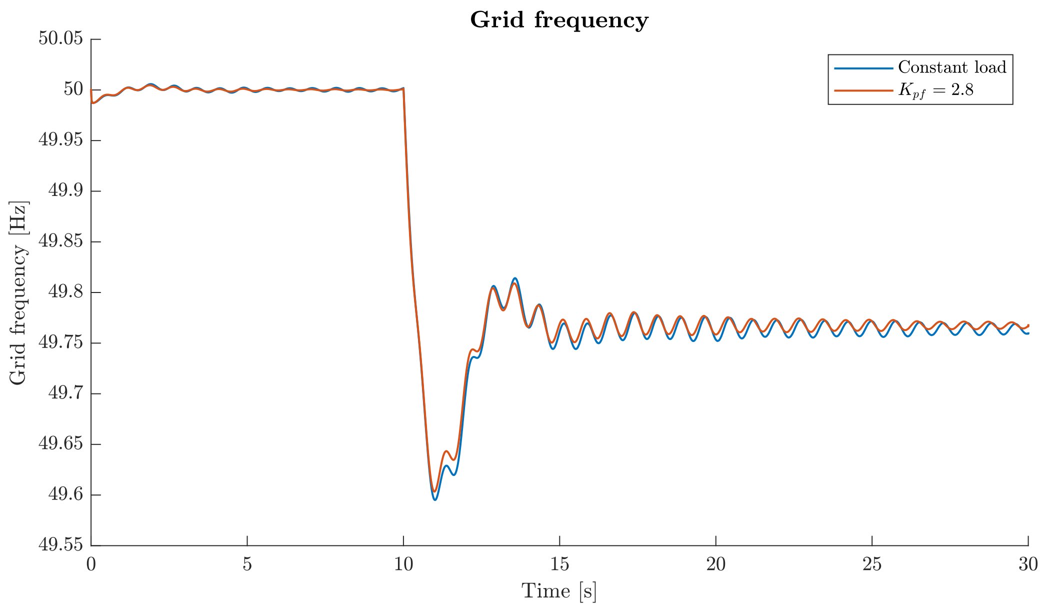

FIGURE 5.12: Influence of variable loads on the grid frequency with a realistic K_{pf}

Influence of variable loads on the grid frequency with a realistic K_{pf}					
$\mathbf{K_{pf}}$ [pu]	$\mathbf{\Delta f_{nadir}}$ [Hz]	**Reduction** [%]	**RoCoF** [mHz/s]	$\mathbf{\Delta f_{eq}}$ [Hz]	**Reduction** [%]
/	0.405	/	- 731	0.241	/
2.8	0.397	2.1	- 733	0.233	3.3

TABLE 5.6: Influence of variable loads on critical parameters of the grid frequency with a realistic K_{pf}

As seen in FIGURE 5.12 and TABLE 5.6, the influence of the variable loads on the grid frequency is relatively small. The frequency deviation is reduced by a few percents and the RoCoF is still unchanged.
As variable loads have little influence on the grid frequency and significantly increase the computational time of simulations, loads with constant impedance are used for further analysis.

Some conclusions

- Variable loads reduce the frequency nadir during a disturbance
- Variable loads reduce the frequency deviation at the equilibrium after a disturbance
- Variable loads have no influence on the RoCoF during a disturbance
- With a realistic K_{pf} the influence of variable loads is limited to a few percent.

5.4 Loss of a generator

In this section, the influence of the loss of a generator on the grid frequency is analyzed. The aim is to determine if this type of power imbalance has a larger influence on the grid frequency than the connection of an additional load. To this end, the frequency deviation of the grid due to the loss of a generator is compared to the deviation caused by the connection of a load of same power as the generator. Then, the underlying reasons of this difference are explained.

Frequency response To begin with, let us compare the frequency response of the two types of power imbalance. FIGURE 5.13 shows the frequency response of the grid with the loss of a generator and the connection of an additional load. The generator loss curve was obtained by disconnecting the power plant of Amercoeur and thus losing 451 [MW] of generation. The additional load curve is obtained by connecting to the grid a 451 [MW] load at the same location as Amercoeur.

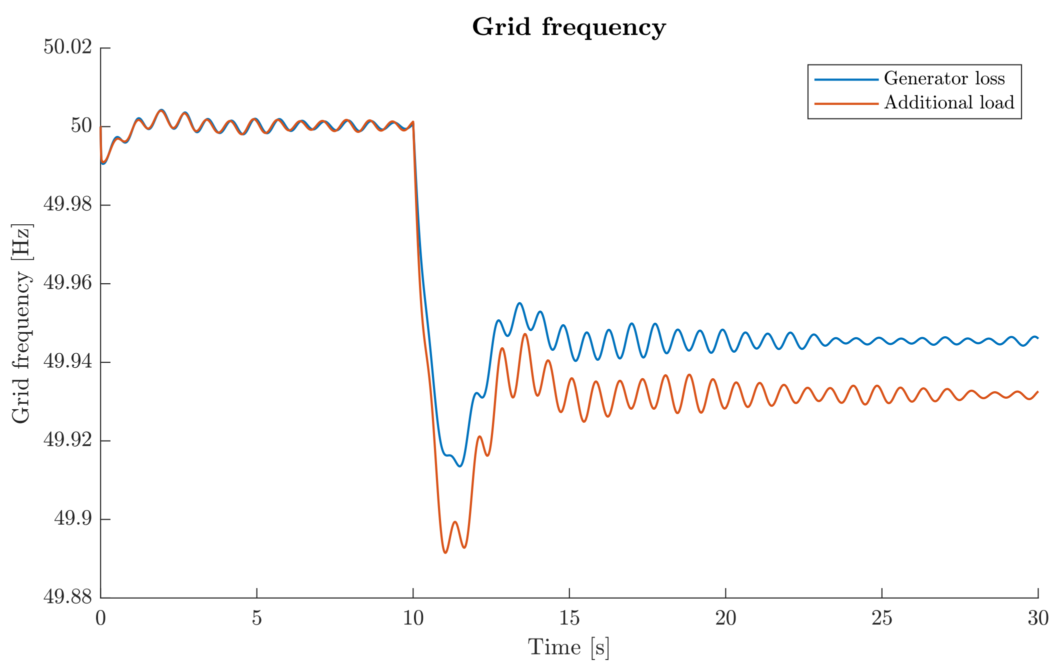

FIGURE 5.13: Grid frequency response due to a generator loss and a load connection

As seen in FIGURE 5.13, the sudden loss of a generator has a lesser impact on the grid frequency than the connection of an additional load. This result might seem strange as the power imbalance in both cases is the same. The difference in frequency response can be explained by the difference in effective power imbalance generated by the two imbalances. This is explained in detail in the following paragraphs.

Decrease in load consumption The difference in effective power imbalance created by the types of faults is due to the variation of voltage in the grid. The decrease of grid voltage generates a decrease in load power consumption as the loads are constant impedance loads. FIGURE 5.14 shows the decrease in voltage and load power for the two scenarios.

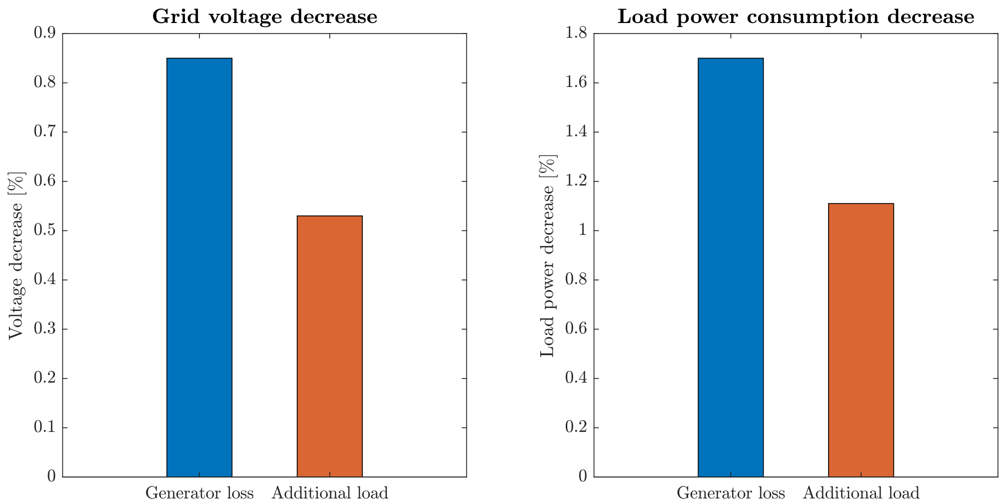

FIGURE 5.14: Voltage and load power decrease during imbalances

The loss of a generator causes a bigger voltage decrease than the connection of an additional load. This is due to the loss of reactive power initially provided by the disconnected generator. Because the distribution grid is modelled as a set of constant impedance loads, the decrease in voltage affects the power consumption in the grid. Thus, the loss of a generator induces a larger decrease of the load consumption than the connection of an additional load.
The active power consumption of a constant impedance load is dictated by *Equation* 5.4.

$$P \propto \left(\frac{V}{V_0}\right)^2 \tag{5.4}$$

Thus, the theoretical power decrease of the load power for a voltage drop is in percentage:

$$\Delta P_{load} = \frac{(1 + \dfrac{V - V_0}{V_0})^2 P_0}{P_0} \tag{5.5}$$

With:

- ΔP_{load} : the decrease in consumption of the loads in percentage
- P_0 : the initial power consumption of the loads
- V : the new voltage after the imbalance
- V_0 : the initial voltage

The theoretical decrease in load power is compared to the real decrease obtained with simulation in TABLE 5.7.

Influence voltage on the load consumption				
Scenario	$\mathbf{\Delta V}$ [%]	**Theoretical** $\mathbf{\Delta P_{load}}$ [%]	**Real** $\mathbf{\Delta P_{load}}$ [%]	**Error** [%]
Generator loss	0.84	1.69	1.70	0.6
Additional load	0.54	1.08	1.12	3.6

TABLE 5.7: Influence of the voltage decrease on the load consumption for the loss of a generator and the connection of an additional load

The theoretical results match the results obtained by simulation. The hypothesis that the drop in power consumption of the load is caused by the drop in voltage is thus correct.

Effective power imbalance It has been proved in the previous paragraphs that the loss of a generator induces a larger voltage drop than the connection of an additional load, which results in a larger decrease in load consumption. Therefore, the effective power imbalance in the two cases is different even if the additional load and the lost generator have the same nominal power.
The effective power imbalance created by the disconnection of a generator is given by *Equation* 5.6.

$$\Delta P_{eff} = P_{gen} - \Delta P_{load} \tag{5.6}$$

With:

- ΔP_{eff} : the effective power imbalance created by the loss of the generator
- P_{gen} : the nominal power of the lost generator
- ΔP_{load} : the decrease in consumption of the loads in the grid

Subsequently, the effective power imbalance created by the connection of an additional load is given by *Equation* 5.7.

$$\Delta P_{eff} = P_{add} - \Delta P_{load} \tag{5.7}$$

With:

- ΔP_{eff} : the effective power imbalance created by the connection of the additional load
- P_{add} : the nominal power of the additional load
- ΔP_{load} : the decrease in consumption of the loads in the grid

TABLE 5.8 summarizes the effective power imbalance created in the two scenarios.

Effective power imbalance			
Scenario	$\mathbf{P_{nom}}$ [MW]	$\mathbf{\Delta P_{load}}$ [MW]	$\mathbf{\Delta P_{eff}}$ [MW]
Generator loss	451	199	252
Additional load	451	133	314

TABLE 5.8: Effective power imbalance created by the loss of a generator and by the connection of an additional load

The difference in effective power imbalance explains the difference between the frequency response of the two scenarios. The effective power imbalance created by the connection of an additional load is bigger and it leads to a greater frequency deviation.

Equilibrium frequency Let us compare the theoretical equilibrium frequency after disturbance with the frequency deviations obtained by simulation. As a reminder, the loads are modelled without frequency dependency and thus their power consumption does not vary as the frequency changes (K_{pf}=0).
The equilibrium frequency deviation after the loss of a generator is given by *Equation* 5.8

$$\Delta f_{eq} = \frac{-P_k}{\frac{1}{f_0}\sum_{i\neq k}^{N}\frac{P_{Ni}}{S_i}} \tag{5.8}$$

With:

- Δf_{eq} : the equilibrium frequency deviation
- $-P_k$: the nominal power of the lost generator
- f_0 : the nominal frequency of the grid (50Hz)
- P_N : the nominal power of the generators with droop control
- S : the droop constant of the generator (here 5%)

In this case, the nominal power of the lost generator is seen by the grid as the effective power imbalance created by the disconnection of the generator.

Then, the equilibrium frequency deviation after the connection of a new load is given by *Equation* 5.9.

$$\Delta f_{eq} = \frac{-\Delta P_c}{\frac{1}{f_0}\sum_{i=1}^{N}\frac{P_{Ni}}{S_i}} \tag{5.9}$$

With ΔP_c the change in load power consumption after connection of the additional load.

Again, the change of load power consumption is seen by the grid as the effective power imbalance after connecting the additional load.

TABLE 5.9 summarizes the theoretical and the real frequency deviation at the equilibrium for both scenarios.

Equilibrium frequency deviation				
Scenario	$\mathbf{\Delta P_{eff}}[MW]$	**Theoretical** $\mathbf{\Delta f_{eq}}$ $[\mathrm{mHz}]$	**Real** $\mathbf{\Delta f_{eq}}$ $[\mathrm{mHz}]$	**Error** $[\%]$
Generator loss	252	53.8	54.6	1.4
Additional load	296.7	64.6	68.6	6.1

TABLE 5.9: Equilibrium frequency deviation after the loss of a generator and the connection of an additional load

The small error between the calculated theoretical values and the simulation values can be explained by the inaccuracy on the droop constant. Indeed, the droop constant used for the theoretical calculation is the mechanical droop constant of the generators. As shown in SECTION 5.1, the effective droop constant for the electric power of the generators is smaller than the nominal value of 5% set to control the turbine. With the electrical droop control constants the errors between the theoretical frequency deviations and the real frequency deviations drops below 2%.

Rate of Change of Frequency Next to the equilibrium frequency, another important aspect of the frequency response is the RoCoF. This section will analyse the theoretical value and the simulation value.
The theoretical initial RoCoF created by a power imbalance is given by *Equation* 5.10 [13].

$$\text{RoCoF} = \left.\frac{df}{dt}\right|_{t_{imb}} = \frac{f_0\,\Delta P}{H_g\,P_N} \tag{5.10}$$

With:

- ΔP : the power imbalance in the grid
- f_0 : the nominal frequency of the grid (50Hz)
- H_g : the inertia constant of the grid
- P_N : the sum of the generators nominal power
- t_{imb} : the time at which the imbalance is initiated

The value of the power imbalance in the grid is given by the effective power imbalance calculated previously. The sum of the generators nominal power and the nominal frequency are also known. The inertia constant of the grid is still to be determined with *Equation* 5.11 and the data summarized in TABLE 4.2, 4.3, 4.5 and 4.6.

$$H_g = \frac{\sum_{i=1}^{N} H_i S_{Bi}}{\sum_{i=1}^{N} S_{Bi}} = 3.62 \quad [s] \tag{5.11}$$

With these parameters and *Equation* 5.10, the theoretical value of the RoCoF in both scenarios can be calculated and compared to the values obtained by simulation. The real RoCoF is obtained using the first 100 [ms] of the simulation and taking the average RoCoF over this period.
TABLE 5.10 summarizes the RoCoF values for both scenarios.

Rate of Change of Frequency			
Scenario	**Theoretical RoCoF** $[\mathrm{mHz/s}]$	**Real RoCoF** $[\mathrm{mHz/s}]$	**Error** $[\%]$
Generator loss	232	216	7.2
Additional load	289	267	8.2

TABLE 5.10: RoCoF after the loss of a generator and the connection of an additional load

From TABLE 5.10, we see that the real values of the RoCoF are smaller than the theoretical values. The small error could be caused by the time window taken to calculate the average RoCoF from the simulation results. Indeed, the measure time window influences the results.

In summary, several results from the simulation have been analysed and their validity has been confirmed by their alignment with the theoretical results. The real values of load consumption, equilibrium frequency and rate of change of frequency results being all similar to the the theoretical values, the simulation model is accurate and it can be used to analyse the influence of the VSG.

Some conclusions The connection of an additional load compared to the loss of a generator creates:

- A smaller voltage decrease
- A smaller load power consumption decrease
- A bigger effective power imbalance
- **A larger deviation at the equilibrium of the grid frequency**
- **A larger RoCoF of the grid frequency**

5.4.1 Influence of the VSG

Now that we have compared the frequency response of the grid for two types of imbalance, it is important to determine if the impact of the VSG is the same for both scenarios. For this purpose, we used a VSG with an inertia constant H = 10 [s], a droop $D = 0.5\%$ and various values of nominal power. FIGURE 5.15 shows the influence of a VSG with several nominal powers on the frequency response.

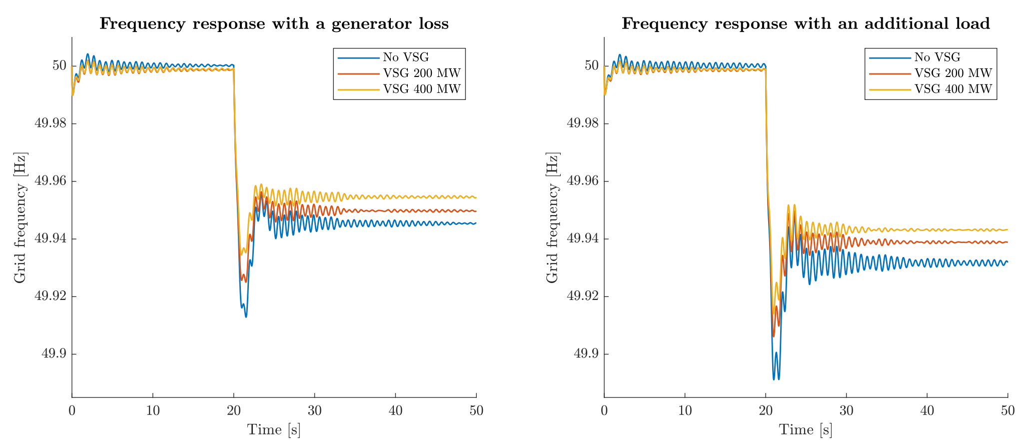

FIGURE 5.15: Influence of the VSG on the frequency response during the loss of a generator and the connection of an additional load

As seen in FIGURE 5.15, the VSG significantly improves the frequency response in both cases.

The VSG reduces the frequency nadir, the equilibrium frequency deviation and also the RoCoF.

Equilibrium Frequency Let us begin with comparing the effectiveness of the VSG in reducing the equilibrium frequency deviation for both scenarios.

Influence of the VSG on the equilibrium frequency		
Scenario	**VSG 200 [MW]**	**VSG 400 [MW]**
/	$\mathbf{\Delta f_{eq}}$ **Reduction** $[\mathrm{mHz}]$	$\mathbf{\Delta f_{eq}}$ **Reduction** $[\mathrm{mHz}]$
Generator Loss	4.3	8.8
Additional Load	7.4	11.8

TABLE 5.11: Influence of the VSG on the frequency response for the loss of a generator and the connection of an additional load

As noticed in TABLE 5.11, the VSG has a higher impact on the reduction of Δf_{eq} for the additional load scenario than for the generator loss scenario. This can be explained by the dependency of the output power of the VSG with the grid frequency deviation (see *Equation* 3.1). Indeed, the bigger the frequency deviation, the more power the VSG is going to inject in the grid.

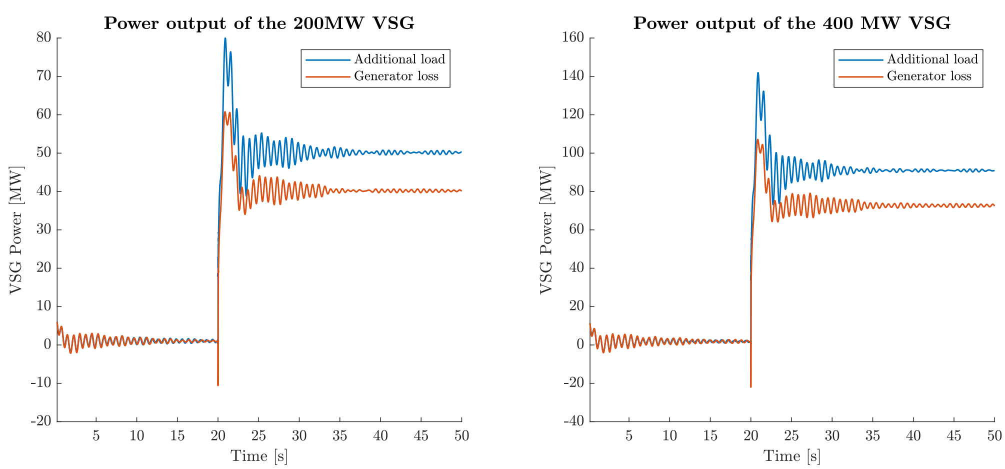

FIGURE 5.16: Power output of the VSG during the loss of a generator and the connection of an additional load

As shown in FIGURE 5.16, the power output of the VSG is bigger during the connection of the additional load than during the loss of a generator. This is because the effective power imbalance created by the connection of an additional load is higher than the one created by the loss of a generator. Therefore, the VSG will inject more power and thus be more efficient at reducing the frequency deviation during the imbalance.

In order to validate the simulation results of the impact of the VSG on Δf_{eq}, it is important to compare them to the theoretical values. Let us first compute the new theoretical equilibrium frequency deviation with the VSG by adapting *Equation* 5.12 for the loss a generator and *Equation* 5.13 for the connection of an additional load.

$$\Delta f_{eq} = \frac{-P_k}{\frac{1}{f_0}\left(\sum_{i\neq k}^{N}\frac{P_{Ni}}{S_i} + \frac{P_{VSG,N}}{D}\right)} \tag{5.12}$$

$$\Delta f_{eq} = \frac{-\Delta P_c^0}{\frac{1}{f_0}\left(\sum_{i=1}^{N}\frac{P_{Ni}}{S_i} + \frac{P_{VSG,N}}{D}\right)} \tag{5.13}$$

All parameters stay the same except the term $\sum_{i=1}^{N}\frac{P_{Ni}}{S_i}$ that has to be adapted. Indeed, the nominal power of the VSG divided by its droop constant ($D = 0.5\%$) has to be included in the sum. The results are given in TABLE 5.15 and TABLE 5.16.

Equilibrium frequency deviation with the 200 [MW] VSG			
	Theoretical	Real	
Scenario	**Δf$_{eq}$ Reduction [mHz]**	**Δf$_{eq}$ Reduction [mHz]**	**Error [%]**
Generator loss	7.8	4.3	44
Additional load	9.1	7.4	19

TABLE 5.12: Equilibrium frequency deviation after the loss of a generator and the connection of an additional load with a 200 [MW] VSG

Equilibrium frequency deviation with the 400 [MW] VSG			
	Theoretical	Real	
Scenario	**Δf$_{eq}$ Reduction [mHz]**	**Δf$_{eq}$ Reduction [mHz]**	**Error [%]**
Generator loss	13.7	8.8	36
Additional load	16.0	11.8	26

TABLE 5.13: Equilibrium frequency deviation after the loss of a generator and the connection of an additional load with a 400 [MW] VSG

It can be seen that real reduction of the equilibrium frequency deviation with the VSG is smaller than the reduction suggested by the theoretical results. Moreover, there is a significant error between the theoretical results and the real results. However, this can be explained by the impact of the VSG on the voltage deviation caused by the imbalance.
FIGURE 5.17 shows the voltage deviation in the grid during the connection of an additional load for various values of VSG nominal power.

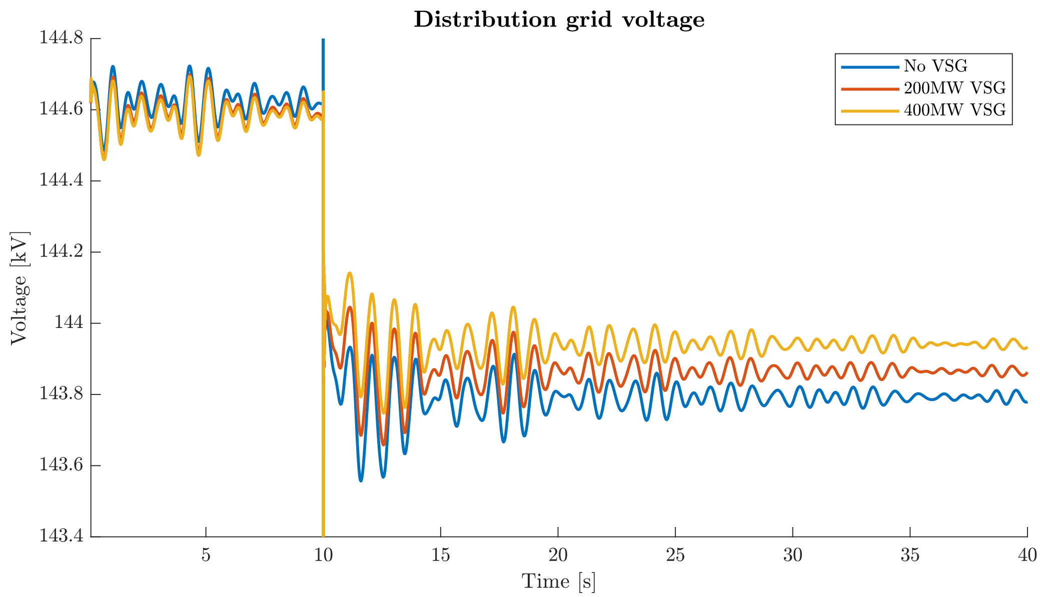

FIGURE 5.17: Grid voltage deviation during power imbalance for several values of VSG nominal power

The higher the nominal power of the VSG, the more it reduces the voltage deviation in the grid during an imbalance. As a result of the higher voltage in the grid with the VSG, the power consumption of the loads is higher than in the case with no VSG (constant impedance loads). Therefore, the effective power imbalance created by the connection of an additional load or the loss of a generator varies with the nominal power of the VSG.
TABLE 5.14 compares the effective power imbalance in the grid with for various nominal powers of the VSG.

Effective power imbalance $\Delta \mathbf{P}_{\mathbf{eff}}$			
Scenario	**No VSG**	**200 [MW] VSG**	**400 [MW] VSG**
	$\Delta \mathbf{P}_{\mathbf{eff}}$ $[MW]$	$\Delta \mathbf{P}_{\mathbf{eff}}$ $[MW]$	$\Delta \mathbf{P}_{\mathbf{eff}}$ $[MW]$
Generator loss	252	269	278
Additional load	314	328	343

TABLE 5.14: Effective power imbalance created by the loss of a generator and by the connection of an additional load for several nominal powers of the VSG

As seen in TABLE 5.14, the effective power imbalance increases as the nominal power of the VSG increases. Again, this can be explained by the ability of the VSG to mitigate the voltage drop which in turn mitigates the decrease in power consumption of the loads.
The change in effective power imbalance will affect the theoretical value of the equilibrium frequency of the grid. Let us now compare the new theoretical values of equilibrium frequency with the real values obtained by simulations and see if the error is reduced. TABLE 5.15 and TABLE 5.16 compare the new theoretical values of equilibrium frequency with the real values.

Equilibrium frequency deviation with the 200 [MW] VSG			
	Theoretical	Real	
Scenario	Δf_{eq} Reduction $[mHz]$	Δf_{eq} Reduction $[mHz]$	Error $[\%]$
Generator loss	4.74	4.3	9.3
Additional load	6.8	7.4	8.9

TABLE 5.15: Equilibrium frequency deviation after the loss of a generator and the connection of an additional load with a 200 [MW] VSG

Equilibrium frequency deviation with the 400 [MW] VSG			
	Theoretical	Real	
Scenario	Δf_{eq} Reduction $[mHz]$	Δf_{eq} Reduction $[mHz]$	Error $[\%]$
Generator loss	9.4	8.8	6.4
Additional load	11.6	11.8	1.9

TABLE 5.16: Equilibrium frequency deviation after the loss of a generator and the connection of an additional load with a 400 [MW] VSG

As seen in TABLE 5.15 and TABLE 5.16, the error between the theoretical and the real values is now below 10% and thus the two methods of calculation converge. Therefore, it can be concluded that the VSG droop control is behaving correctly and the simulation results for the equilibrium frequency are correct.

RoCoF Let us know see if there is a difference between the RoCoF reduction in both scenarios.

Influence of the VSG on the RoCoF		
Scenario	VSG 200 [MW]	VSG 400 [MW]
/	RoCoF Reduction $[mHz/s]$	RoCoF Reduction $[mHz/s]$
Generator Loss	11.5	23.3
Additional Load	13.3	25.2

TABLE 5.17: Influence of the VSG on the RoCoF for the loss of a generator and the connection of an additional load

As observed in TABLE 5.17, the RoCoF reduction is higher for the additional load scenario than for the generator loss scenario. This can be explained by the dependency of the VSG power output on the RoCoF in the grid. In other words, the higher the RoCoF in the grid, the more power the VSG will inject power in the grid (see *Equation* 3.1).
To validate the accuracy of the simulation results, they have to be compared with theoretical values. As a reminder the theoretical equation to calculate the RoCoF during an imbalance is given by *Equation* 5.14

$$\text{RoCoF} = \left.\frac{df}{dt}\right|_{t_{imb}} = \frac{f_0}{H_g}\frac{\Delta P}{P_N} \tag{5.14}$$

In this equation, both ΔP, H_g and P_N have to be adapted. For ΔP, the new values of effective power imbalance given in TABLE 5.14 have to be used. Then, the grid inertia constant H_g has to take into account the added grid inertia by the VSG and P_N has to include the nominal power of the VSG. The inertia constant of the grid calculated with a 200 [MW] VSG is given by *Equation* 5.15.

$$H_g = \frac{\sum_{i=1}^{N} H_i S_{Bi}}{\sum_{i=1}^{N} S_{Bi}} = 3.72 \quad [s] \tag{5.15}$$

And the inertia constant of the grid with a 400 [MW] VSG is given by *Equation* 5.16.

$$H_g = \frac{\sum_{i=1}^{N} H_i S_{Bi}}{\sum_{i=1}^{N} S_{Bi}} = 3.80 \quad [s] \tag{5.16}$$

Having now the values for all the parameters in *Equation* 5.14, we can compare the theoretical values with the real values as summarized in TABLE 5.18 and TABLE 5.19 .

RoCoF with the 200 [MW] VSG			
	Theoretical	**Real**	
Scenario	**Reduction** $[\mathrm{mHz}]$	**Reduction** $[\mathrm{mHz}]$	**Error** $[\%]$
Generator loss	8.25	11.5	28
Additional load	10.3	13.3	29

TABLE 5.18: RoCoF reduction due to the the loss of a generator and the connection of an additional load with a 200 [MW] VSG

RoCoF with the 400 [MW] VSG			
	Theoretical	**Real**	
Scenario	**Reduction** $[\mathrm{mHz}]$	**Reduction** $[\mathrm{mHz}]$	**Error** $[\%]$
Generator loss	15.9	23.3	32
Additional load	19.9	25.2	27

TABLE 5.19: RoCoF reduction due to the loss of a generator and the connection of an additional load with a 400 [MW] VSG

The real RoCoF reduction of the VSG is in reality higher than what the theoretical results predict. This can be explained by the fast response of the VSG droop control which react during the first moments of the imbalance. As explained in SECTION 5.1, the droop constant of the VSG influences the amount of power injected at the beginning of the power imbalance. With a droop constant of 0.5%, the VSG droop response is participating to the RoCoF reduction on top of the virtual inertia. Therefore, the impact it has on the RoCoF reduction is higher than the pure inertial response calculated by the theoretical results.

Some conclusions The impact of the VSG during a power imbalance in the grid is such that it:

- Decreases the voltage deviation created by an imbalance
- Reduces the deviation of the grid frequency at the equilibrium. The greater the nominal power of the VSG, the greater the reduction of the equilibrium frequency deviation.
- Reduces the RoCoF of the grid frequency. The greater the nominal power of the the VSG, the greater the reduction of the RoCoF.

5.5 Renewable Energy

The share of electricity produced by renewable energy sources is continuously increasing in Europe as a result of EU environmental and energy policies. Also, some European governments strive to decrease the production of electricity by nuclear reactors and replace it by RES. Therefore, the renewable penetration rate will further increase in the future and it is important to determine its influence on the stability in frequency of the grid. The various renewable penetration rates are obtained by adapting the production of wind and nuclear energy while keeping the total production constant, as seen in FIGURE 5.18.

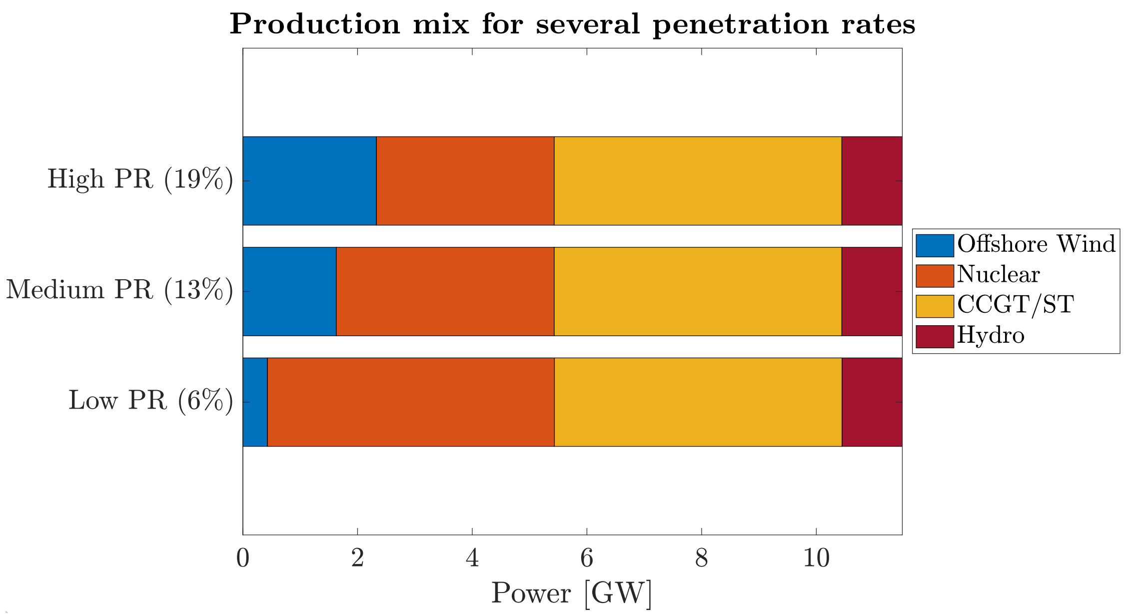

FIGURE 5.18: Electricity mix distribution influencing on RES penetration rate

FIGURE 5.19 shows the influence of the renewable penetration rate on the frequency response for a power imbalance. The simulation was done with a total power production of 11.5 [GW] and an imbalance of 200 [MW].
The initial purpose of this section was to study the total closure of Belgian nuclear power plants. However, for computational time reasons, a penetration rate upper limit constrained us to reduce the nuclear power production by only a factor 2.
As a reminder, the penetration rate of renewable is the power produced by renewable energy sources divided by the total power produced and is given by *Equation* 5.17.

$$p_{rate} = \frac{P_{renewable}}{P_{tot}} \tag{5.17}$$

With

- p_{rate}: the penetration rate
- $P_{renewable}$: the power produced by renewable energy sources (here only offshore wind)
- P_{tot}: the total power produced

FIGURE 5.19 shows the frequency response of the grid during an imbalance for several penetration rates of renewable energy.

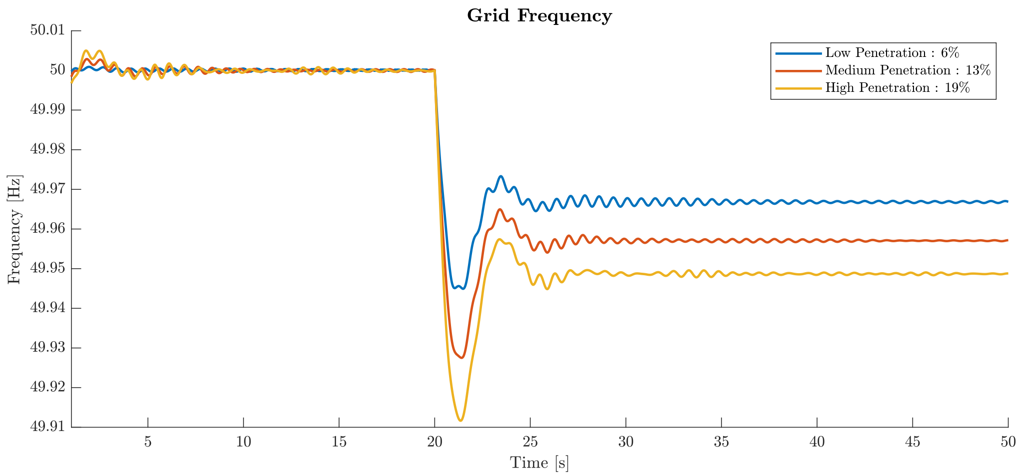

FIGURE 5.19: Influence of the renewable penetration rate on the frequency response of the grid during a 200 [MW] power imbalance

As seen in the figure, the renewable penetration rate has a significant influence on the grid frequency. The higher the penetration rate, the greater the frequency deviation during a power imbalance.
TABLE 5.21 summarizes the frequency nadir, the equilibrium frequency deviation and the RoCoF for the three different renewable penetration rates.

Frequency response with different renewable penetration rate			
Penetration rate	$\mathbf{\Delta f_{nadir}}$ **[mHz]**	$\mathbf{\Delta f_{eq}}$ **[mHz]**	**RoCoF [mHz/s]**
Low (4%)	55	33	95
Medium (13%)	73	43	108
High (19%)	88	51	115

TABLE 5.20: Influence of the renewable penetration rate on the grid frequency response during an imbalance of 200 [MW]

It can be observed in TABLE 5.21 that the penetration rate of RES has an influence on the frequency nadir, the equilibrium frequency and the RoCoF. This confirms the hypothesis that the increased share of renewable energy sources in the energy mix deteriorates the stability in frequency.
In order to give substance to these simulation results, it is important to verify them with theoretical calculations. The equilibrium frequency and the RoCoF will be compared to the theoretical values in the following paragraphs.

Equilibrium frequency The equilibrium frequency is given by *Equation* 5.18

$$\Delta f = \frac{-\Delta P_c^0}{\dfrac{1}{f_0}\displaystyle\sum_{i=1}^{N}\frac{P_{Ni}}{S_i}} \tag{5.18}$$

With ΔP_c the change in load power consumption after connection of the additional load. Again, the effective power imbalance is different than the nominal power of the additional load because of the voltage drop.

Theoretical vs Real results for the equilibrium frequency			
	Theoretical	Real	
Penetration rate	$\mathbf{\Delta f_{eq}}$ $[\mathrm{mHz}]$	$\mathbf{\Delta f_{eq}}$ $[\mathrm{mHz}]$	**Error**[%]
Low (4%)	33	34.1	2.8
Medium (13%)	43	44.2	3.3
High (19%)	51	52.2	1.9

Table 5.21: Theoretical vs Real results of the equilibrium frequency with different values of penetration rate

It can be noticed that the theoretical results and the simulation results converge to the same values. It confirms the trend that a higher penetration rate leads to a higher equilibrium frequency deviation. It can be understood intuitively as there are less synchronous generators to participate in the droop control, since nuclear plants are partly replaced by RES with no droop algorithm.

Rate of Change of Frequency The theoretical RoCoF is given by *Equation* 5.19.

$$\text{RoCoF} = \left.\frac{df}{dt}\right|_{t_{imb}} = \frac{f_0\,\Delta P}{H_g\,P_N} \tag{5.19}$$

The grid inertia constant has to be calculated for each scenario of penetration rate. The effective power imbalance is used for the power imbalance term in the formula. Table 5.25 summarizes the theoretical and the simulation results for the RoCoF.

Theoretical vs Real results for the RoCoF				
		Theoretical	Real	
Penetration rate	$\mathbf{H_g}$ $[\mathrm{s}]$	**RoCoF** $[\mathrm{mHz/s}]$	**RoCoF** $[\mathrm{mHz/s}]$	**Error**[%]
Low (4%)	3.9	93	150	39
Medium (13%)	3.6	109	193	44
High (19%)	3.4	118	225	48

Table 5.22: Theoretical vs Real results of the RoCoF with different values of penetration rate

It can be seen that as the penetration rate increases, the grid inertia decreases. Moreover, a higher penetration rate of renewable leads to a higher RoCoF during an imbalance both in the theoretical results and the real results. This confirms the negative impact of a high penetration rate on the grid frequency response.
Then, the error between the theoretical results and the real results is higher than 35%. Potential reasons for this error are the time window of the RoCoF measurement and the rather simplistic theoretical formula.

Some conclusions The penetration rate in the Belgian grid is increasing as more and more renewable energies are being installed. During a power imbalance, a higher penetration rate leads to :

- An increase of the grid frequency nadir
- An increase of the equilibrium frequency deviation
- An increase of the RoCoF of the grid frequency

5.5.1 Impact of the VSG

The main goal behind the VSG is to support the grid frequency response as the share of renewable increases. In this section, we will determine if the VSG succeeds in improving the frequency response for various penetration rates. FIGURE 5.20 compares the grid frequency response due to a power imbalance of 200 [MW] with and without VSG.

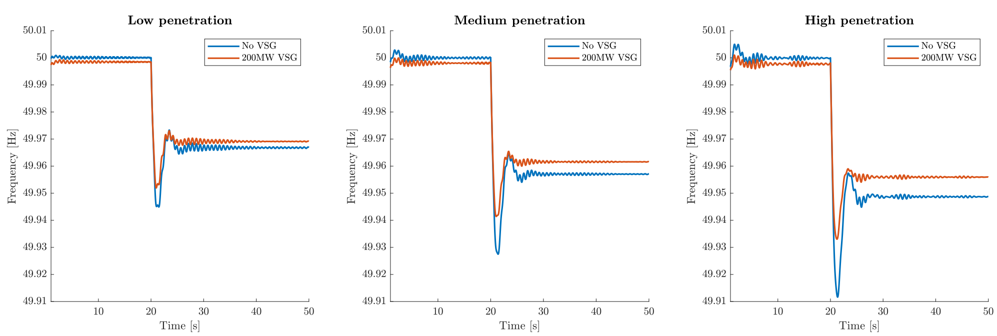

FIGURE 5.20: Influence of the VSG on the frequency response of the grid for several penetration rates

It can be seen that the VSG improves the frequency response of the grid as expected. Let us analyse the influence of the VSG on the frequency nadir, the equilibrium frequency and the RoCoF for several penetration rate.

Frequency nadir As seen in FIGURE 5.20, the VSG significantly reduces the frequency nadir during the power imbalance. TABLE 5.23 synthesises the values of the frequency nadirs with and without a VSG.

Frequency nadir with and without VSG			
	No VSG	200 [MW] VSG	
Penetration rate	$\mathbf{\Delta f_{nadir}}$ [mHz]	$\mathbf{\Delta f_{nadir}}$ [mHz]	**Reduction**[%]
Low (4%)	55	48	13
Medium (13%)	73	59	19
High (19%)	88	67	22

TABLE 5.23: Influence of the VSG on the grid frequency nadir during an imbalance of 200 [MW]

As seen in the table, the higher the penetration rate, the more the VSG reduces the frequency nadir. This can be explained by the proportionality between the power output of the VSG and the frequency deviation. *Equation* 5.20 describes the power output of the VSG:

$$P_{VSG} = K_D \Delta\omega + K_I \frac{d\Delta\omega}{dt} \tag{5.20}$$

As the frequency deviation increases, so does the power injection of the VSG in order to mitigate the frequency deviation. The VSG is thus efficient in reducing the frequency nadir of the grid.

Equilibrium frequency After analysing the frequency nadir, let us now take a look at the equilibrium frequency. TABLE 5.24 summarizes the values for the equilibrium frequency with and without VSG.

Equilibrium frequency with and without VSG			
	No VSG	200[MW] VSG	
Penetration rate	$\mathbf{\Delta f_{eq}}$ [mHz]	$\mathbf{\Delta f_{eq}}$ [mHz]	**Reduction**[%]
Low (4%)	33	31	7
Medium (13%)	43	38	10
High (19%)	51	44	14

TABLE 5.24: Influence of the VSG on the grid equilibrium frequency during an imbalance of 200 [MW]

As with the frequency nadir, the VSG is also more efficient at reducing the equilibrium frequency deviation when the penetration rate is high. We can compare these simulation results with a theoretical calculation using *Equation* 5.21.

$$\Delta f_{eq} = \frac{-\Delta P_c^0}{\frac{1}{f_0}\left(\sum_{i=1}^{N} \frac{P_{Ni}}{S_i} + \frac{P_{VSG,N}}{D}\right)} \tag{5.21}$$

Theoretical vs Real results for the equilibrium frequency with VSG			
	Theoretical	Real	
Penetration rate	$\Delta \mathbf{f_{eq}}$ [mHz]	$\Delta \mathbf{f_{eq}}$ [mHz]	Error[%]
Low (4%)	29	31	6.3
Medium (13%)	37	38	4.1
High (19%)	43	44	2.6

Table 5.25: Theoretical vs Real results of the influence of the 200 [MW] VSG on the equilibrium frequency with different values of penetration rate

The theoretical results and the simulations results for the impact of the VSG on the equilibrium frequency converge. As two different methods of calculation give the same results, these results are validated.

Rate of Change of Frequency The primary goal of the VSG is to provide virtual inertia to the grid as the penetration rate of renewable increases. Table 5.27 summarizes the impact of the VSG on the grid RoCoF for several penetration rates.

RoCoF with and without VSG			
	No VSG	200 [MW] VSG	
Penetration rate	RoCoF [mHz/s]	RoCoF [mHz/s]	Reduction[%]
Low (4%)	93	88	5.4
Medium (13%)	109	103	5.9
High (19%)	118	110	6.5

Table 5.26: Influence of the VSG on the RoCoF during an imbalance of 200 [MW]

It can be seen that the VSG is more efficient at reducing the RoCoF as the penetration rate increases. Indeed, it can be noticed that a fault in a grid with a high penetration rate and with VSG has the same RoCoF as in a grid with medium penetration rate without VSG. Thus the VSG is capable to provide virtual inertia to the grid and to mitigate the RoCoF during the first instants of the power imbalance. We can compare the results obtained by simulation with theoretical calculations using *Equation* 5.22.

$$\text{RoCoF} = \left.\frac{df}{dt}\right|_{t_{imb}} = \frac{f_0\,\Delta P}{H_g\,P_N} \tag{5.22}$$

RoCoF with and without VSG			
	Theoretical Reduction	Real Reduction	
Penetration rate	ΔRoCoF [mHz/s]	ΔRoCoF [mHz/s]	Error[%]
Low (4%)	5.8	5.0	14
Medium (13%)	8.2	6.4	21
High (19%)	10.2	7.7	24

TABLE 5.27: Influence of the VSG on the RoCoF during an imbalance of 200 [MW]

As seen in table, both the simulation results and the theoretical results show the same trend. Indeed, both methods show an increasing RoCoF reduction by the VSG as the penetration rate increases. This can be explained by the power output of the VSG shown in FIGURE 5.21.

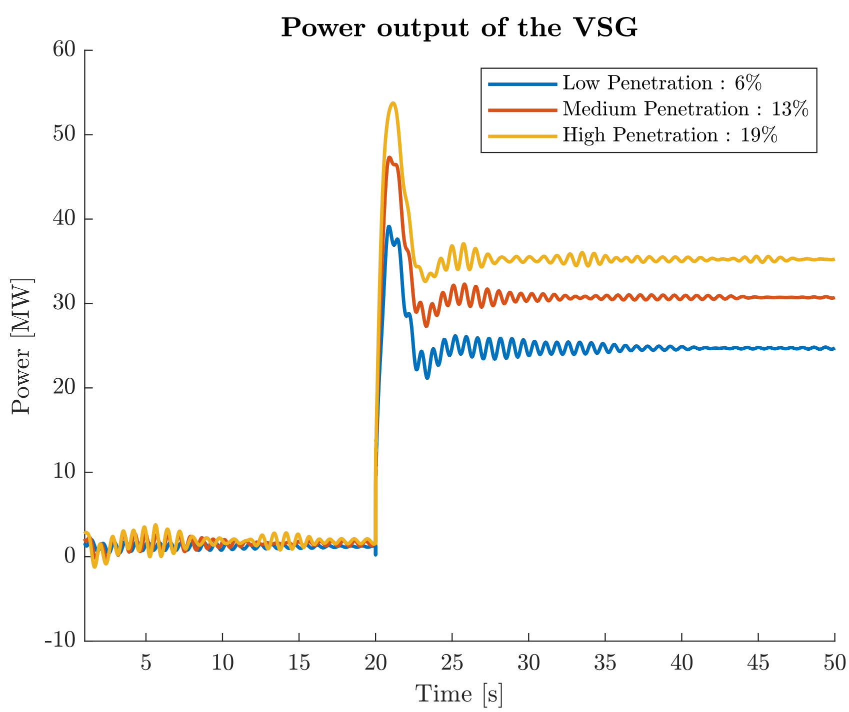

FIGURE 5.21: Output power of the VSG for an imbalance of 200 [MW] and several renewable penetration rate

A higher penetration rate means less grid inertia. Hence, the RoCoF of the grid frequency is higher and the VSG injects more power in order to mitigate the frequency deviation. This confirms the effectiveness of the VSG at creating virtual inertia to support the grid frequency.

Some conclusions In summary, the VSG succeeds at improving the frequency response of the grid as the penetration rate of renewable increases. In fact, as the penetration rate increases the VSG induces:

- A greater reduction of the frequency nadir
- A greater reduction of the equilibrium frequency
- A greater reduction of the RoCoF

Chapter 6

Economical analysis

6.1 Deloaded RES and storage

As analysed in the previous sections, it is possible to provide virtual inertia and primary frequency control to the grid using a VSG and an energy storage. This energy storage can be done with conventional installations as a BESS or with deloaded renewable energy sources (RES).

6.1.1 Deloaded renewables

Deloading a renewable energy source means operating it at a sub-optimum operating point. In other words, the RES does not operate at its MPP and will thus inject less than its maximum power into the grid [76]. As a result, the RES has a backup power it can release by shifting its operating point back to the MPP. This reserve of energy combined with the VSG will provide frequency stabilisation to the grid as the penetration rate of RES increases. Two different energy sources are studied to create a deloaded energy storage: PV panels and wind turbines.

Wind There are two control methods that can be used to deload the wind turbines: pitch control and rotor overspeed control [77].

Let us start with the pitch control. This control method involves maintaining the rotor speed constant and adapting the pitch angle of the wind turbines to control the power output. As shown in FIGURE 6.1, by increasing the pitch angle β above the optimal angle, the wind turbines will produce less power and thus have a back up available [78]. However, as the pitch control involves the command of a mechanical part with a large inertia, its response speed is slow and not suited for creating virtual inertia [76].

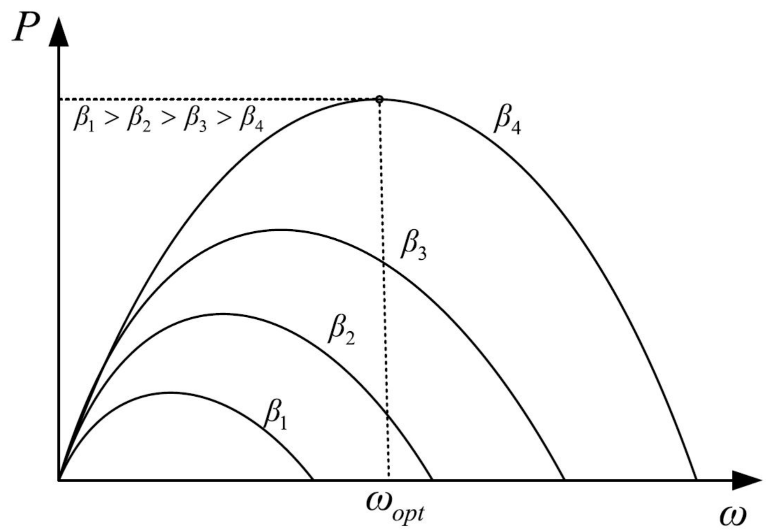

FIGURE 6.1: Power reserve with deloaded wind turbines based on pitch angle control [76].

Then, the power output of the wind turbines can be controlled with the the speed of the rotor. As shown in FIGURE 6.2, by increasing the rotor speed above the optimal speed, the wind turbine output power is decreased. Therefore, when the frequency in the grid drops, the wind turbine is able to inject more power in the grid by reducing the rotor speed back to the optimal speed [76]. The control of the rotor speed is fast and can react quickly enough to provide virtual inertia to the grid. Additionally, part of the energy lost by deloading the wind turbines is retained as kinetic energy due to the higher rotor speed [78].
Because of the faster response and smaller wind energy loss with the rotor overspeed control compared to the pitch control, this method is preferred.

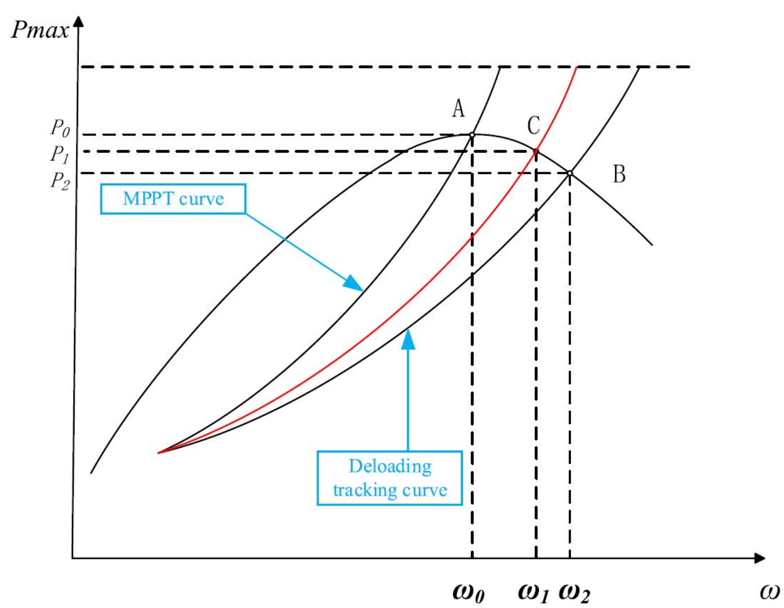

FIGURE 6.2: Power reserve with deloaded wind turbines based on rotor speed control [76].

PV Panels As with the wind turbines, the PV panels have a MPP. For a certain set of parameters (as solar irradiance, cell temperature, etc.), there is an optimal voltage of the PV panel at which it produces the maximum power. As shown in FIGURE 6.3, by operating the PV panels at a voltage higher than the optimal voltage, the output power of the PV panels is lowered and a reserve of power is available [79]. In case of power demand surge in the grid, the PV panels can quickly be brought back to its MPP by decreasing the voltage. This increases the power output of the PV panels and thus mitigate the frequency deviation.

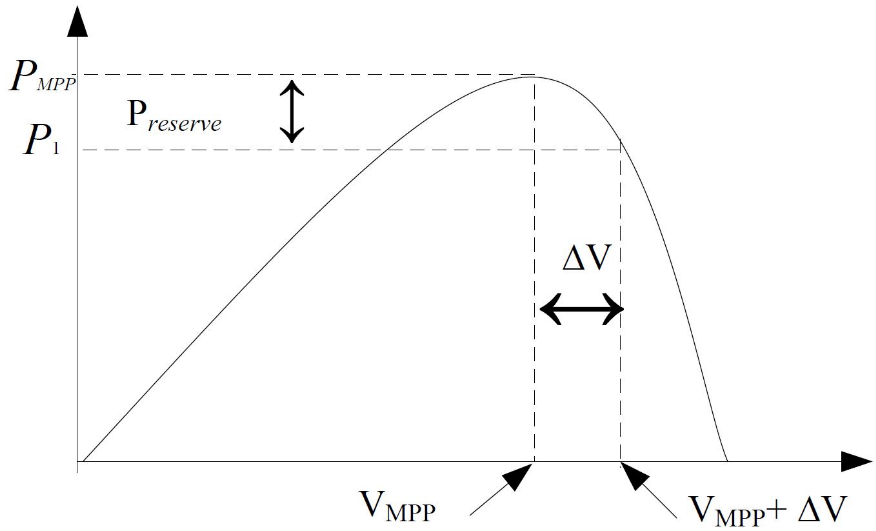

FIGURE 6.3: Power reserve using deloaded PV panels [80].

6.1.2 Battery Energy Storage System

Instead of deloading the renewable energy sources, an alternative is to operate them at their MPP and use a BESS for virtual inertia and primary frequency control. Hence, during over-injection of power in the grid, the excess of electricity is stored in the batteries and this energy is later released during peak demand periods to support the grid frequency [77][81]. BESS have a fast and precise regulation of their power output and are therefore well suited to provide virtual inertia and primary frequency control to the grid in combination with the VSG [82].

6.2 Economical Perspective

In SECTION 6.1.1, three different methods to create an energy reserve have been detailed. All of them have a power response fast enough to provide virtual inertia and primary frequency regulation to the grid when combined with the VSG.
Ancillary services are system services contracted by Elia to maintain frequency and voltage at appropriate levels [83]. As Elia does not operate the generators itself, it uses the flexibility of generation from electricity producers to ensure grid stability.
This case study aims to determine the competitiveness of ancillary services provided with BESS, deloaded wind turbines and deloaded PV panels from an economical perspective.

Case study The case study is done from the point of view of an energy producer operating a RES as wind farms or PV panels. The installed power capacity of RES is of a least 250 [MW] such that no more than 10% of the power capacity is deloaded.
The specifications of the storage units are: 25 [MW] power capacity for all storage devices and an energy storage of 25 [MWh] for the BESS (there is no limit on the energy reserve for deloaded wind or PV panels).
The power rating is chosen arbitrarily based on the 78 [MW] of primary frequency control capacity required by Elia for 2020 [84]. The battery storage specifications are chosen taking into account the power profile needed for virtual inertia and primary frequency control [85]. Indeed, the demand of power of these frequency regulations requires a fast power response of low duration. Moreover, the power capacity for balancing purposes has to be available 100% of the time during the hour when it is serviced [86]. Therefore, an energy reserve capable to service 1 hour at rated power is sufficient to cover the ancillary services applications covered in this thesis and is also the minimum storage to comply with Elia's rules [81][86].
Also, the hypothesis is made that the additional support of ancillary services through RES is only required between 10:00 am and 6:00 pm as the share of electricity produced with RES is the highest during this period [87] [88] [89]. During these 8 hours of servicing, it is estimated that the primary frequency response will operate on average 20 minutes at rated power each hour [81].
At first, the costs of storage for the different ancillary services will be compared using a common metric, the Levelized Cost Of Storage (LCOS) [81]. Then, the profitability of the different storage systems will be analysed with their Net Present Value (NPV). Finally, future outlooks on ancillary services with BESS and deloaded RES will be discussed.

6.2.1 Levelized cost of storage

The levelized cost of storage represents the total lifetime cost of a storage technology divided by its cumulative electricity supplied [90], as formulated in *Equation* 6.1.

$$\text{LCOS} = \frac{\text{Total lifetime cost}}{\text{Total supplied energy}} \left[\frac{€}{\text{MWh}}\right] \tag{6.1}$$

Let us compare the LCOS for the three storage methods: BESS, deloaded wind and deloaded PV panels.

Battery Energy Storage System The lifetime costs of a BESS can be classified in the following categories [91]:

- Investments costs (CAPEX)
- Operation and maintenance costs (O&M)
- Charging costs

The investments costs include the purchase of the power conversions system (PCS), the purchase of the battery modules, the engineering procurement costs and construction costs [92] [91]. Then operation and maintenance costs incorporate general maintenance of the BESS and PCS equipment, the augmentation costs of the BESS and the warranty costs for the BESS and PCS [92]. Next, the charging costs represent the cost of electricity stored in the BESS.

Charging costs thus depend on the price of the electricity used at the time when the BESS is charged. As the BESS is charged during times of excess generation in the grid, the BESS gets paid to absorb electricity from the grid. Therefore, the charging cost is negative and is in fact a source of revenue [81].

Taking into account the several costs of the BESS and the time value of money, *Equation* 6.1 becomes [90]:

$$\text{LCOS} = \frac{\text{CAPEX} + \sum_{t=1}^{N} \frac{\text{O\&M}}{(1+r)^t} + \sum_{t=1}^{N} \frac{\text{Charging costs}}{(1+r)^t}}{\sum_{t=1}^{N} \frac{\text{Electricity Discharged}}{(1+r)^t}} \tag{6.2}$$

The parameters summarized in TABLE 6.1 describe the operation of the BESS as frequency regulator:

Technical and Financial parameters of the BESS				
Parameter	**Symbol**	**Value**	**Unit**	**Remark**
Power	P	25	MW	For large wholesale applications [92]
Capacity	C	25	MWh	1 hour of servicing at rated power is enough to cover inertia and primary frequency regulation [81]
Cycles per year	CL	1145	Nr.	20 minutes at rated power per hour during the 8 hours of operation each day [81] .
Degradation per year	DF	1	%	Degradation of the capacity per year for 365 days of operation at 85% DoD[81].
Cycle efficiency	EF	90	%	96% charging and 94% discharging efficiency [77][81].
Depth of discharge	DoD	85	%	Lower DoD extends the lifetime of the battery [81].
Lifetime	N	10	years	Lifetime of 12000 cycles at 85% DoD [77][92]. Here the BESS has 1145 cycles/year.
Initial cost	/	420	€/kWh	Commercial Li-Ion battery system [81][93].
Total initial investment	CAPEX	10.5	M€	25MWh of BESS at 420 €/kWh.
Yearly O&M costs	O&M	0.21	M€	2% of the initial investment [81][93].
Discount rate	r	11	%	80% of equity at a 12% discount rate and 20% of debt at a 8% a discount rate [92] [93].
Down regulation tariffs	RT	-5	€/MWh	Down regulation tariffs paid for absorbing energy [94].
Escalation factor of electricity	ER	0.5	%	Additional to the annual inflation rate [81].

TABLE 6.1: Technical and financial parameters of a BESS for frequency regulation purposes

Equation 6.1 can be developed using the parameters shown in TABLE 6.1, it becomes [81]:

$$\text{LCOS} = \frac{\text{CAPEX} + \sum_{t=1}^{N} \frac{\text{O\&M}}{(1+r)^t} + \sum_{t=1}^{N} \frac{\text{RT} \cdot \text{CL} \cdot \text{C} \cdot \text{DoD} \cdot (\text{1-DF})^t \cdot (\text{1+ER})^t}{(1+r)^t}}{\sum_{t=1}^{N} \frac{\text{CL} \cdot \text{C} \cdot \text{DoD} \cdot \text{EF} \cdot (\text{1-DF})^t}{(1+r)^t}} \tag{6.3}$$

The analysis is done on a 10 year period which is the lifetime of the BESS investment. By replacing the parameters in *Equation* 6.3 with the values given in TABLE 6.1 we obtain:

$$LCOS = 90 \left[\frac{€}{\text{MWh}}\right]$$

Deloaded Wind Turbines There are no additional costs when operating a wind farm or PV panels at a reduced power output but there is a loss in operating revenues [77]. The operational loss of revenue occurs during the period when the RES are deloaded. As a reminder, the ancillary services using RES are only required for an 8 hour period during the day. Therefore, the loss of operating revenues due to the deloading of RES can be represented by the energy loss during this period multiplied by the average electricity price on this same period [81].
Moreover, the deloaded RES has to be compared with the BESS with an equal capacity reserve and thus 25 [MW] of active power capacity will be deloaded. For example, if the off-shore wind farms with 1.7 [GW] of capacity are producing 1 [GW] of electricity at a certain moment, after being deloaded they will be injecting only 975 [MW] into the grid. To summarize, the deloaded capacity is subtracted from the active power production and not from the installed capacity of RES.
Then, it is assumed that the deloaded RES injects the same amount of energy per day in the grid as the BESS because it fulfills the same ancillary services.
Equation 6.4 shows the LCOS for deloaded wind turbines taking into account the operational losses of revenues.

$$\text{LCOS} = \frac{\sum_{t=1}^{N} \frac{\text{Revenue Losses}}{(1+r)^t}}{\sum_{t=1}^{N} \frac{\text{Electricity Discharged}}{(1+r)^t}} \tag{6.4}$$

As the wind turbines operate in deloaded mode for 8 hours per day, *Equation* 6.4 can be developed in *Equation* 6.5.

$$\text{LCOS} = \frac{\sum_{t=1}^{N} \frac{\text{TF} \cdot \text{C} \cdot \text{DH} \cdot (1+\text{ER})^t}{(1+r)^t}}{\sum_{t=1}^{N} \frac{\text{CL} \cdot \text{C} \cdot \text{DoD} \cdot \text{EF}}{(1+r)^t}} \tag{6.5}$$

Parameters of the Deloaded Wind				
Symbol	**Meaning**	**Value**	**Units**	Remark
TF	Electricity Tariff	40	€/MWh	Average day-ahead price during the day [95]
C	Deloaded capacity	25	MW	Same deloaded power as the BESS
DH	Deloaded hours per year	2920	hours	Deloaded during 8 hours per the day
ER	Electricity escalation rate	0.5	%	/
r	discount rate	11	%	/

TABLE 6.2: Parameters for the LCOS calculation of a deloaded wind turbine

It can be seen from TABLE 6.1 and TABLE 6.2 that the electricity tariffs are different. Indeed, the BESS recharges during down regulation demand from Elia when the prices of electricity are negative. On the contrary, the wind turbines are always deloaded during the day to provide ancillary services which results in a loss of revenues.
Then, the energy released for primary frequency support by the deloaded wind is the same as the energy released by the BESS except for the degradation factor that does not occur with the wind turbines.

By replacing the values given in TABLE 6.2 in *Equation* 6.5, we obtain:

$$\text{LCOS} = 143 \left[\frac{€}{\text{MWh}}\right]$$

Deloaded PV Panels The deloaded PV panels will have the same LCOS as the deloaded wind turbines. Indeed, if the same capacity of PV panels is deloaded for the same duration as the wind turbines, they will experience the same loss of revenues from electricity sales. As there are no additional operating costs for deloading PV panels or wind turbines, the LCOS for the two RES will be the same.
Therefore, the LCOS of deloaded PV panels is equal to the LCOS of deloaded wind and is given by *Equation* 6.6.

$$\text{LCOS} = \frac{\sum_{t=1}^{N} \frac{\text{Revenue Losses}}{(1+r)^t}}{\sum_{t=1}^{N} \frac{\text{Electricity Discharged}}{(1+r)^t}} = 143 \left[\frac{€}{\text{MWh}}\right] \tag{6.6}$$

It can be seen that the LCOS is lower for the BESS than for deloaded wind turbines or deloaded PV panels. This means that deloading the RES is a more expensive alternative to store electricity for frequency regulation than operating the RES at MPP in combination with a BESS.
This difference in LCOS is mainly due to the additional revenue stream from charging the BESS compared to the revenue loss for energy reserve with the deloaded RES. Indeed, if the BESS would pay the average electricity price for its electricity storage (40 €/MWh), the LCOS for deloaded RES and the BESS would become nearly equal.

Sensitivity analysis Several assumptions were made in order to obtain the LCOS for the BESS and deloaded RES. This paragraph will analyse the influence of each parameter on the LCOS to understand if a small estimation error could change the LCOS significantly.
FIGURE 6.4 shows the sensitivity of several parameters of the BESS on the LCOS.

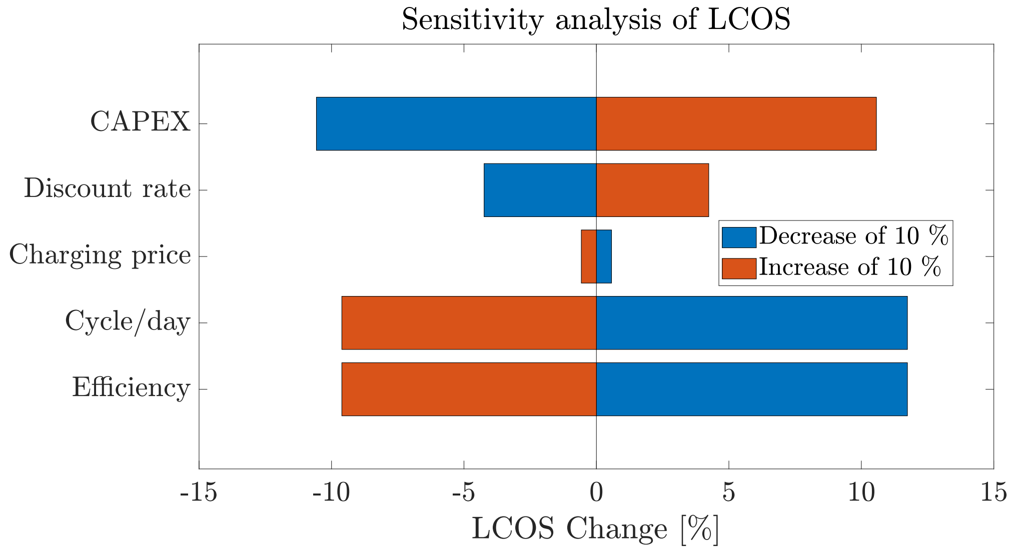

FIGURE 6.4: Sensitivity analysis of the LCOS for the BESS

It can be seen that the CAPEX, the efficiency of the BESS and the number of cycle per day have the most influence on the LCOS. Actually a 50% increase of the CAPEX would be required in order to have the same LCOS for the BESS as for deloaded RES.
As for the efficiency, even with a 60% cycle efficiency of the batteries, the BESS stays less costly than the deloaded RES.
Finally, an increase of the number of cycles per day would lead to a reduced lifetime of the BESS and thus to an increase of the CAPEX due to higher renewal of equipment.
Then, a sensitivity analysis was also done to determine the influence of the parameters of the deloaded RES on the LCOS.
FIGURE 6.5 shows the influence of several parameters on the LCOS for deloaded RES.

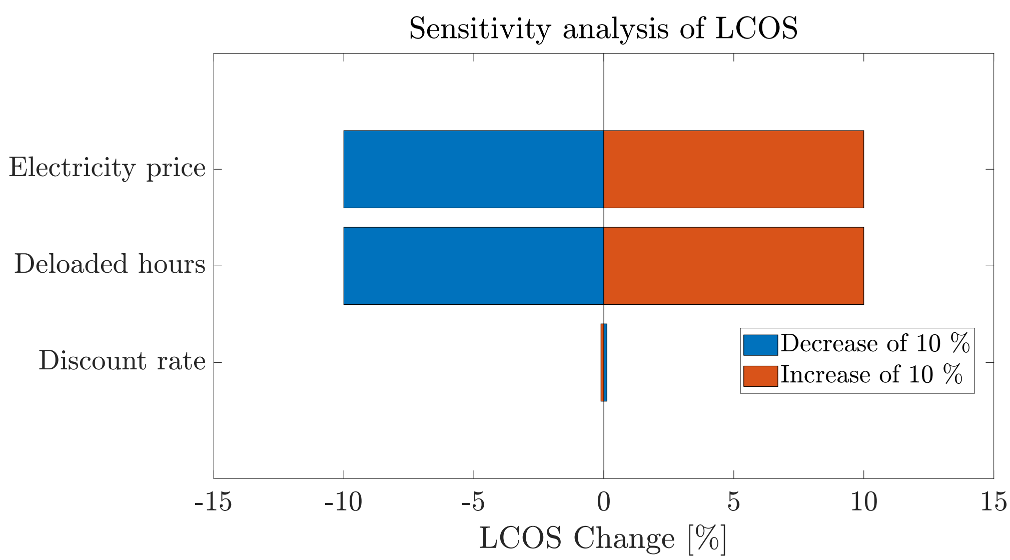

FIGURE 6.5: Sensitivity analysis of the LCOS for deloaded RES

The two parameters with the most influence are the electricity price and the deloaded hours. A 40% decrease in the average electricity price to 24 €/MWh would be required in order to

make the costs of storage less expensive with the deloaded RES than with the BESS.
Then, the number of deloaded hours also have a significant impact on the LCOS. The deloaded RES would benefit from a shorter but more intense period of activity.

6.2.2 Net present value

To understand the profitability of the ancillary services provided with the BESS and with deloaded RES, the Net Present Value (NPV) will be calculated. The Net Present Value takes into account both the revenues and costs associated with ancillary services and is determined by *Equation* 6.7.

$$NPV_{profit} = NPV_{revenues} - NPV_{costs} \tag{6.7}$$

With:

$$NPV_{revenues} = \sum_{t=1}^{N} \frac{\text{Revenue(t)}}{(1+r)^t}$$

$$NPV_{costs} = \sum_{t=1}^{N} \frac{\text{Cost(t)}}{(1+r)^t}$$

The costs have been calculated in the previous section and are represented by the numerator of the LCOS formula. The revenues from ancillary services have still to be determined.

Costs Let us start with the cost as most of the calculation has already been done for the LCOS. These costs are different for the BESS and the deloaded RES.
The NPV of the costs of the BESS are given by *Equation* 6.8.

$$NPV_{Costs} = \text{CAPEX} + \sum_{t=1}^{N} \frac{\text{O\&M}}{(1+r)^t} + \sum_{t=1}^{N} \frac{\text{Charging costs}}{(1+r)^t} = -11.1 \text{ M€} \tag{6.8}$$

Then, the NPV of the costs of deloaded wind and deloaded PV panels is given by *Equation* 6.9.

$$NPV_{Costs} = \sum_{t=1}^{N} \frac{\text{Revenue Losses}}{(1+r)^t} = -17.6 \text{ M€} \tag{6.9}$$

The costs for the BESS are significantly lower than the costs of deloaded wind or PV panels. As explained before, this difference is driven by the high loss in electricity sales revenues with deloaded RES which do not occur with the BESS.

Revenues The second component of the profitability estimations are the revenues from ancillary services. The distribution of the balancing capacity for primary frequency response in Belgium is done through a system of auction where Elia pays producers per MW of reserve capacity provided during one hour [98]. This power has be available for 100% of the hour contracted by Elia [86]. The average price for one MW of balancing capacity contracted during one hour by Elia is 8 €/MW/h [98].
On top of these revenues from power reserve, the producers are paid for each MWh of electricity they inject in the grid during primary frequency control [99]. The average up-regulation electricity price is in average 50 €/MWh and is thus higher than the day-ahead electricity

price [94].
Concerning the revenues from virtual inertia, there is no existing market for them in Belgium yet. Hence, they can not be included in the revenue analysis. However, an estimate of the minimum viable price for virtual inertia will be given in SECTION 6.3.
TABLE 6.3 summarizes the parameters for the ancillary service revenues calculation.

Parameters for ancillary services revenues				
Symbol	**Meaning**	**Value**	**Units**	Remark
TF_{cap}	Reserve capacity tariffs	8	€/MWh/h	Average auction price for capacity reserve [98].
TF_{up}	Up-regulation tariffs	50	€/MWh	Average electricity price for up-regulation [94]
P	Balancing capacity	25	MW	Nominal power of the BESS and deloaded wind
T	Yearly balancing	2920	hours	Balancing required from RES during 8 hours/day.
ED	Yearly electricity discharged	21 900	MWh	20 minutes at rated power per hour of servicing.
r	discount rate	11	%	/

TABLE 6.3: Parameters for the revenues calculation of a deloaded RES and BESS

The revenues from ancillary services are thus composed from a fixed capacity revenue and from a variable revenue proportional to the amount of power injected during frequency up-regulation. This revenue can be calculated with *Equation* 6.10 [99]:

$$NPV_{Revenue} = \sum_{t=1}^{N} \frac{Revenue(t)}{(1+r)^t} = \sum_{t=1}^{N} \frac{TF_{cap} \cdot P \cdot T}{(1+r)^t} + \sum_{t=1}^{N} \frac{TF_{up} \cdot ED}{(1+r)^t} \tag{6.10}$$

By replacing the parameters from TABLE 6.3 in *Equation* 6.10, we obtain NPV of the revenues from ancillary services on a 10 year basis:

$$NPV_{Revenues} = 3.5 \text{ M€} + 6.4 \text{ M€} = 9.9 \text{ M€} \tag{6.11}$$

The revenues from the ancillary services provided by the BESS and deloaded RES are equal as they all provide 25MW of capacity during 8 hours per day and the same amount of up-regulation electricity.

Profitability Now that the revenues and costs for the BESS and deloaded RES are known, we can estimate the profitability of both systems.
Using *Equation* 6.7 and the values for the revenues and costs calculated previously, we obtain :

$$NPV_{BESS} = -1.2 \text{ M€}$$

$$NPV_{Wind} = NPV_{PV} = -7.7 \text{ M€}$$

As the NPV for both projects is negative, they are not profitable and should not been undertaken. Subsidies or higher tariffs for the ancillary services are required in order to make these projects economically viable.
The producers have no incentives to participate to the frequency regulation and will thus produce electricity at maximum power output.

6.3 Future outlook

So that energy producers are willing to provide ancillary services, these services have to be profitable. Until now, there is no market for virtual inertia in Belgium and the revenues from primary frequency control are too small to cover the costs of the electricity producers as demonstrated in SECTION 6.2.2.
For virtual inertia, power injection has to act fast and it lasts less than 1 second. Therefore, a remuneration for virtual inertia services per MW of capacity installed seems more logical than a remuneration per MWh of electricity injected in the grid. Let us calculate the minimum virtual inertia tariffs for the BESS and deloaded RES so that the VSG would be profitable. The virtual inertia tariff would have to be paid on top of the primary frequency control tariff.
The virtual inertia tariffs per MW serviced each hour such that the NPV of the BESS with VSG equals zero is:

$$TF_{inertia} = 3 \left[\frac{€}{\text{MW h}}\right]$$

The virtual inertia tariffs per MW serviced each hour such that the NPV of the deloaded RES with VSG equals zero is:

$$TF_{inertia} = 10 \left[\frac{€}{\text{MW h}}\right]$$

The minimum price for virtual inertia capacity with the BESS such that the installation is profitable is significantly lower than the price of capacity for primary frequency control. Therefore, this technology has the potential to provide virtual inertia to the grid at a low cost for the Transmission System Operator (Elia).
For deloaded RES, the minimum price for virtual inertia is higher than the current capacity price for primary frequency control which makes it unlikely to be a profitable alternative in the near future.

6.4 Conclusion

As a conclusion, it was determined that ancillary services with BESS and deloaded RES are not profitable yet compared to the operation of RES at maximal power output without providing frequency control. Also, a sensitivity analysis was done to understand to most influential parameters in the cost structure of the BESS and deloaded RES.
Finally, an estimation of the minimum price for virtual inertia services has been calculated such that ancillary services with the VSG would be profitable. The BESS will become economically viable for ancillary services if the price of virtual inertia is above 3 €/MW/h.

Chapter 7

Future outlook and conclusion

7.1 Future outlook

The modelling of the grid as described in Chapter 4 allowed us to study the grid inertial behaviour in term of RoCoF, frequency nadir and equilibrium frequency. The simplifications made for the power generation, the different control systems and the downstream grid were useful to reduce drastically the computational time while keeping a logical and consistent frequency behaviour. However, the modelled network is not flawless and some features can be added to enhance the results accuracy for further work.

As seen during the simulation results analysis, the frequency dynamics of the grid are strongly dependent on the voltage profile. Indeed, the inertial response of the grid mainly depends on the power imbalance, as seen in the swing equation. The simulation results highlighted that the power imbalance is different from the theoretical expectation. Due to the connection of a new load or to the loss of generator, the voltage profile decreases in the grid. Because of the constant impedance load modelling, the power consumption in the grid also varies. This effect reduces the theoretical value of power imbalance to a smaller effective value. Although it seems logical that voltage has influence on the power consumption of the loads (due to the $\left(\frac{V}{V_0}\right)^{\alpha}$ term in the expression of power), this dependency is disproportionate in the grid model. This is due to two reasons :

- **Constant impedance assumption:** this assumption implies a power variation proportional to the square of voltage variation ($\alpha = 2$). As explained in Section 4.4, more realistic values of α should lie between $\alpha = 0$ and $\alpha = 1$, causing a much lower voltage dependency. Moreover, the dispersed generation provides power from downstream and also influences the power flows.

- **Voltage regulation:** a strong hypothesis made for the thesis is that the voltage variation would not impact the frequency dynamics. This assumption appeared not to be valid regarding the simulation results. In this thesis, no voltage regulation devices or SM excitation systems were modelled. For further work, it would be useful to integrate these regulation systems in order to model a more realistic voltage profile with less dependency on load connections.

Moreover, the aim of this thesis was to study the impact of the VSG on the inertial response of the grid by focusing on initial RoCoF and frequency nadir. The results analysis focused on the tendencies and on the reduction in %, not on the exact values. However, if future studies whose goal is to look at Grid Code compliance (i.e verifying that the frequency lies in the imposed frequency range) are made using the thesis grid model, it would be convenient to use the detailed model of SM instead of the simplified one used in this thesis . Indeed, the simplified model underestimates the frequency nadir. The simulations results are not precise enough in terms of frequency values to predict if the frequency nadir lies in the acceptable range.

Another aspect that was not covered in this thesis and that influences the inertial response of the VSG is the power rate limiter. Indeed, the rate of power injection during the very first instants after a power imbalance is determinant and strongly influences the VSG inertial response. However, there is a current limitation for the power electronics in order not to introduce an overload causing damages on the inverter. For further work, a more detailed model for power electronics would allow to emulate a more realistic power injection resulting in a more accurate inertial behaviour.

Finally, further improvements can be done in the economical analysis. Indeed, the profitability of the deloaded RES was done with the hypothesis that they are constantly deloaded during their servicing period for ancillary services. However, optimisation algorithms have been developed to reduce the deloading period of the RES which leads to a smaller loss in electricity revenues for the producer of electricity. It would be interesting to see if an economical analysis taking these new deloading algorithms into account would have a different conclusion.

7.2 Conclusion

As the share of RES increases, the grid inertia is reduced which causes greater frequency deviations and undesired tripping of RoCoF relays. This thesis has extensively covered the Virtual Synchronous Generator technology and its ability to provide frequency support to the grid.

First, a synthetic review of the various technologies capable to provide virtual inertia was performed. The control algorithms of the synchronverters, swing equation based, VSG and droop-based model were studied and their respective advantages and drawbacks were compared. The VSG was selected as best topology for this thesis as its advantages are the most relevant for the study of the BHVG inertia. Indeed, it has a similar inertial behaviour as SM which makes it more intuitively understandable than other topologies. In addition, the VSG provides over-current protection as it is current-controlled. Next to its relevant advantages, the VSG drawbacks have little influence when considering the BHVG. Indeed, the VSG is not suited for islanded operation and can experience PLL instabilities in weak grids. These drawbacks are irrelevant in this thesis as the BHVG is never islanded and is considered a strong grid.

Then, the followed theoretical approach to model the VSG was thoroughly explained. The different coordinate systems were explained as well as the current control of the inverter with the direct and quadrature components. The choice of droop and inertia constants was justified and their influence on the grid frequency was intuitively explained.

Thereafter the modelling of the BHVG was detailed. More precisely, the grid model contains all Belgian generators with a nominal power above 350 [MW] as well as the cross-borders power links with France and the Netherlands. The Belgian nuclear, gas and hydro power plants were represented with an equivalent synchronous machine of adequate inertia and droop time constant. The power injection from off-shore wind farms was replicated using a constant power injection source. Concerning the overhead power lines of the grid, they were reproduced using a purely inductive impedance. Also, a model of the downstream grid taking into account the frequency dependency of the loads was presented.

Afterwards, simulations on the BHVG were conducted. A parametric analysis was performed showing the influence of the droop and inertia constants. Also, it was demonstrated that the VSG is more efficient at reducing the frequency deviation if it is located closer to the fault. Then it was showed that the frequency dependency of the downstream grid has little influence on the frequency results and could therefore be neglected. To continue, the differences in frequency response between the connection of a load and the loss of a generator were investigated. In fact, the connection of an additional load creates a larger frequency deviation because it leads to a smaller voltage drop. Finally, it was shown that the VSG is efficient in supporting the grid frequency response as the penetration rate of RES increases which was the main purpose of this thesis. Indeed, in a high penetration rate scenario, a 200 [MW] VSG is capable of reducing the RoCoF by nearly 8% during a 200[MW] power imbalance. It was also shown that the VSG is increasingly efficient in providing frequency regulation as the penetration rate of RES increased.

Finally, an economical analysis of the various energy storage combined with the VSG was done.

Both the Levelized Cost of Storage and the Net Present Value were calculated for a BESS and deloaded RES. The results showed that the BESS is a cheaper technology than deloading RES in order to provide ancillary services to the grid. However, both the BESS and deloaded RES are not profitable at the moment to deliver virtual inertia and primary frequency control. For the moment, there is no market for virtual inertia in Belgium nor infrastructure capable to provide it. It was estimated that a minimum price of 3 €/MW/h for virtual inertia capacity was necessary to make ancillary services with the BESS profitable for electricity producers. In conclusion, further developments of regulations and remuneration schemes are required for the integration of Virtual Inertia in the European electricity grid.

Appendix A: Downstream grid load distribution

Loads distribution	
Location	**Power [MW]**
Achene	1000
Aubange	1000
Avelgem	1000
Bruegel	1000
Brume	500
Buggenhout	500
Champion	500
Courcelles	500
Gramme	1000
Horta	500
Lixhe	500
Massenhoven	1000
Meerhout	1000
Mekingen	500
Mercator	1000
Van Eyck	1000

Appendix B: Simulink Network

SIMULINK representation of Belgian High Voltage Grid

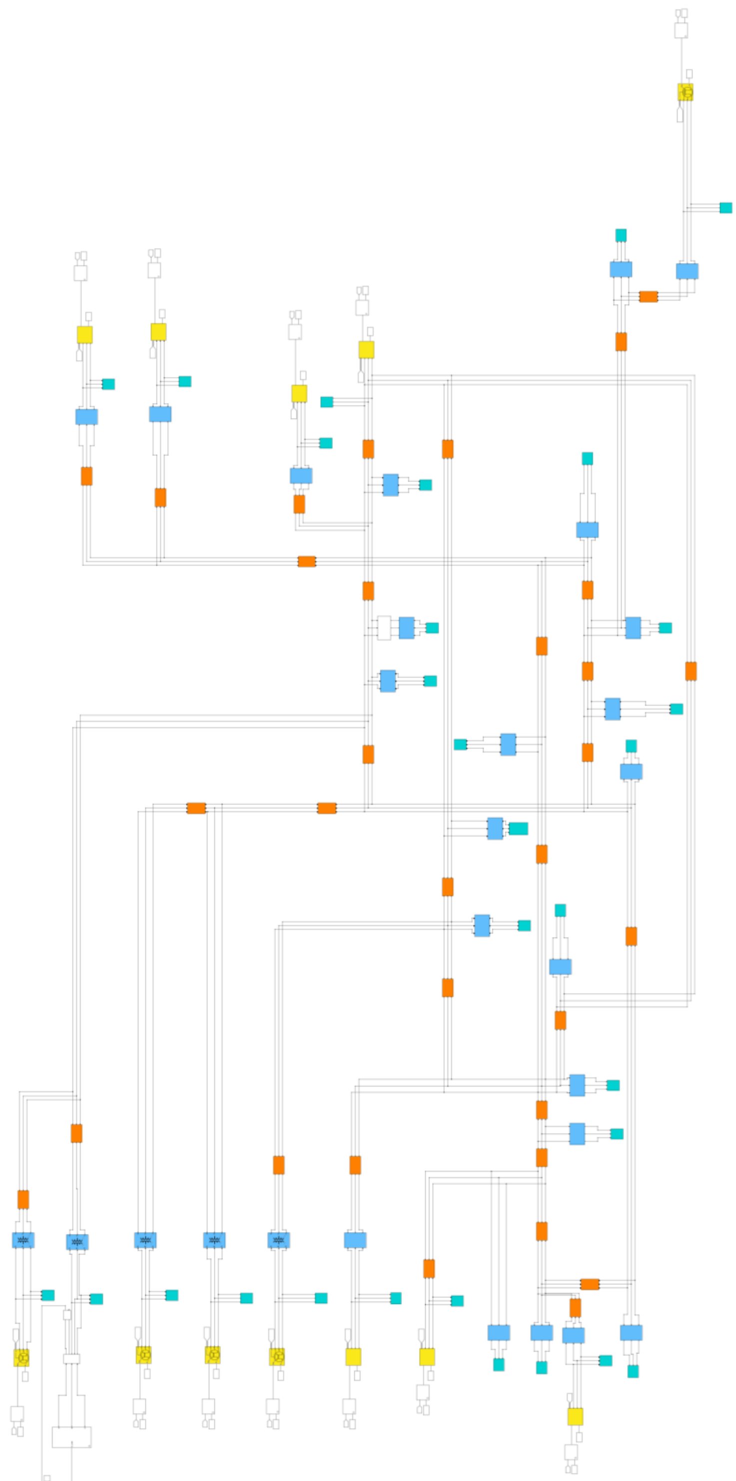

Appendix C: Simulink Virtual Synchronous Generator

SIMULINK representation of Virtual Synchronous Generator

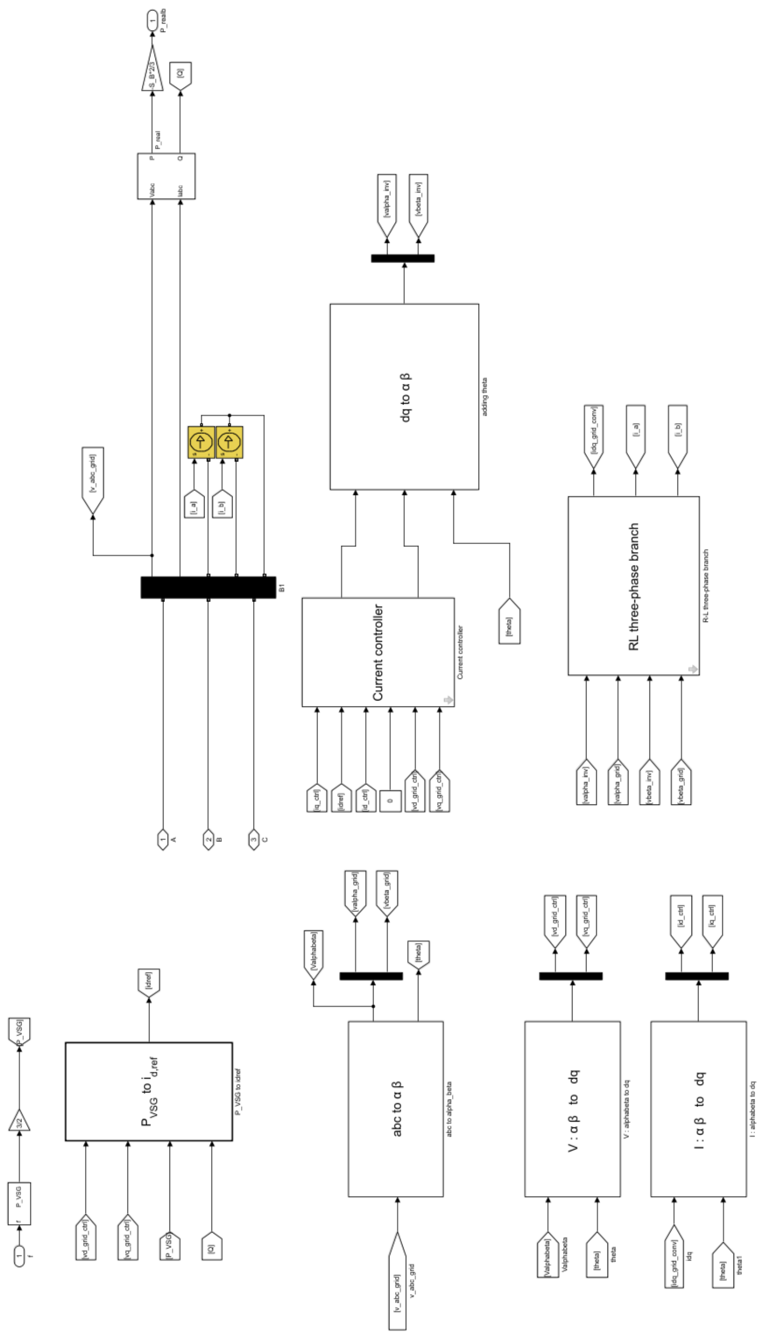

Bibliography

[1] **Association pour la Promotion des Energies Renouvelables**, "*Observatoire belge des énergies renouvelables, Production d'Energie Renouvelable*", `http://www.apere.org/fr/observatoire-energies-renouvelables`, [Online, Accessed 28 May 2020]

[2] **Ujjwol Tamrakar , Dipesh Shrestha, Manisha Maharjan, Bishnu P. Bhattarai, Timothy M. Hansen & Reinaldo Tonkoski**. (26 June 2017). "*Virtual Inertia: Current Trends and Future Directions*." Applied Science.

[3] **S. Roaf, D. Crichton, et F. Nicol**, " *Chapter 14 - Fuel Security: When Will the Lights Go Out?* ", in Adapting Buildings and Cities for Climate Change (Second Edition), Second Edition., S. Roaf, D. Crichton, et F. Nicol, Éd. Oxford: Architectural Press, 2010, p. 289-312.

[4] **P. Pourbeik, S. Soni, A. Gaikwad, et V. Chadliev**, " *Providing Primary Frequency Response from Photovoltaic Power Plants* ", 2017.

[5] **B. Hartmann, I. Vokony, et I. Táczi**, " *Effects of decreasing synchronous inertia on power system dynamics—Overview of recent experiences and marketisation of services* ", Int Trans Electr Energ Syst, vol. 29, n 12, déc. 2019

[6] **A. Dixon**, "*Modern Aspects of Power System Frequency Stability and Control*". Elsevier Science, 2019.

[7] **Western Power Distribution**, " *Loss of Mains Protection* ", Distribution System Operability Framework, June 2018.

[8] **M. R. Almassalkhi et I. A. Hiskens**, " *Impact of Energy Storage on Cascade Mitigation in Multi-Energy Systems* ", in Energy Storage for Smart Grids, Elsevier, 2015, p. 115-169.

[9] **Y. R. Omar, I. Z. Abidin, S. Yusof, H. Hashim, et H. A. A. Rashid**, " *Under frequency load shedding (UFLS): Principles and implementation* ", in 2010 IEEE International Conference on Power and Energy, Kuala Lumpur, Malaysia, nov. 2010, p. 414-419

[10] **Energuide, a Sibelga Initiative**, " *Why does the electricity grid have to stay in balance?* ", `https://www.energuide.be/en/questions-answers/why-does-the-electricity-grid-have-to-stay-in-balance/2136` [Online, Accessed 29 May 2020].

[11] **H. Beck and R. Hesse**, "*Virtual synchronous machine*", 2007 9th International Conference on Electrical Power Quality and Utilisation, Barcelona, 2007, pp. 1-6

[12] **I. Vokony**, "*Effect of inertia deficit on power system stability - synthetic inertia concepts analysis*," 2017 6th International Youth Conference on Energy (IYCE), Budapest, 2017, pp. 1-6

[13] **E. De Jaeger**, "*LELEC2520 - Electric Energy Systems*" Course Notes, "*Load-Frequency Control*", UCLouvain, 2020.

[14] **Zhong, Q.-C.** (2016). "*Virtual Synchronous Machines: A unified interface for grid integration*". IEEE Power Electronics Magazine

[15] **Piya, P., & Karimi-Ghartemani, M.** (2016). "*A stability analysis and efficiency improvement of synchronverter*". 2016 IEEE Applied Power Electronics Conference and Exposition (APEC), 3165-3171.

[16] **H. M. A. Antunes, S. M. Silva, D. I. Brandao, A. A. P. Machado, et R. V. Ferreira**, " *A fault-tolerant grid-forming converter applied to AC microgrids*", International Journal of Electrical Power Energy Systems, vol. 121, p. 106072, 2020

[17] **Z. Li, C. Zang, P. Zeng, H. Yu, S. Li and J. Bian**, "*Control of a Grid-Forming Inverter Based on Sliding-Mode and Mixed H_2/H_∞ Control,*" in IEEE Transactions on Industrial Electronics, vol. 64, no. 5, pp. 3862-3872, May 2017

[18] **B. Hoseinzadeh et F. Blaabjerg**, "*Pre-design feasibility study of grid connected wind pow er plants under weak grid condition*", Electric Power Systems Research, vol. 182, p. 106248, 2020

[19] **Wang, S., Hu, J., Yuan, X.** (2015). "*Virtual Synchronous Control for Grid-Connected DFIG-Based Wind Turbines*". IEEE Journal of Emerging and Selected Topics in Power Electronics, 3(4), 932-944.

[20] **Shinnaka, S**. (2008). "*A Robust Single-Phase PLL System With Stable and Fast Tracking*". IEEE Transactions on Industry Applications, 44(2), 624-633.

[21] **X. Zhang, D. Xia, Z. Fu, G. Wang and D. Xu**, "*An Improved Feedforward Control Method Considering PLL Dynamics to Improve Weak Grid Stability of Grid-Connected Inverters,*" in IEEE Transactions on Industry Applications, vol. 54, no. 5, pp. 5143-5151, Sept.-Oct. 2018

[22] **Zhong, Q.-C., Nguyen, P.-L., Ma, Z., Sheng, W.** (2014). "*Self-Synchronized Synchronverters: Inverters Without a Dedicated Synchronization Unit*" . IEEE Transactions on Power Electronics, 29(2), 617-630.

[23] S**akimoto, K., Miura, Y., Ise, T.** (2015). *"Characteristics of Parallel Operation of Inverter-Type Distributed Generators Operated by a Virtual Synchronous Generator*". Electrical Engineering in Japan, 192(4), 9-19.

[24] **J. Alipoor, Y. Miura, et T. Ise**, " *Power System Stabilization Using Virtual Synchronous Generator With Alternating Moment of Inertia* ", IEEE Journal of Emerging and Selected Topics in Power Electronics, vol. 3, n 2, p. 451-458, juin 2015

[25] **J. Meng, Y. Wang, C. Fu and H. Wang**, "*Adaptive virtual inertia control of distributed generator for dynamic frequency support in microgrid,*" 2016 IEEE Energy Conversion Congress and Exposition (ECCE), Milwaukee, WI, 2016, pp. 1-5

[26] **Yalong Hu1, Wei Wei & Yonggang Peng & Jinyong Lei**. (27 July 2016). "*Fuzzy virtual inertia control for virtual synchronous generator*". Proceedings of the 35th Chinese Control Conference.

[27] **Hassan Bevrani, Toshifumi Ise & Yushi Miura**. (13 July 2013). "*Virtual synchronous generators: A survey and new perspectives*". Science Direct.

[28] **S. D'Arco and J. A. Suul**, "*Equivalence of Virtual Synchronous Machines and Frequency-Droops for Converter-Based MicroGrids*", in IEEE Transactions on Smart Grid, vol. 5, no. 1, pp. 394-395, Jan. 2014.

[29] **Y. Du, J. M. Guerrero, L. Chang, J. Su and M. Mao**, "*Modeling, analysis, and design of a frequency-droop-based virtual synchronous generator for microgrid applications*", 2013 IEEE ECCE Asia Downunder, Melbourne, VIC, 2013, pp. 643-649.

[30] **S. D'Arco and J. A. Suul**, "*Virtual synchronous machines — Classification of implementations and analysis of equivalence to droop controllers for microgrids*", 2013 IEEE Grenoble Conference, Grenoble, 2013, pp. 1-7.

[31] **S. D'Arco and J. A. Suul**, "*Equivalence of Virtual Synchronous Machines and Frequency-Droops for Converter-Based MicroGrids*", in IEEE Transactions on Smart Grid, vol. 5, no. 1, pp. 394-395, Jan. 2014.

[32] **V. Soares, P. Verdelho and G. Marques**, "*Active power filter control circuit based on the instantaneous active and reactive current i/sub d/-i/sub q/ method*", PESC97. Record 28th Annual IEEE Power Electronics Specialists Conference. Formerly Power Conditioning Specialists Conference 1970-71. Power Processing and Electronic Specialists Conference 1972, Saint Louis, MO, USA, 1997, pp. 1096-1101 vol.2.

[33] **R. Hesse, D. Turschner, et H.-P. Beck**, "*Micro grid stabilization using the virtual synchronous machine (VISMA)*", REPQJ, vol. 1, n 07, p. 676-681, avr. 2009

[34] **F.N.J Martin**, "*Virtual Synchronous Machine*", Tecnico Lisboa, ULisboa `https://fenix.tecnico.ulisboa.pt/downloadFile/395145918861/paper.pdf`, [Online, Accesed XX March 2020] .

[35] **Y. Chen, R. Hesse, D. Turschner, et H.-P. Beck**, "*Comparison of methods for implementing virtual synchronous machine on inverters*", REPQJ, p. 734-739, avr. 2012

[36] **P. Rodriguez, I. Candela, et A. Luna**, "*Control of PV generation systems using the synchronous power controller"*, in 2013 IEEE Energy Conversion Congress and Exposition, 2013, p. 993-998

[37] **H. Bevrani, T. Ise, et Y. Miura**, " *Virtual synchronous generators: A survey and new perspectives* ", International Journal of Electrical Power Energy Systems, vol. 54, p. 244-254, janv. 2014

[38] **P. Tielens et D. Van Hertem**, " *Grid Inertia and Frequency Control in Power Systems with High Penetration of Renewables* ", 2012.

[39] **D. Shrestha, U. Tamrakar, Z. Ni, et R. Tonkoski**, "*Experimental verification of virtual inertia in diesel generator based microgrids*", in 2017 IEEE International Conference on Industrial Technology (ICIT), Toronto, ON, 2017, p. 95-100

[40] **The MathWorks, Inc**, *"Introducing the Phasor Simulation Method "*, https://nl.mathworks.com/help/physmod/sps/powersys/ug/introducing-the-phasor-simulation-method.html, [Online, Accessed 7 June 2020]

[41] **A. Du Bois, B. Martin**, "*Capacité d'hébergement des réseaux publics de distribution basse tension pour des petites installations photovoltaïques*", Master Thesis, Ecole polytechnique de Louvain, Université catholique de Louvain UCLouvain, 2012, Prom. : E. De Jaeger.

[42] **The MathWorks, Inc**, *"Park Transform"*, https://nl.mathworks.com/help/physmod/sps/ref/parktransform.html, [Online, Accessed 7 June 2020]

[43] **U. Tamrakar, R. Tonkoski, Zhen Ni, T. M. Hansen, et I. Tamrakar**, " *Current control techniques for applications in virtual synchronous machines* ", in 2016 IEEE 6th International Conference on Power Systems (ICPS), New Delhi, India, 2016, p. 1-6,

[44] **V. Kharchenko et P. Vasant**, "*Renewable Energy and Power Supply Challenges for Rural Regions*". IGI Global, 2019.

[45] **Elia Group**, "*Our infrastructure*", https://www.elia.be/en/infrastructure-and-projects/our-infrastructure, [Online, Accessed 16 May 2020]

[46] **Elia Group**, "*Data Download*", https://www.elia.be/en/grid-data/data-download-page, [Online, Accessed 17 February 2020]

[47] **S. C. Johnson, D. J. Papageorgiou, D. S. Mallapragada, T. A. Deetjen, J. D. Rhodes, et M. E. Webber**, "*Evaluating rotational inertia as a component of grid reliability with high penetrations of variable renewable energy*", Energy, vol. 180, p. 258-271, août 2019

[48] "*Importance of Inertia in Island Power Systems*", Sigma Power Engineering Pty Ltd, july. 31, 2016. http://www.sigmapower.com.au/24/, [Online, Accessed March 23 2020].

[49] **Belgian Offshore Platform asbl**, "*Projets*",https://www.belgianoffshoreplatform.be/fr/projets/, [Online, Accessed 25 March 2020].

[50] **Elia Group**, "*Physical flows per border*", https://www.elia.be/en/grid-data/transmission/physical-flows-per-border, [Online, Accessed 5 March 2020]

[51] International Energy Agency, " France - Countries Regions ", https://www.iea.org/countries/france, [Online, Accessed XX March 2020]

[52] **J. Sijm et al.**, "*The supply of flexibility for the power system in the Netherlands, 2015-2050 Report of phase 2 of the FLEXNET project*", 2017

[53] **The MathWorks, Inc.**, "*Simplified synchronous machine*", https://nl.mathworks.com/help/physmod/sps/powersys/ref/simplifiedsynchronousmachine.html, [Online, Accessed 15 March 2020]

[54] **A. Marx**, "*An in-depth comparative study of direct drive versus gearbox*", p. 67, Master Thesis, Kungliga Tekniska högskolan Stockholm, 2018.

[55] **S. Benelghali, M. E. H. Benbouzid, et J. F. Charpentier**, "*Comparison of PMSG and DFIG for marine current turbine applications*", in The XIX International Conference on Electrical Machines - ICEM 2010, Rome, Italy, sept. 2010, p. 1-6

[56] **J. Hu et al.**, "*A novel control strategy for Doubly Fed Induction Generator and Permanent Magnet Synchronous Generator during voltage dips*", 2010 20th Australasian Universities Power Engineering Conference, Christchurch, 2010, pp. 1-6.

[57] **V. Yaramasu et B. Wu**, "*Model Predictive Control of Wind Energy Conversion Systems*", Hoboken, NJ, USA: John Wiley Sons, Inc., 2017, p.20.

[58] **X. Yang, D. Patterson, et J. Hudgins**, " *Permanent magnet generator design and control for large wind turbines* ", in 2012 IEEE Power Electronics and Machines in Wind Applications, Denver, CO, USA, juill. 2012, p. 1-5

[59] **A. Soetedjo, A. Lomi, et Widodo Puji Mulayanto**, "*Modeling of wind energy system with MPPT control*", in Proceedings of the 2011 International Conference on Electrical Engineering and Informatics, Bandung, Indonesia, juill. 2011, p. 1-6

[60] **H. M. Hasanien et S. M. Muyeen**, " *Affine projection algorithm based adaptive control scheme for operation of variable-speed wind generato*r ", IET Generation, Transmission Distribution, vol. 9, n 16, p. 2611-2616, déc. 2015

[61] **E. De Jaeger**, "*LELEC2753 - Electrical energy systems; advanced topics*" Course Notes, "*Renewable energy : Wind and PV*", UCLouvain, 2020.

[62] **M. Kayikci et J. V. Milanovic**, "*Dynamic Contribution of DFIG-Based Wind Plants to System Frequency Disturbances*", IEEE Transactions on Power Systems, vol. 24, n 2, p. 859-867, mai 2009

[63] **Elia Group**, "*Losses on the federal electricity network*", `https://www.elia.be/en/grid-data/losses-on-the-federal-electricity-network`, [Online, Accessed 31 May 2020]

[64] **E. De Jaeger**, "*LELEC2520 - Electric Energy Systems*" Course Notes, "*Power Lines*", UCLouvain, 2020.

[65] **E. De Jaeger**,"*LELEC2753 - Electrical energy systems; advanced topics*" Course Notes, "*Power System Dynamics Stability*", UCLouvain, 2020.

[66] **C. F. Ten et P. A. Crossley**, « *Evaluation of Rocof Relay Performances on Networks with Distributed Generation* », 2008, p. 523-528

[67] **European Comission**, "*Comission Regulation establishing a network code on requirements for grid connection of generators*", 2016 `https://eur-lex.europa.eu/legal-content/EN/TXT/?uri=OJ:JOL_2016_112_R_0001#d1e1336-1-1` [Online, Accessed 14 May 2020]

[68] **Hsiao-Dong Chiang, Ebrahim Vaahedi et al.**, *"Load representation for dynamic performance analysis (of power systems)"*, IEEE Trans. Power Syst., vol. 8, n 2, p. 472-482, mai 1993

[69] **P. Kundur**, "*Power System Stability and Control*", New York, USA : McGraw-Hill, Inc., 1994.

[70] **X. Zhang et al.**, « *Deloading Power Coordinated Distribution Method for Frequency Regulation by Wind Farms Considering Wind Speed Difference*s », IEEE Access, vol. 7, p. 122573-122582, 2019

[71] **V. Y. Singarao**, « *Economic Comparison of Deloaded-Wind and Wind-Battery Systems* », in 2014 Sixth Annual IEEE Green Technologies Conference, Corpus Christi, TX, USA, avr. 2014, p. 126-131

[72] **T. Wang, L. Ding, W. Bao, et J. Zheng**, « *A novel deloaded control strategy of DFIG wind farm* », in 2018 13th IEEE Conference on Industrial Electronics and Applications (ICIEA), Wuhan, mai 2018, p. 1681-1685

[73] **Zarina P.P. et S. Mishra**, « *Power oscillation reduction contribution by PV in deloaded mode* », in 2016 IEEE 6th International Conference on Power Systems (ICPS), New Delhi, India, mars 2016, p. 1-4

[74] **P. P. Zarina, S. Mishra**, et P. C. Sekhar, « *Exploring frequency control capability of a PV system in a hybrid PV-rotating machine-without storage system* », International Journal of Electrical Power Energy Systems, vol. 60, p. 258-267, sept. 2014

[75] **L. Toma et al.**, « *On the virtual inertia provision by BESS in low inertia power systems* », in 2018 IEEE International Energy Conference (ENERGYCON), Limassol, juin 2018, p. 1-6

[76] **X. Zhang et al.**, « *Deloading Power Coordinated Distribution Method for Frequency Regulation by Wind Farms Considering Wind Speed Differences* », IEEE Access, vol. 7, p. 122573-122582, 2019

[77] **V. Y. Singarao**, « *Economic Comparison of Deloaded-Wind and Wind-Battery Systems* », in 2014 Sixth Annual IEEE Green Technologies Conference, Corpus Christi, TX, USA, avr. 2014, p. 126-131

[78] **T. Wang, L. Ding, W. Bao, et J. Zheng**, « *A novel deloaded control strategy of DFIG wind farm* », in 2018 13th IEEE Conference on Industrial Electronics and Applications (ICIEA), Wuhan, mai 2018, p. 1681-1685

[79] **Zarina P.P. et S. Mishra**, « P*ower oscillation reduction contribution by PV in deloaded mode* », in 2016 IEEE 6th International Conference on Power Systems (ICPS), New Delhi, India, mars 2016, p. 1-4

[80] **P. P. Zarina, S. Mishra, et P. C. Sekhar,** « *Exploring frequency control capability of a PV system in a hybrid PV-rotating machine-without storage system* », International Journal of Electrical Power Energy Systems, vol. 60, p. 258-267, sept. 2014

[81] **C. Yianni, M. Florides, S. Afxentis, V. Efthymiou, et G. E. Georghiou**, « *Economic viability of battery energy storage system applications* », in 2018 IEEE International Energy Conference (ENERGYCON), Limassol, juin 2018, p. 1-6

[82] **L. Toma et al.**, « *On the virtual inertia provision by BESS in low inertia power systems* », in 2018 IEEE International Energy Conference (ENERGYCON), Limassol, juin 2018, p. 1-6

[83] **Elia Group**, « *System Services* ». `https://www.elia.be/en/electricity-market-and-system/system-services` [Online, Accessed June 12, 2020].

[84] **Elia Group**, « *Capacity Volumes needs* », `https://www.elia.be/en/grid-data/balancing/capacity-volumes-needs` [Online, Accessed 09 June, 2020].

[85] **A. Oudalov, D. Chartouni, C. Ohler, et G. Linhofer**, « *Value Analysis of Battery Energy Storage Applications in Power Systems* », in 2006 IEEE PES Power Systems Conference and Exposition, Atlanta, Georgia, USA, 2006, p. 2206-2211

[86] **Elia Group**, « *Flexible Demand Management Products* ». `EliaBy_Special_AncillaryServices_20170523_ENG_LR-EN.pdf`, [Online, Accessed 09 June, 2020].

[87] **Elia Group**, « *Load and load forecasts* », `https://www.elia.be/en/grid-data/load-and-load-forecasts`, [Online, Accessed 08 June, 2020].

[88] **Elia Group**, « *Wind-power generation* », `https://www.elia.be/en/grid-data/power-generation/wind-power-generation`, [Online, Accessed 08 June, 2020].

[89] **Elia Group**, « *Solar-PV power generation data* ». `https://www.elia.be/en/grid-data/power-generation/solar-pv-power-generation-data`, [Online, Accessed 08 June, 2020].

[90] **O. Schmidt, S. Melchior, A. Hawkes, et I. Staffell**, « *Projecting the Future Levelized Cost of Electricity Storage Technologies* », Joule, vol. 3, n 1, p. 81-100, janv. 2019

[91] **B. Marchi, M. Pasetti, et S. Zanoni**, « *Life Cycle Cost Analysis for BESS Optimal Sizing* », Energy Procedia, vol. 113, p. 127-134, mai 2017

[92] **M. Wilson**, « *Lazard's Levelized Cost of Storage Analysis—Version 4.0* », p. 60, 2018, Lazard

[93] **P. Larsson, P.Börjesson**, « *Cost models for battery energy storage systems* », KTH School of Industrial Engineering and Management, Energy Technology EGI-2018.

[94] **Elia Group**, « *Prix de desequilibre 15 min* », `https://www.elia.be/fr/donnees-de-reseau/equilibrage/prix-de-desequilibre-15-min` [Online, Accessed June 10, 2020].

[95] **Elia Group**, « *Prix de reference day-ahead* ». `https://www.elia.be/fr/donnees-de-reseau/transport/prix-de-reference-day-ahead`, [Online, Accessed 06 June, 2020].

[96] **G. Carpinelli, S. Khormali, F. Mottola, et D. Proto**, « *Battery Energy Storage Sizing When Time of Use Pricing Is Applied* », Scientific World Journal, vol. 2014, 2014

[97] **Trading Economics**, « *European Union Inflation Rate | 1997-2020 Data | 2021-2022 Forecast | Historical* », `https://tradingeconomics.com/european-union/inflation-rate` [Online, Accessed 06 June, 2020].

[98] **Elia Group**, « *Capacity Auction results* ». `https://www.elia.be/en/grid-data/balancing/capacity-auction-results`, [Online, Accessed 09 June, 2020].

[99] **B. Zhang, W. Hu, et Z. Chen**, « *Stochastic optimal regulation service strategy for a wind farm participating in the electricity market* », in 2015 IEEE Innovative Smart Grid Technologies - Asia (ISGT ASIA), Bangkok, Thailand, nov. 2015, p. 1-5

UNIVERSITÉ CATHOLIQUE DE LOUVAIN
École polytechnique de Louvain
Rue Archimède, 1 bte L6.11.01, 1348 Louvain-la-Neuve, Belgique | **www.uclouvain.be/epl**